LOAN DOCUMENT

PHOTOGRAPH THIS SHEET

DTIC ACCESSION NUMBER

LEVEL

INVENTORY 0

RIA-83-U252

DOCUMENT IDENTIFICATION

JAN 83

DISTRIBUTION STATEMENT A
Approved for Public Release
Distribution Unlimited

DISTRIBUTION STATEMENT

ACCESSION FOR
NTIS GRA&I
DTIC TRAC
UNANNOUNCED
JUSTIFICATION

BY

DISTRIBUTION/

AVAILABILITY CODES

DISTRIBUTION	AVAILABILITY AND/OR SPECIAL	
A-1		

DISTRIBUTION STAMP

DATE ACCESSIONED

DATE RETURNED

1999051704 1

DATE RECEIVED IN DTIC

REGISTERED OR CERTIFIED NUMBER

PHOTOGRAPH THIS SHEET AND RETURN TO DTIC-FDAC

DTIC FORM 70A JUN 90

DOCUMENT PROCESSING SHEET

PREVIOUS EDITIONS MAY BE USED UNTIL STOCK IS EXHAUSTED.

LOAN DOCUMENT

HANDLE WITH CARE

ARMY MATERIEL SYSTEMS ANALYSIS ACTIVITY

PART II

PROCEEDINGS
FOURTH MEETING OF THE COORDINATING GROUP
ON
MODERN CONTROL THEORY
27-28 OCTOBER 1982
OAKLAND UNIVERSITY
ROCHESTER, MICHIGAN 48063

U S ARMY MATERIEL SYSTEMS ANALYSIS ACTIVITY
ABERDEEN PROVING GROUND, MARYLAND 21005

UNCLASSIFIED

SECURITY CLASSIFICATION OF THIS PAGE *(When Data Entered)*

REPORT DOCUMENTATION PAGE		READ INSTRUCTIONS BEFORE COMPLETING FORM
1. REPORT NUMBER	2. GOVT ACCESSION NO.	3. RECIPIENT'S CATALOG NUMBER
4. TITLE *(and Subtitle)* PART II - Proceedings of the Fourth Meeting of the Coordinating Group on Modern Control Theory (27-28 Oct 1982) Oakland University, Rochester, Michigan 48063		5. TYPE OF REPORT & PERIOD COVERED Conference 6. PERFORMING ORG. REPORT NUMBER
7. AUTHOR(s) H. Cohen (Chairman)		8. CONTRACT OR GRANT NUMBER(s)
9. PERFORMING ORGANIZATION NAME AND ADDRESS Director US Army Materiel Systems Analysis Activity Aberdeen Proving Ground, MD 21005		10. PROGRAM ELEMENT, PROJECT, TASK AREA & WORK UNIT NUMBERS DA Project No. 1R665706M541
11. CONTROLLING OFFICE NAME AND ADDRESS Director US Army Materiel Systems Analysis Activity ATTN: DRXSY-MP, Aberdeen Proving Ground,MD 21005		12. REPORT DATE January 1983 13. NUMBER OF PAGES
14. MONITORING AGENCY NAME & ADDRESS*(If different from Controlling Office)* Cdr, US Army Materiel Development & Readiness Command, 5001 Eisenhower Avenue, Alexandria, VA 22333		15. SECURITY CLASS. *(of this report)* UNCLASSIFIED 15a. DECLASSIFICATION/DOWNGRADING SCHEDULE
16. DISTRIBUTION STATEMENT *(of this Report)* Approved for public release; distribution unlimited		
17. DISTRIBUTION STATEMENT *(of the abstract entered in Block 20, if different from Report)*		
18. SUPPLEMENTARY NOTES		
19. KEY WORDS *(Continue on reverse side if necessary and identify by block number)* Control theory, Kalman Filtering, Man-Model, Maneuvering Target, Fire Control, Missile Guidance and Control, Robotics, Artificial Intelligence		
20. ABSTRACT *(Continue on reverse side if necessary and identify by block number)* Report documents papers presented at fourth meeting of the coordinating group on modern control theory with emphasis on military weapon systems.		

DD FORM 1 JAN 73 1473 EDITION OF 1 NOV 65 IS OBSOLETE

UNCLASSIFIED

SECURITY CLASSIFICATION OF THIS PAGE *(When Data Entered)*

TABLE OF CONTENTS

Next page intentionally left blank.

FOURTH MEETING

OF

COORDINATING GROUP ON MODERN CONTROL THEORY

27-28 OCTOBER 1982

OAKLAND UNIVERSITY
MEADOW BROOK HALL
Rochester, Michigan 48063

AGENDA

WEDNESDAY, 27 OCTOBER 1982

ROOM #1 - MORNING

SESSION I: Weapon Stabilization and Control (Chairman - Dr. Ronald Beck)

WELCOMING STATEMENT -

0900 - Wideband Modern Control of Microprocessor-Based Tracking and Pointing Systems
by William J. Bigley, Vincent J. Rizzo
Lockheed Electronics Company, Inc.
Plainfield, New Jersey 07061

0930 - Discrete-Time Disturbance Accommodating Control of a Helicopter Gun-Turret System
by N. P. Coleman, R. Johnson, E. Carroll
US Army Armament Research & Development Command
Dover, New Jersey 07801

1000 - Firing Data Comparison of Classical and Modern Turret Controllers
by G. A. Strahl
Ware Simulation Section
US Army Armament Research & Development Command
Rock Island, IL 61299

1030 - Development of a Combat Vehicle Support Plan Using Modern System Theory
by A. Fermelia
Martin-Marietta Aerospace
Denver Division (Mail Stop 0570)
P. O. Box 179
Denver, CO 80201

1100 - Closed Loop Methodology Applied to the Combat Vehicle Support Plan
by A. Fermelia
Martin-Marietta Aerospace
Denver Division (Mail Stop 0570)
P. O. Box 179
Denver, CO 80201

1130 - Controllability of Disturbed Reticle Tank Fire Control Systems
by Paul G. Cushman
Ordnance Systems
General Electric Company
Pittsfield, Mass. 01201

ROOM #2 - MORNING

SESSION II: Missile/Air Defense Fire Control (Chairman - Mr. Herbert E. Cohen)

0900 - Endgame Performance Study of a Special Class of Interceptors
by Dr. Jonathan Korn
ALPHATECH, Inc.
3 New England Executive Park
Burlington, Mass. 01803

0930 - Applications of Heuristic and Game-Theoretic Paradigms to Fire Control
by Max Mintz
Dept of Systems Engineering
University of Pennsylvania
Philadelphia, PA 19104

Terry L. Neighbor
Advanced Development Branch
Air Force Flight Dynamics Laboratory
Wright-Patterson AFB, OH 45433

Walter Dziwak
US Army Armament Research & Development Command
Fire Control & Small Caliber Weapon Systems Laboratory
Dover, NJ 07801

Stephen S. Wolff
US Army Armament Research & Development Command
Ballistic Research Laboratory
Aberdeen Proving Ground, MD 21005

1000 - Application of Modern Control Theory and Adaptive Control Concepts to the Guidance and Control of a Terminally Guided Anti-Tank Weapon
by R. D. Ehrich
Missile Systems Division
Rockwell International
Columbus, OH 43216

1030 - Free-Flight Rocket Guidance with the Spinning Plug Nozzle
by W. E. Judnick and A. H. Samuel
Battelle-Columbus Laboratories
505 King Avenue
Columbus, OH 43201

1100 - Boost-Phase Steering for Surface-Launched Cruise Missiles
by D. J. Fromnes
General Dynamics Convair Division
P. O. Box 80847
San Diego, CA 92138

1130 - Closed-Loop Bullet Tracking Algorithms for Digital Fire Control Systems
by Radhakisan S. Baheti
Corporate Research & Development
General Electric Company
Schenectady, NY 12345

ROOM #1 - AFTERNOON

SESSION III: Robotics (Chairman - Professor Nan K. Loh)

1300 - DARPA Intelligent Task Automation (ITA)
by Dr. Edward C. van Reuth
Dr. Elliott C. Levinthal
Defense Advanced Research Projects Agency
1400 Wilson Boulevard
Arlington, VA 22209

1330 - Vision Systems for Intelligent Task Automation
by Dr. C. Paul Christensen
Dr. Roger A. Geesey
Dr. C. Martin Stickley
The BDM Corporation
7915 Jones Branch Drive
McLean, VA 22102

1400 - A Robotic Tank Gun Autoloader
by S. J. Derby
Benet Weapons Laboratory, LCWSL
US Army Armament Research & Development Command
Watervliet Arsenal
Watervliet, NY 12189

1430 - Experiments in Nonlinear Adaptive Control of Mechanical Linkage Systems
by T. M. Depkovich
Martin-Marietta Aerospace
Denver Division (Mail Stop 0570)
P. O. Box 179
Denver, CO 80201

H. Elliott
Department of Electrical & Computer Engineering
University of Massachusetts
Amherst, MA 01003

1500 - Force Feedback Sensors for Robot Adaptive Control
by Robert DeMoyer, Eugene Mitchell
US Naval Academy
Mail Drop 14A
Annapolis, MD 21402

John Vranish
Naval Surface Weapons Center
NSWC Robotics R&D Laboratory
Dhalgren, VA

1530 - Challenges in Robotic and Artificial Intelligence for NBC Remote Detection and Reconnaissance
by Kirkman Phelps, William R. Loerop, Bernard W. Fromm
Chemical Systems Laboratory
US Army Armament Research & Development Command
Aberdeen Proving Ground, MD 21005

1600 - Robot Decontaminating Systems
by M. B. Kaufman
Chemical Systems Laboratory
US Army Armament Research & Development Command
Aberdeen Proving Ground, MD 21005

1630 - Multi-Resolution Clutter Rejection
by Dr. Allen Gorin
Image Processing Lab
Lockheed Electronics Company
Plainfield, NJ

ROOM #2 - AFTERNOON

SESSION IV: Control Theory & Applications (Chairman - Mr. Toney Perkins)

1300 - An Optimal Integral Submarine Depth Controller
by M. J. Dundics
Director of Program Development
Tracor Incorporated
19 Thames St
Groton, CT 06340

THURSDAY, 28 OCTOBER 1982

ROOM #1 - MORNING

SESSION V: Gun Fire Control (Chairman - Dr. Norman Coleman)

0900 - VATT - The Gunner's "Invisible" Aid
by J. A. Wes
Northrop Corporation
Electro-Mechanical Division
Anaheim, CA 92801

0930 - A Modern Control Approach to Gun Firing Accuracy Improvements
by Robert J. Talir, Donald L. Ringkamp, Fred W. Stein
Emerson Electric Company
8100 W. Florissant Avenue
St. Louis, Missouri 63136

1000 - A Modern Control Theory View of HIMAG Test Data
by R. A. Scheder, A. T. Green, B. C. Culver
Delco Electronics Division
General Motors Corporation
Coleta, CA 93117

1030 - Maneuvering Vehicle Path Simulator
by T. R. Perkins, H. H. Burke, J. L. Leathrum
US Army Materiel Systems Analysis Activity
Aberdeen Proving Ground, MD 21005

1100 - Improving Air-to-Ground Gunnery Using an Attack Autopilot and a Moveable Gun
by Dr. Edward J. Bauman
Department of Electrical Engineering
University of Colorado
Colorado Springs, CO 80907

Captain Randall L. Shepard
Department of Astronautics
USAF Academy, CO 80840

ROOM #2 - MORNING

SESSION VI: Missile Stabilization & Control (Chairman - Dr. Donald R. Falkenburg)

0900 - A Fire Coordination Center for Lightweight Air Defense Weapons
by William C. Cleveland
LADS Program Office
Ford Aerospace & Communications Corporation
Newport Beach, CA 92660

Next page intentionally left blank.

ACKNOWLEDGEMENT

I would like to take this opportunity to thank Sharon Betts of the Protocol Office, US Army Tank-Automotive Command for her invaluable assistance in arranging this meeting and to Professor Nan Loh, Oakland University and Dr. Ronald Beck, US Army Tank-Automotive Command, for their dedicated work in developing an outstanding technical program. Lastly, to Otto Renius, US Army Tank-Automotive Command for the support and encouragement he has provided and to Dean Mohammed S. Ghausi, Dean of the School of Engineering, Oakland University for making these beautiful facilities available.

HERBERT E. COHEN
Chairman
Coordinating Group on
Modern Control Theory

Next page is blank.

FORCE FEEDBACK SENSORS FOR ROBOT ADAPTIVE CONTROL

John M. Vranish, Naval Surface Weapons Center
Prof. Eugene Mitchell, U.S. Naval Academy
Prof. Robert DeMoyer, U.S. Naval Academy

Next page intentionally
left blank.

FORCE FEEDBACK SENSORS FOR ROBOT ADAPTIVE CONTROL

John M. Vranish, Naval Surface Weapons Center
Prof. Eugene Mitchell, U.S. Naval Academy
Prof. Robert DeMoyer, U.S. Naval Academy

ABSTRACT

The objective of this paper is to describe the Naval Surface Weapons Center (NSWC) Program for developing high performance, simple, rugged, cost effective magnetoelastic force feedback sensors for robots and machine tools. Recent advances in magnetoelastic material technology have paved the way for corresponding improvements in the state of the art in force feedback sensors for robots and machine tools. Also, NSWC has designed magnetic circuits which are easily adapted to force feedback sensors. In this paper, magnetoelastic materials are described along with the properties that make them potentially such outstanding force feedback sensors. Following this, the NSWC Program is detailed including advances in materials research, in simple, low cost electronic and magnetic circuits, and designs for force feedback sensor modules. The results are in the public domain.

INTRODUCTION

NSWC is developing high performance, simple, rugged, cost effective magnetoelastic/magnetostrictive force feedback sensors for machine tools and robots. (Note figure 1.)

The Navy is facing increasingly severe manpower and skills shortages. Costs of equipment and complexities of equipment maintenance are escalating. To combat this, CAD/CAM, intelligent automation, and robotics are depended upon to play a vital role. Tactile/force feedback sensors will be at the center of the Navy effort.

To optimize its contribution, NSWC is pulling together a range of disciplines, technical expertise, and experience ranging from materials basic research, to signal processing techniques, to modular robotic sensor designs.

The heart of this coordinated effort is the materials basic research. Since the 1960's, NSWC has been performing basic research in rare earth materials. In recent months, breakthroughs have been achieved which permit these materials to be used to push the state of the art for a range of practical, high performance, tactile/force feedback sensor applications.

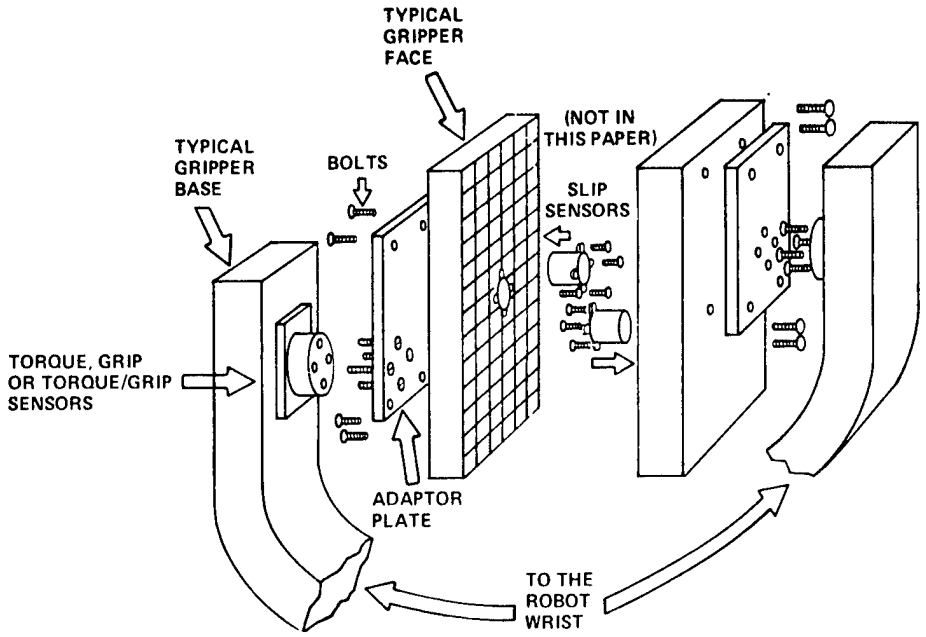

FIGURE 1 RETROFIT TECHNIQUE

NSWC has also made major technical accomplishments in magnetometer circuitry for sensitive magnetic field sensors. This expertise is being applied toward the closely related problem of force feedback sensor circuitry and signal processing.

In this paper, magnetoelastic/magnetostrictive materials are described along with the properties that potentially make them such outstanding force feedback sensors. Following this, the magnetic circuit signal processing techniques will be described. Finally, all these disciplines will be integrated to form tactile/force feedback sensor modules for grip and torque. Designs, circuits, and research results are in the public domain.

MATERIALS

In this section, the magnetoelastic effect is explained including its subsets, the "Villari" effect, and the magnetostrictive effect. Next, the make up and characteristics of the NSWC materials are described and the reasons they are potentially such outstanding tactile/force feedback sensors. Finally, research test results are given.

A material is magnetoelastic if there is a relationship between (1) changes in the internal magnetic moment (and hence $\vec{B}$ field), (2) changes in the physical forces applied to or by it, and (3) changes in its physical length. A magnetoelastic material exhibits the "Villari" effect when it shows a change in its $\vec{B}$ field as a result of its being subjected to external forces of tension or compression. A magnetoelastic material exhibits the magnetostrictive effect when it shows a change in either (1) its

physical length due to changes which have been induced in its internal $\vec{B}$ field, or (2) the inverse-changes in its internal $\vec{B}$ field which have been induced by changes in its physical length.

In this paper we are basically concerned with two families of magnetoelastic materials; amorphous ribbons - $Fe_{70}Co_{10}B_{20}$ (with small amounts of silicon and cobalt) and $Tb_{.27}Dy_{.73}Fe_2$ rods. Both materials exhibit "Villari" and magnetostrictive effects.* The amorphous ribbons are superior in "Villari" effect sensing applications due to stretching forces and the $Tb_{.27}Dy_{.73}Fe_2$ rods are superior in magnetostriction (but they can also perform excellent "Villari" effect sensing in response to compressive forces).

This materials development was begun when NSWC scientists reasoned that while rare earth materials possess extraordinary magnetic properties at below room temperatures, it might be possible to develop alloys and amorphous solutions combining the rare earths with the more classical ferrous materials to provide practical new materials with extraordinary performance properties. These materials can be used at normal room temperature and above. After nearly 20 years of research into this matter, the materials are now reaching the point where they are ready for industrial applications.

Let us now discuss how these materials act as tactile/force feedback sensors. As shown in figure 2, the materials are first treated so that each internal magnetic domain lines up with its net magnetic moment perpendicular to the long axis of the material. At the same time, the net magnetic moment of each domain is pointed in a direction opposite to that of its neighbor's. This leaves the material with a total net magnetic moment of zero; thus reducing spurious effects and increasing material sensitivity. If the magnetoelastic material is now biased by an external magnetic field $\vec{H}$ (either by permanent magnetic material or current) the magnetic moments rotate toward the direction of the field. For maximum linear dynamic range, the bias $\vec{H}$ field is set such that the direction of the net magnetic moment of each magnetic domain is at approximately 45° to the axis of the material.

---

*Magnetoelastic materials research has been in process at NSWC since the 1960's. The material "terfenol" ($Tb_{.27}Dy_{.73}Fe_2$) was discovered by Dr. A. E. Clark at NSWC. Dr. H. Savage and staff have pursued the work in perfecting the material (along with several applications patents). Research in another material (amorphous ribbons) was begun at NSWC by Dr. M. Mitchell and has since been continued by Dr. Kabacoff and staff.

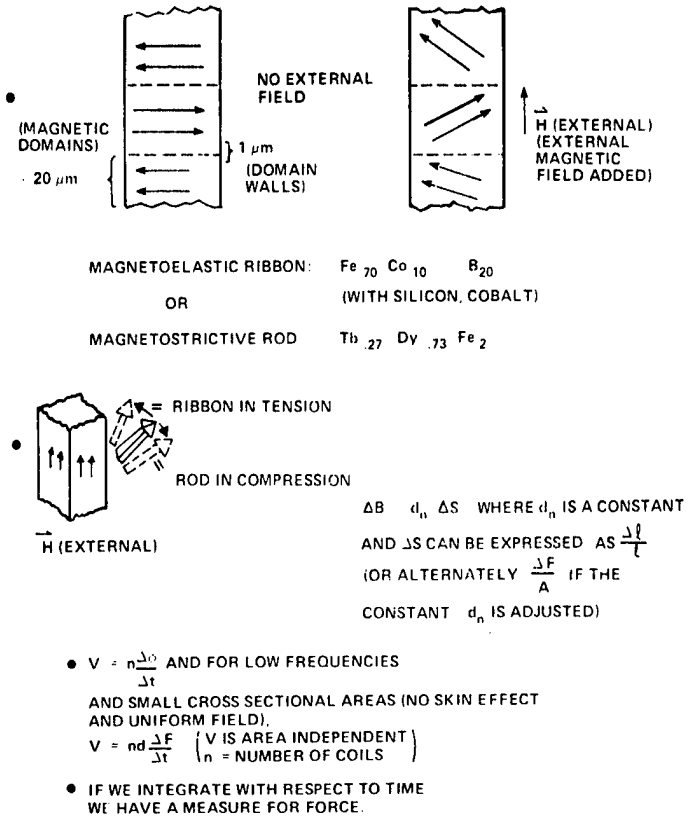

FIGURE 2 HOW THE MATERIALS ACT AS FORCE SENSORS

Magnetoelasticity

As the ribbon is stretched by an external force, the net magnetic moment of each domain rotates toward the ribbon axis at an angle which is linearly proportional to the exciting force. The additive effect of all these magnetic moments rotating toward the ribbon axis is that the ribbon total $\vec{B}$ field rotates toward its longitudinal axis, linearly proportional to the exciting force. By the same token, as a terfenol rod is compressed by an external force, its total $\vec{B}$ field rotates away from its longitudinal axis, linearly proportional to the exciting force. In both cases, this is a "Villari" effect. This linear relationship can be described by the following equations:

$$|\Delta B| = |d\frac{\Delta F}{A}|$$

where $|\Delta B|$ is the total net change in the Material $\vec{B}$ field, d is a constant and $|\frac{\Delta F}{A}|$ is the applied force per unit area.

$$\left|\frac{\Delta F}{A}\right| = y\left|\frac{\Delta \ell}{\ell}\right|$$

where y is the Young's Modulus of the material in psi and $\left|\frac{\Delta \ell}{\ell}\right|$ is the material change in length per unit length.

$\left|\frac{\Delta \ell}{\ell}\right| = d|\Delta H|$ where $|\Delta H|$ is an externally applied magnetic field. (One should recall that $\vec{B} = \mu \vec{H}$ where μ is the material permeability ($\mu_o \mu_r$).

Referring to figure 2, if we wrap either an amorphous ribbon or a terfenol rod with coils of insulated wire and send current through the wire, a $\vec{B}$ field will be superimposed on the $\vec{B}$ field already in the material. This will cause the amorphous ribbon and terfenol rods to expand or contract depending on the product of the current and the number of coils. This magnetostrictive property is most pronounced for terfenol rods (see figure 3).

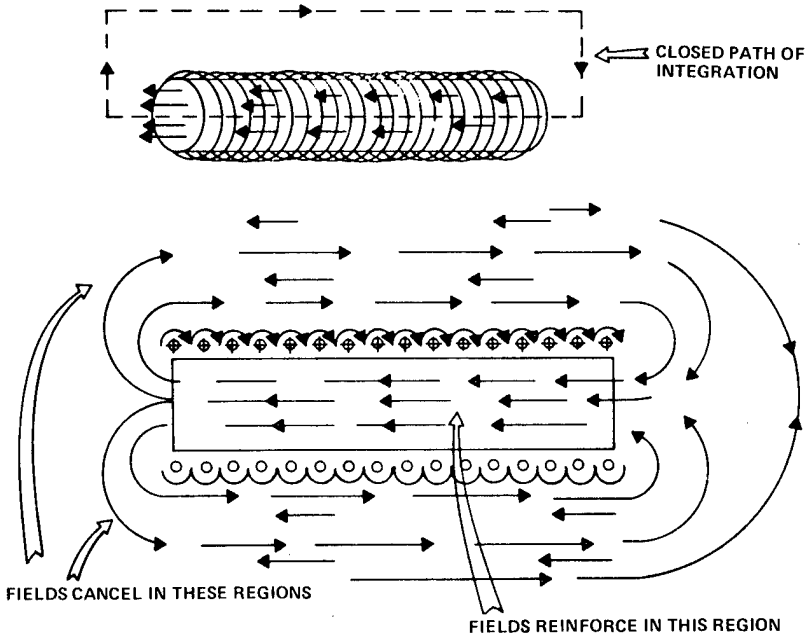

NOT TO SCALE

FIGURE 3 H&B FIELDS IN THE MAGNETOSTRICTIVE ROD

Again, we can use the $|\Delta\vec{B}| = d|\Delta F/A|$ relationship. But $\Delta\vec{B} = \mu\Delta\vec{H}$ where $\mu = \mu_o \mu_r = 4 \times 10^{-7}(8)$ since μ terfenol = 8.**

The question then becomes how large can we make ΔB? Let us illustrate by picking a few numbers. Using a current of 1 amp, a rod length of 2 inches (5.08 cm), .25 in. diameter (.635 cm) and with 2000 turns of wire around it, we will get:

$$\oint_\ell \vec{H} \cdot d\vec{\ell} = I = 2000 \quad (1)$$

(where length is in meters). And referring back to figure 3, this simplifies to $\Delta B\,(.0508) = 2000$ (1 amp)

Thus $\vec{B} = .126$ webers/m^2

$|\vec{B}| = d|\Delta\vec{F}/A|$; $d = .25 \times 10^{-7}$ webers/newton for terfenol and 1 lb = 4.44 newtons.

So $\vec{F}$ = 35.9 lbs or 159 newtons

Again back to our equation

$$|\Delta\vec{H}| = d\left|\frac{\vec{\Delta\ell}}{\ell}\right| \text{ where } d = \frac{8.6}{\mu_o \mu_r} \times 10^2 \text{ webers/m}^2$$

$$\Delta\vec{B} = 8.6 \times 10^2 \frac{\Delta\vec{\ell}}{2 \text{ in}}$$

But $\Delta\vec{B} = .126$ webers/m^2

Thus $\vec{\Delta\ell} = 2.93 \times 10^{-4}$ in (7.44×10^{-4} cm)
Magnetostriction

Of course one can see that increasing the product of the current and windings increases both the force and the magnetostrictive travel. (Magnetostriction of .001 in. per inch is easily achievable for terfenol.)

Force Sensing

There are essentially two methods for force sensing using magnetoelastic materials, one a technique which measures the total force acting on the sensor and one which measures the rate of change of the force acting on the sensor.

**Values and equations from Dr. Howard Savage's notes 4/13/81.

First we will discuss the technique which measures the total force on the sensor. In this technique an external oscillator source is used. It should be noted that the amorphous ribbon with its μ_r of the order of magnitude of 20,000 (vs 8 for the terfenol rods) is the better of the two for the total force sensing technique. So, for this method we shall use the amorphous ribbon in our example. Let us start by coiling an insulated wire around an amorphous ribbon and connecting this wire to an AC source. This will provide the drive circuit. (See figure 4.) We can wrap another set of insulated wire coils over the coils of the driving circuit and these provide the signal. The driving circuit is constructed so that it drives the amorphous ribbon back and forth into saturation. Since the waveform drops back rapidly to zero, the output signal, which is proportional to $\frac{d\phi}{dt}$, is maximum. But we know that the characteristics of the amorphous ribbon are such that its μ_r changes with applied force. This means that the saturation $\vec{B}$ field changes and we have a difference between the $\vec{B}$ field with and without applied force ($\Delta\vec{B}$). This $\Delta\vec{B}$ is some function of the applied force or pressure which we can call f_1 (P). This $\Delta\vec{B}$ translates into a difference in the voltage output V which in turn relates back to the applied force or pressure by some function F_2(P). We call this the external oscillator technique. (See figure 5.)

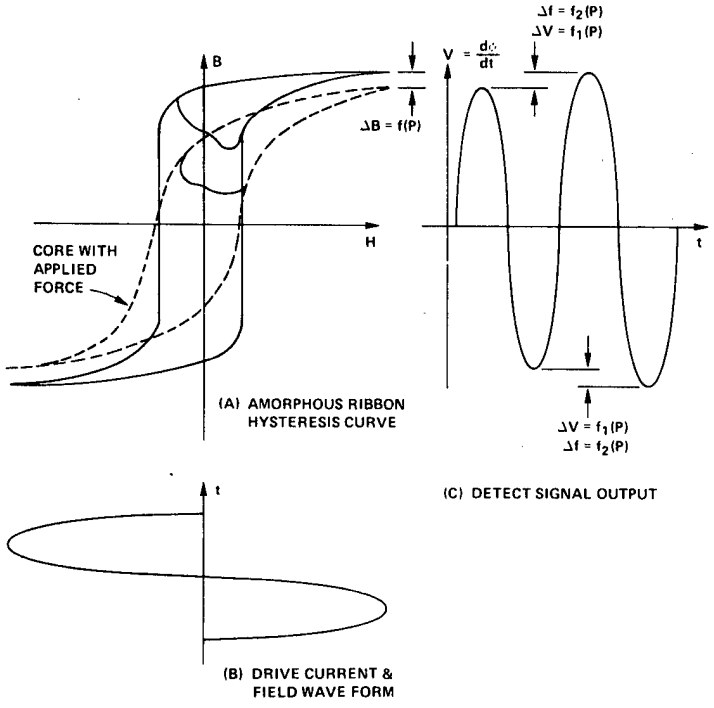

FIGURE 4 SIGNAL PROCESSING SIN MAGNETOELASTIC RIBBONS

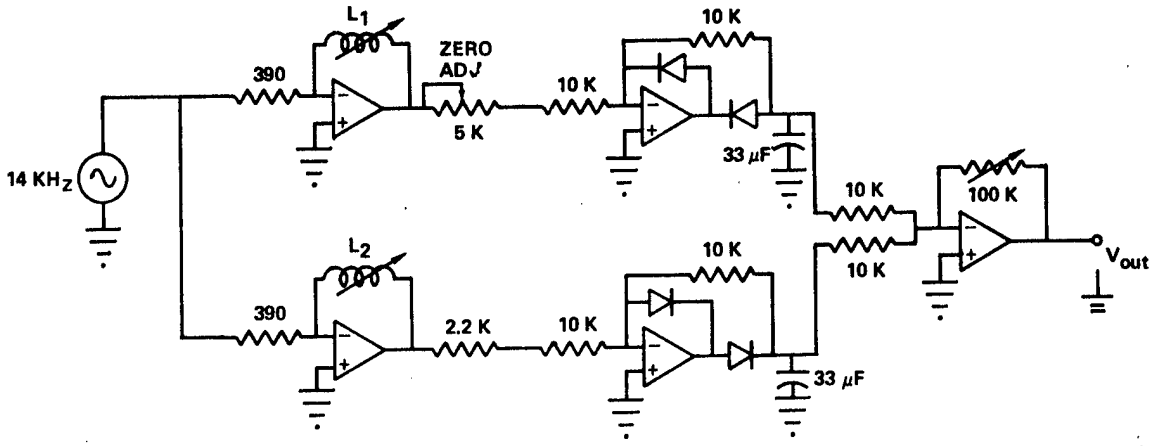

FIGURE 5 THE SEPARATELY EXCITED OSCILLATOR

Next we will discuss the technique which measures the derivative of the total force (or pressure) with respect to time ($\frac{dF}{dt}$). This technique depends on the rate of change of flux ϕ ($\phi = \oint_S \vec{B} \cdot d\vec{s}$ ($\vec{s}$ = area of ribbon or rod cross section). The governing equation is:

$$V = n \frac{d\phi}{dt}$$

n = number of coils
V = voltage output

Looking at figure 2, we can see that we have essentially a passive sensor with one set of coils (no driving circuit). It will operate at very low frequencies (to DC), those of the robotic tactile force itself. At these low frequencies, and with the small cross sectional areas of the ribbons and rods (typically .006 in^2), there is virtually no skin effect or magnetic hysteresis and the equation simplifies to:

$$V = n \frac{d}{dt} \oint_S \Delta\vec{B} \cdot d\vec{s} \quad (\Delta\vec{B} = d\frac{\Delta\vec{F}}{A})$$

So:

$$V = n \frac{d}{dt} d_2 \frac{\Delta F}{\cancel{A}} \cancel{A} \quad (S = A)$$

$$V = nd_2 \frac{dF}{dt}$$

Thus we can see that the voltage is proportional to the term $|\frac{dF}{dt}|$ (or $|\frac{d\Delta F}{dt}|$) and the integral of $\int_{t_1}^{t_2} V\,dt$ yields the total force.

The high efficiency of the rods and ribbons (mechanical work on the material compared to the change in magnetic field ΔB) makes the derivative sensor practical.

Generally the force derivative sensor provides a relatively low voltage, high power output. And, comparing figures 2 and 3, one can see that when a terfenol rod is used there is the option of it acting either as a sensor or actuator. On the other hand, the external oscillator technique yields higher output voltages and the sampling time is not critical (since total force is measured). Clearly, the preferable technique depends on the application.

Let us now discuss why these materials are potentially such good force feedback and tactile sensors.

Outstanding Sensitivity

Both the ribbons and the terfenol rods have demonstrated outstanding sensitivity. A 0.8 ratio for magnetomechanical coupling has already been produced at NSWC for both the rods and amorphous ribbon and the value is expected to climb to 0.9. This 0.8 value is the ratio of the output voltage to the voltage equivalent of the force applied to the material. A 40 mV/V ratio was previously considered excellent.

Outstanding Dynamic Range

A conservative estimate of the ribbon's linear region for dynamic range is $\pm$1,000 psi. It should also be noted that experiments at NSWC (for underwater pressure sensors) have indicated that it is possible to resolve .004 psi in a background depth of 266 psi. This means that theoretically we can expect 10 log (266/.004) = 48.2 dB volts. 30 dB power or 15 dB volts is normally considered to be excellent. The terfenol rods have a dynamic range 2 times that of the ribbons and are prestressed to 2,000 psi.

No Observable Mechanical Hysteresis

The amorphous ribbons and terfenol rods are, for all intents and purposes, completely recoverable. This recoverability extends to well beyond 2 or 3 times the $\pm$1,000 psi linear dynamic range of each.

Outstanding Linearity

Graphs for both experiments conducted by Japanese investigators, K. Mohri and E. Sudoh, showed outstanding linear response and this linearity has been duplicated at NSWC by investigator J. F. Scarzello.***

Simple Electronics

The circuitry for the oscillator drive method is shown in figure 5. As can be seen from the figure, only one small circuit board is needed.

***P.4 NSWC memo dtd 23 Nov 1979, "Development of a pressure transducer using amorphous magnetic materials," by J. F. Scarzello.

Tough, Inexpensive, Corrosion Resistant and Radiation Hardened Materials

The amorphous ribbons are tough and can stand up to 20,000 psi (13,764 newtons/cm^2). The rods, when prestressed to 2,000 psi (1,376 newtons/cm^2) in a metal can, are also tough. Both materials can be mass produced inexpensively. Both are extremely resistant to corrosion and radiation. But there are aspects of the material which require additional investigation and/or are a bit troublesome.

Stray Fields and Voltage Offsets

This is a problem, particularly for the amorphous ribbons because they have such a high μ (magnetic permeability) and because they are driven by the "external oscillator" technique. NSWC is pursuing three techniques to deal with this problem: (1) putting magnetic shielding material around the ribbons, (2) using 2 sets of symmetrical windings so that the errors are self cancelling, and (3) using filtering and digital signal processing techniques.

Noise in the Ribbon (when operated as part of the external drive oscillator system)

This noise tends to restrict the available dynamic range of the system. As a result, the materials experts at NSWC are continuing to work on improving the material and considerable progress has been made. It has also been noted that the ribbons tend to resonate magnetostrictively, so selecting the proper drive frequency can lower noise considerably. 15 KHz has yielded good results.

Brittleness in the Terfenol Rods

Very recent experiments at NSWC have resulted in terfenol rods which can stand 2,000 psi (1,376 newtons/cm^2) in tension (in addition to high compressive capabilities). This represents still another improvement in the breed.

Low u_r in the Terfenol Rods

Low u_r and high magnetostrictive capabilities go hand in hand so only limited progress can be made in this area. This means that the terfenol rods must act as derivative sensors and cannot be driven by the separately excited oscillator technique.

Temperature Stability

This has not been fully tested though stability to 100°C is anticipated.

SIGNAL PROCESSING

In this section, signal processing techniques will be outlined including both the oscillator drive technique and the derivative method. Some of the expected signal processing problems and their usual methods of solution are addressed.

The oscillator drive method is the main signal processing technique to be used in the grip, torque, and grip/torque modules.

As mentioned above, this method measures the total force or torque as the case may be and it is simple, sensitive, and accurate. In addition, this technique is well understood at NSWC since it was developed for magnetometers in underwater mine and space applications, and it has resulted in many major publications and patents dating back to 1970. (For example, a magnetometer designed jointly by NSWC and NASA Ames Research Center was a part of the equipment deployed on the lunar surface in the Apollo 16 Mission.)

The Relationship of Magnetometers to Robotic Force Feedback Sensors

In a magnetometer, the magnetically active element (in our case an amorphous ribbon) has its $\vec{B}$ field changed by an intruding magnetic field. This $\vec{B}$ in turn changes the magnetic reluctance of the amorphous material. If the material is being excited by an oscillator drive, as an intruding magnetic field adds to or subtracts from the magnetic field in the magnetometer core, output voltage will be affected. But as we noticed earlier, the same effect will occur if the ribbon is physically stressed. Thus the oscillator drive signal processing technique is equally applicable to force feedback sensors and magnetometers.

A Brief Description of how the Oscillator Drive Processing Technique Works

A key factor is the current/field wave shape in the driving circuit coils. This wave shape is such that the current/field builds to a peak and then rapidly drops to zero. The resulting large $\frac{d\phi}{dt}$ can be used to provide a voltage output which is a function of the force on the ribbon (see figures 4 and 5).

As the sensor ribbon is stretched by a robotic force or torque, the slope of the $\vec{B}$-$\vec{H}$ curve becomes steeper and the output voltage greater. Also, inductance is proportional to the slope of this curve, so a circuit which will produce a signal proportional to inductance will produce a measurable signal.

The central component of the circuit is an operational amplifier (op-amp). As a result of high amplifier gain, A, and high input impedance, it can be shown that the output voltage is related to the input voltage by the ratio of feedback and input impedance.

$$V_b = -(\frac{Z_b}{Z_a})\ V_a$$

Suppose the input voltage is sinusoidally varying:

$$V_a = V \sin(\omega t)$$

Its magnitude is given by

$$|V_a| = V$$

If the input component is a resistor, and the feedback component an inductor: then

$$Z_a = R \quad Z_b = j\omega L$$

and

$$|V_b| = (\frac{\omega V}{R})\ L$$

Thus a signal is produced which is proportional to inductance.

If both ribbons are pre-tensioned, an additional force will increase inductance in one coil, and decrease inductance in the other, both by L (figure 5).

The voltage magnitudes at points V_1 and V_2 are given by

$$V_1 = \frac{V\omega\ (L - \Delta L)}{R} \qquad V_2 = \frac{V\omega\ (L + \Delta L)}{R}$$

The orientation of the diodes cause the dc levels

$$V_3 = |V_1| \quad V_4 = -|V_2|$$

The final op-amp adds V_3 and V_4.

$$V_o = -(\frac{Rb}{Ra}) \qquad (V_3 + V_4)$$

Combining the above

$$V_o = (\frac{2V\omega\ Rb}{R\ R_a})\Delta L$$

This is a signal proportional to the difference in inductance caused by an imbalance in ribbon tension (sensor ribbon compared to a ref. ribbon). This simplified circuit is expanded to include a zero adjustment and ideal diodes.† Specific component values are shown in figure 5.

The V_o from the circuit shown in figure 5 can now be further processed. We can pick up the RMS voltage output (using perhaps a simple square law detector). In this process, the equation $V_o = 4.44\ N_2 f\ BA \times 10^{-8}$ volts

N = number of windings
f = frequency
A = area

is a good estimate of the RMS value we would expect. Since a force on a robotic sensor introduces a change in B using, once again, the equation $|\Delta\vec{B}| = d|\frac{\Delta\vec{F}}{A}|$, we will get a change in the total voltage output of approximately:

$$V_{rms} = 4.44\ N_2 f\ \ B\ A \times 10^{-8} \text{ volts}$$

since

$$|\Delta\vec{B}| = d|\frac{\Delta\vec{F}}{A}|$$

$$|\Delta\vec{F}| = \frac{\Delta V_{rms} \times 10^{-8}}{4.44\ N_2 f d}$$

Thus simply measuring the RMS voltage output will provide us with the information we need to solve the force, or torque, directly.

The derivative technique can also be used for signal processing in any of the magnetoelastic/magnetostrictive robotic force feedback sensors. As mentioned above, in the derivative technique the equation $V = n\frac{d\phi}{dt}$ applies or $V = n\frac{d}{dt}\left\{d\Delta F\right\}$ $V = n\ d|\frac{dF}{dt}|$. So, again, we are dealing with the rate of force application.

---

†From "Progress Report Magnetoelastic Sensor Development," 6/15/81 thru 8/15/81 Prof. R. DeMoyer and Prof. E. Mitchell, U.S. Naval Academy, 9/15/81, pp. 11-13

ROBOTIC TORQUE, GRIP, GRIP/TORQUE MODULES

In this section, preliminary designs for robotic torque and grip modules will be described. In addition, since the sensors are designed to be modular, a grip/torque sensor will be described which is the result of cascading a grip and a torque sensor module together. The modules are for a large industrial robot that can lift 250 lbs (114 Kg).

The Torque Module (figures 4, 5 and 6)

The design goals for the torque module are 125 in-lb (144.1 Kgcm) of torque in the linear region in a package of nominally 2.5 in. diameter (6.35 cm) and 3/4 in. (1.9 cm) height. Again, as shown in figure 1, this module is designed to go into the wrist of the robot gripper. The 125 in-lb torque parameter is picked because it is assumed that a worst case condition is one in which the robot picks up a 225 lb object with a .5 in. deviation from the object's center of gravity. With 0.030 in. (.08 cm) typical robot movement accuracy, this represents an extreme case.

Design Calculations

Figure 6 shows the design philosophy. When the flat bar spring bends, the ribbon is either stretched or compressed (depending on direction of torque). This is a linear relationship with the force on the end of the bar. From our design requirements we know that we need a maximum torque of 125 in-lbs. This must be balanced by the bending moment in the aluminum bars of the torque sensor.

$$|\vec{T}| \text{ (125 in-lbs)} = (4)(2)\int_{o}^{x_o} x\,dF$$

4 = number of bars
2 = tension and compression
xdF = Δtorque

For a rectangular beam $\frac{Fx}{Ax_o}\int w\,dx = dF$

$|\frac{F}{A}|$ = psi at outer fiber of bar

x_o = distance from bar center to outer fiber

w = bar width

But

$$|\frac{\vec{F}}{A}| = Y_m\,|\frac{\Delta\vec{\ell}}{\ell}|; \quad Y_m = 10.3 \times 10^6 \text{ psi for aluminum}$$

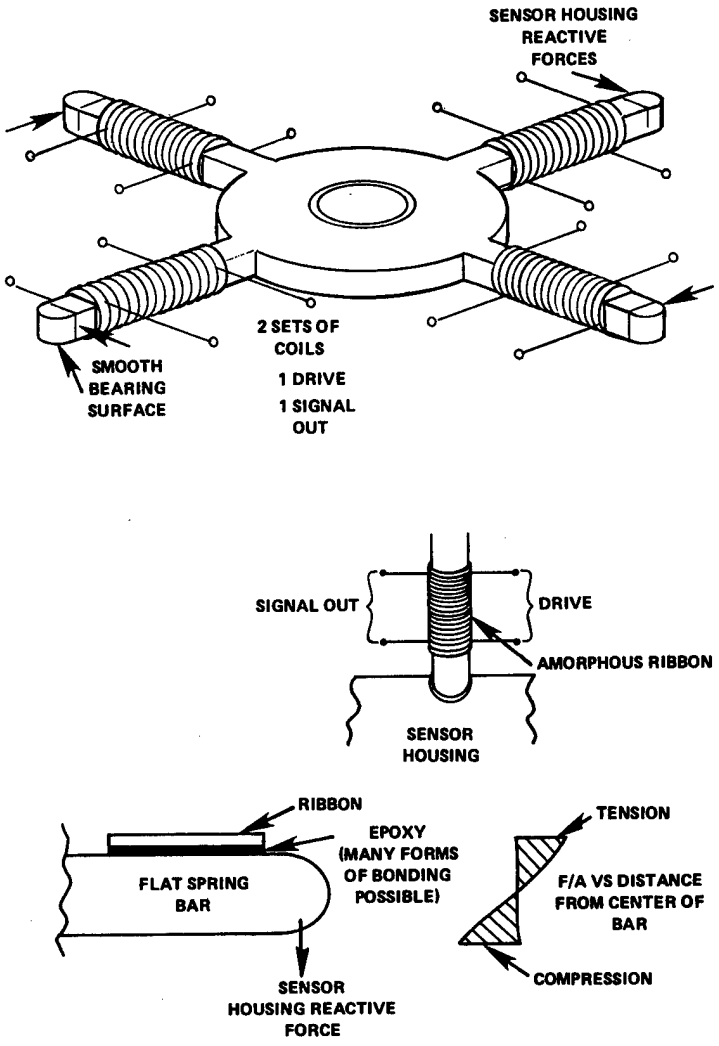

FIGURE 6 TORQUE SENSOR

and for amorphous ribbons = 25 x 10^{-6}in/in

Lets add on 25 x 10^{-6}in/in for adhesive shear.

$$125 = 8 \int_{o}^{x_o} x\frac{Fx}{Ax_o} \qquad dx = 8(10.3)(50)\int_{o}^{x_o}\frac{x^2}{x_o} \qquad dx$$

$$wx_o^2 = \frac{125}{4120}$$

If we make it 3/4 in. wide, it must be .4 in. thick. This means that if our electronics has 30 dB dynamic range, we can pick up .125 in-lb to 125 in-lb in the linear to 250 in-lb using the non-linear region. Of course, we will expect much better sensitivity.

We know $V_{rms} = 4.44\ N_2 f\ BA \times 10^{-8}$ volts (CGS units)

$B = d\ F/A$

for Mks units use

$$d = 11.1 \frac{F_{lb}}{Acm^2}\ ††$$

with f = 15 KHz; V_{rms} required = .1mV

we get the design relationship

$$.0135 = F\ lb\ N_2 \text{ or } .00614 = F_{kg} N_2$$

We will use a ribbon .2 in. wide by .002 in. thick with 0 to ±1,000 psi linear dynamic range. So, at its maximum stress, it will experience (1,000) .002(.2) = .4 lb tension or compression. This corresponds to .125 in-lbs torque on the beams. To get down to .025 in-lbs (28.9 gmcm or 37 dBV dynamic range), we need .00008 lb sensitivity in the ribbon:

$$.00008\ N_2 = .0135$$

$$N_2 = 168; \text{ use } N_2 = \underline{170 \text{ turns}}$$

It will be a challenge to get the electronics to handle such sensitivity.

At this point we will examine the results from a test prototype torque sensor. This prototype was built oversize so as to facilitate testing and modification. It is essentially patterned on the concept shown in figure 6.

Results (see figure 7)

At 10 KHz, inductance increases with tension up to a point after which it remains constant. This is true for both annealed and unannealed ribbon.

Slight deviations from linearity at the curve extremes are probably due to the adhesive yield in shear.

Using annealed ribbon, the change in inductance effect with tension is reversed from the unannealed version.

---

††Meeting 3/23/80, Dr. Howard Savage, J. M. Vranish.

The annealed ribbon can take high signal levels without saturation, and the output is a reasonably linear function of applied load in both tension and compression.

Conclusions

The annealed ribbon excited at a frequency near its resonance exhibits desirable properties: near linearity, large dynamic range, and high level output. The phase shift between the annealed and unannealed is due to the fact that annealed and unannealed ribbons resonate magnetostrictively at different frequencies.

Future Work

A magnetic return path should be installed to determine if the effects of external iron proximity can be totally eliminated.

Many trade-offs include:

Signal levels
Frequency
Number of turns on coils

All components must be miniaturized in order to construct a practical torque/force sensor.†††

We can now show the design approach that will be taken on the grip sensor. This is the same as the torque sensor except the force comes straight down and the ribbons are on the top and bottom of the bars rather than the sides as in the torque sensor.

The design goals for the grip sensor are 250 lbs (182 kg) maximum grip in a small package 2.5 in. (6.35 cm) diameter and 1 in. (2.54 cm) deep.

Grip Sensor Design Calculations

The grip sensor will be designed similar to the torque sensor. 250 lbs (113.5 kg) maximum design grip will be distributed among the 4 aluminum bars of the grip sensor.

So: $62.5\ell = 8 \int_{o}^{x_o} \frac{(Fx)}{Ax_o} wdx$ as before. ℓ = bar length

and this reduces to $62.5\ell = 4118\ wx_o^2$

---

†††"Progress Report Magnetoelastic Sensor Development," 6/16/81 through 8/15/81, pp. 28-31.

using ℓ = 1 in. and picking w = 3/8 in., we get a bar thickness of .4 in. (1.02 cm). Our electronics relationships remain the same as for the torque sensor.

$$.0135 = F_{lb} \quad N_2$$

If we use .008 lb in our ribbon as the minimum force to pick up at .1mV rms signal output voltage, we will need 170 coils as before.

Future Directions

During the first year, NSWC will continue to develop and refine the sensor modules. This will include optimizing the amorphous sensor material for robotic applications.

In the second year, the sensor modules will be interfaced with the NSWC robot to iron out the control theory and vision coordination questions. Also during this year, a gripper will be designed for the removal of high tension fasteners from Navy missiles.

In the third year, a gripper will be built and the sensor modules interfaced.

In the fourth year, the gripper will be interfaced to a heavy duty industrial robot and the combined system tested in a Naval Weapons Station.

SUMMARY AND CONCLUSIONS

In summary, we have described the NSWC Program for developing high performance, simple, rugged, cost effective magnetoelastic/magnetostrictive force feedback sensors for machine tools and robots in CAD/CAM operations. We have shown that the NSWC Program is a comprehensive program including basic materials research, signal processing, and robot sensor modules. We have outlined the materials characteristics, the signal processing techniques, and the robotic sensor designs. The basic research has been successfully completed, and practical force feedback sensors for robots are being constructed and debugged. The NSWC Program will significantly advance the state of the art in force feedback sensors.

BIBLIOGRAPHY

1. For materials introduction, U.S. Navy Journal of Underwater Acoustics, Vol. 27, No. 1, Jan. 1977 "Introduction to Highly Magnetostrictive Rare-Earth Materials," by Dr. A. E. Clark.

2. For Terfenol Rod Application read "The Robotic Sensor/Gripper," J. Vranish, NSWC, Feb. 1981.

3. For Brown Oscillator Circuits - See U. S. Patent 3,649,908, March 1982, and the publication entitled "A Miniature Fluxgate Magnetometer with Subgamma Noise," presented at IEEE Intermag Conference, Kyoto, Japan, April 1972.

4. Handbook of Physics, 1957, McGraw Hill.

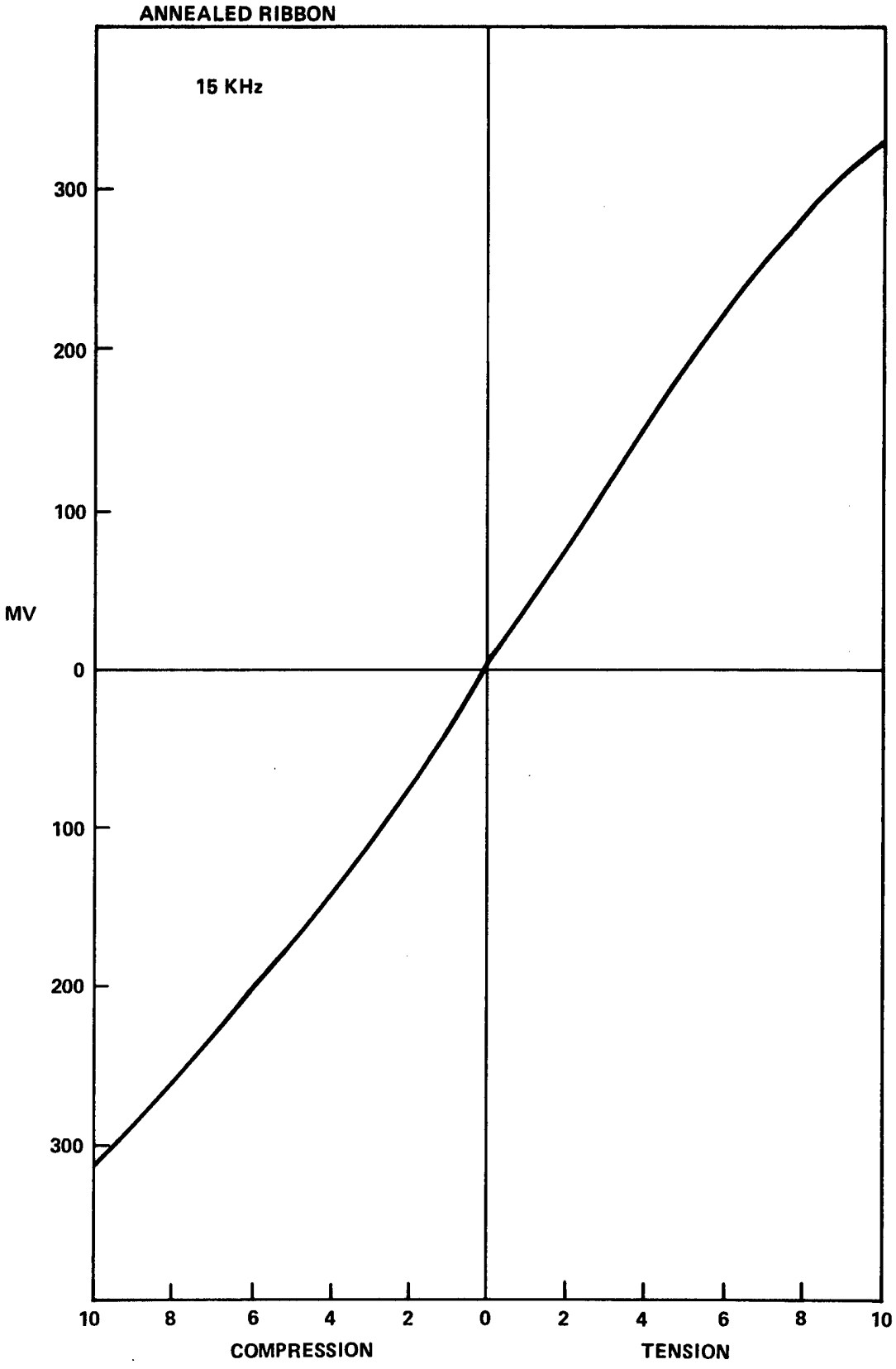

FIGURE 7 LINEARITY RESULTS

MODERN CONTROL TECHNIQUES APPLICABLE TO THE SPACE SHUTTLE MAIN ENGINE

T. C. Evatt
Rockwell International Corporation
Rocketdyne Division

Next page intentionally left blank.

MODERN CONTROL TECHNIQUES APPLICABLE TO THE SPACE SHUTTLE MAIN ENGINE

T. C. EVATT

ROCKWELL INTERNATIONAL CORPORATION
ROCKETDYNE DIVISION
SYSTEMS ANALYSIS
CANOGA PARK, CALIFORNIA 91304

INTRODUCTION

Historically, development of liquid propulsion rocket control systems has utilized classical control techniques to regulate thrust and mixture ratio. The approach taken here is to model the Space Shuttle Main Engine as a linear-multivariable system whose parameters vary with engine operating environment. Only inputs and noise corrupted outputs realizable at an actual engine are considered. The engine control objective centered on controlling preburner temperature, mixture ratio and thrust (combustion pressure). An eighth order linear model with two actuators (valves) and their associated dynamics is derived to apply optimal linear quadratic design methodologies to control fuel turbine inlet temperature gradients. The design methodology selected to investigate and develop a feedback controller for these temperature gradients is the Linear Quadratic Gaussian (LQG) design philosophy.[1] This method is a systematic method of regulator control using a Kalman-Bucy filter (state estimator) to determine plant states from measured parameters. A subset of the LQG design methodology, the Linear Quadratic Regulator (LQR) will be derived for an SSME deterministic model at one design point and graphical results presented.

The use of this modern control methodology represents an advance in the design philosophies used in rocket engine control systems. At the time of the SSME control system design in the early 1970's, attention was given to both classical and modern control system design methodologies. The state of the art, however, was not mature enough to use the modern control systems design approach for the SSME. As a result, an advanced application of the classical methodology was selected for the control system design.

With the foreseeable increasing performance demands on the SSME, LQG control methodology that relies on linear quadratic synthesis of regulators at different operating points is being applied to design an improved control system. Many papers have been written on engine control using Linear Quadratic Design

techniques. Hoff and Hall[2,3] have discussed a control design methodology for turbine engine control synthesis using regulators at a number of power levels at sea level, static conditions. Taiwo[4] discussed a method of turbine controller design using Zakain's method of inequalities. Merrill[5] has used sampled data regulators to design multivariable control laws for jet propulsion. Michael and Farrar[6] discussed a practical and systematic linear quadratic synthesis procedure. The regulator design techniques, however, rely on full-state availability.

This paper is divided into four sections. The first section introduces the SSME rocket engine and the techniques used to simulate the dynamics of the SSME including linear model derivation. A discussion of actuator dynamics and their effect on closed-loop response is also presented. In the next section, the LQG technique is briefly discussed with a more detailed description of the Linear Quadratic Regulator. A procedure is discussed for choosing the LQR weighting matrices. Conclusions and recommendations follow.

SSME TURBOPUMP ROCKET ENGINE

INTRODUCTION

With the advent of the space shuttle concept in the late 60's, it became apparent that a reusable and reliable engine design was needed. The high performance requirements of the Space Shuttle Orbiter demanded a new state of the art in liquid propellant rocket engine design. The Space Shuttle Main Engine (SSME) design uses a staged combustion power cycle (Figure 1) coupled with high combustion chamber pressures. In the SSME staged combustion power cycle, the propellants are partially burned at low mixture ratio, very high pressure, and relatively low temperatures in the preburners to produce hydrogen-rich gas to power the turbopumps. The hydrogen-rich gas steam is then routed to the main injector where it is injected, along with additional oxidizer and fuel, into the main combustion chamber at a higher mixture ratio and pressure. Liquid hydrogen is used to cool all combustion devices directly exposed to contact with high-temperature combustion products. An electronic engine controller automatically performs checkout, start, mainstage and engine shutdown functions.

The SSME was developed especially for the Space Shuttle Orbiter Vehicle, which uses three engines for launch. The SSME is a reusable, high performance, liquid propellant rocket engine with variable thrust. The engine is ignited on the ground at launch and operated in parallel with the solid rocket boosters during the initial ascent phase and continues to operate for approximately 520 seconds total firing duration. The requirement for 55 missions totaling 7.5 hours of cumulative operating

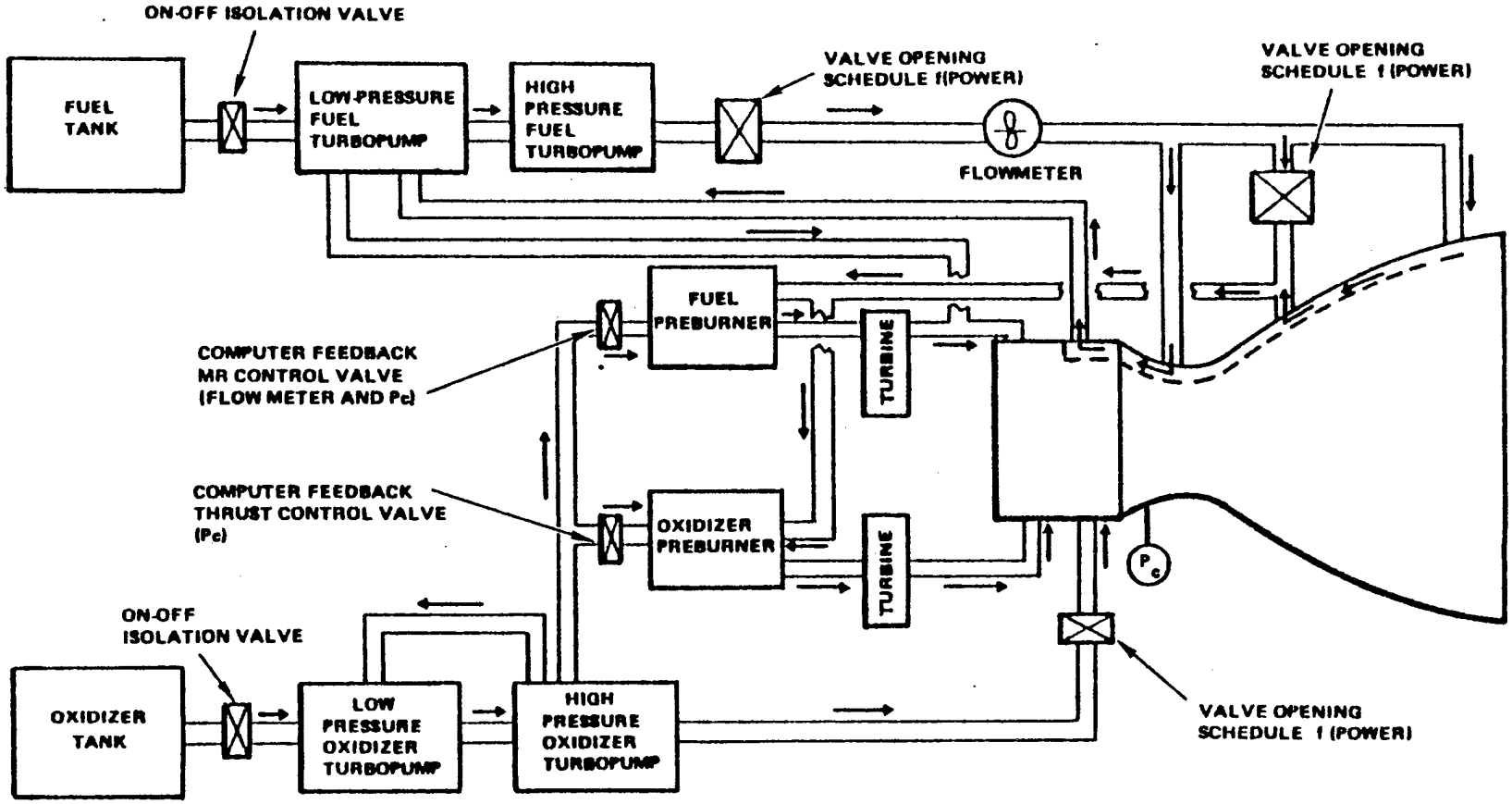

- 3 SCHEDULED AND 2 CONTROLLED VALVES FOR MR AND THRUST LEVEL

FIGURE 1 -- SIMPLIFIED ENGINE CONTROL SYSTEM, STAGED COMBUSTION ENGINE

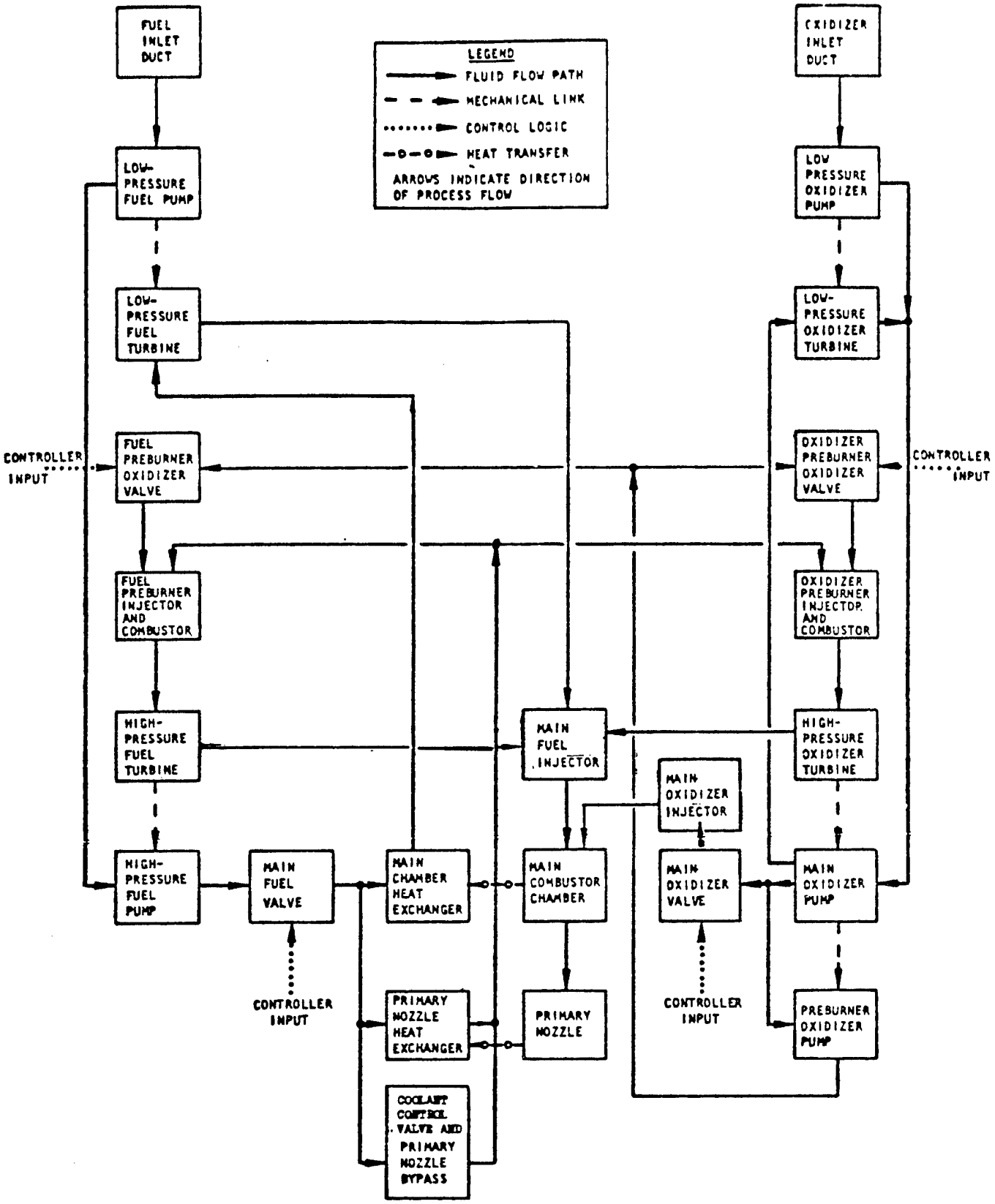

FIGURE 2 -- ANALOG MODEL FLOW DIAGRAM

time with varying thrust levels represented the first significant requirement for a reusable liquid rocket engine. The SSME is a very efficient engine with a specific impulse of approximately 455 seconds at rated power level (RPL) (470,000 pounds of thrust altitude). The two stage combustion is approximately 99.96% efficient. The main chamber combustion pressure is approximately 3000 psia at rated power level. The turbopumps are direct drive, i.e., they have no gear trains. Another interesting feature of the SSME is that it uses head pressure to supply the energy to start the engine. There are no start tanks, turbine spinners, or pyrotechnics involved in engine start. Electrical igniters are supplied in the fuel and oxidizer preburner and the main combustion chamber to initiate combustion.

Each of the rocket engines operates at a mixture ratio of 6:1, and over a throttling range of 109%-65% RPL. This provides a higher thrust level during lift off and the initial ascent phase, and allows orbiter acceleration to be limited to 3g during the final ascent phase. The engines are gimballed to provide pitch, yaw, and roll control during orbiter boost phase.

SSME HYBRID SIMULATION MODEL

The first stage in designing a feedback control law is to derive a set of differential equations that describe the system response as accurately as possible. The SSME hybrid model developed by Rocketdyne on the AD-10/PDP-11 computer is the simulation model used in this study. The engine system analog simulation model is constructed on a component basis. Individual turbines, pumps, heat exchangers, and fluid flow passages are characterized by equations defining component variations, dynamic relationships, and interface requirements. The system simulation includes all static and dynamic formulations that are considered of importance in accurately representing overall start, mainstage control, and cutoff behavior of the engine.

The hybrid model contains three subsections that are used to develop the basic building blocks to represent all phenomena of significance. The engine fuel flow system involves all physical processes where hydrogen in a gas, liquid, two-phase, or super-critical state is handled. The oxidizer flow portion of the engine system involves the physical processes where oxygen is handled by the engine system prior to being involved in any combustion process. The hot-gas portion of the engine system simulation includes all component processes that involve handling oxygen/hydrogen combustion products. This model contains simplifications which include perfect gas law assumptions instead of National Bureau of Standards Property Tables, curve fitting of some functions, and linearization of second-order nonlinear effects. A schematic of the simulation program is shown in Figure 2.

The analog model description represents SSME dynamics and is applicable for simulating engine start, throttling, and cutoff dynamics at nominal conditions. The analog model differential equations are used to develop the control linear model used in subsequent sections of the paper.

CONTROLLER REQUIREMENTS

The SSME control system is designed to meet or exceed all performance control requirements set by the Contract End Item (CEI) specification. Typical CEI requirements encompass the performance criteria for startup, mainstage, and shutdown (Table 1). As can be observed in Table 1, all CEI control requirements are met or exceeded by the present controller.

For this study, CEI design requirements will be the ultimate goal with the added goal of minimization of temperature gradients (F/s) in the preburners. Excessive temperature gradients (spikes) during engine start/cutoff can cause localized cracking of turbine blades (e.g., shortening of turbine blade life).

In summary, the SSME controller requirements for this study are:

1. Design a multivariable control loop which will be capable of performing control functions on a simulated (hybrid) SSME and demonstrating superior performance against existing SSME controls.

2. Develop the above multivariable control loop with the added design goal of minimizing turbine blade metal thermal gradients (thermal shock; F/s) on the SSME.

MODELING TECHNIQUES

Introduction

The solution for a nonlinear set of differential equations is difficult or impossible to solve analytically. An approach that will allow an approximate solution to the process equations taken from the SSME hybrid model is called small disturbance theory, small perturbation theory, or linearization.[8,12] Initially, a set of steady state operating conditions is found from an engine balance. These determine the values of the state and control variables needed to maintain the engine at the steady state operating conditions. The process equations are then linearized about the engine design point. The following sections describe the linearization procedure for a general set of nonlinear equations and then apply the result to the SSME analog equations discussed previously.

TABLE 1 -- SUMMARY OF SSME PERFORMANCE CONTROL REQUIREMENTS

	CEI REQUIREMENTS	ROCKETDYNE PERFORMANCE
STARTUP		
TIME TO NPL	LESS THAN 5 SECONDS	3.5 SECONDS
RATE OF INCREASE		
0 TO 15% THRUST	20,000 LB THRUST/10 MS MAX	20,000 LB THRUST/10 MS
ABOVE 15% THRUST	7,000 LB THRUST/10 MS MAX	7,000 LB THRUST/10 MS
IMPULSE TO NPL	464,000 LB-SEC MIN	464,000 LB-SEC BOOSTER, 540,000 LB-SEC ORBITER
IMPULSE VARIATION TO NPL	75,000 LB-SEC MAX	75,000 LB-SEC ORBITER
PROPELLANT USED TO NPL	2,320 LB MAX (1,800 PROPOSED)	1,500 LB
MAINSTAGE		
THRUST CONTROL		
RANGE OF CONTINUOUS CONTROL BETWEEN MPL AND EPL		BETWEEN MPL AND EPL
TOLERANCE	±10,000 LB THRUST (±7,500 PROPOSED)	±5,920 LB THRUST (STEADY STATE)
120 K STEP RESPONSE	1 SECOND MAX	1 SECOND
RATE OF THRUST CHANGE		
WHILE MEETING TOLERANCE	7,000 LB THRUST/SEC MIN	7,500 LB THRUST/SEC
DURING STEP	7,000 LB THRUST/10 MS MAX	7,000 LB/10 MS
LOW-FREQUENCY THRUST OSC AMPLITUDE	±10 K LB 0-0.5 Hz, ±2 K LB 0.5 Hz-1.5 Hz ±0.6 K LB 1.5-25 Hz ±2 K LB 25-100 Hz	±10 K LB 0-0.5 Hz, ±2 K LB 0.5 Hz-1.5 Hz ±0.6 K LB 1.5-25 Hz ±2 K LB 25-100 Hz
MIXTURE RATIO		
RANGE OF CONTROL		
BETWEEN MPL AND NPL	5.5 TO 6.5	5.5 TO 6.5
AT EPL	6.0	6.0
TOLERANCE	±2% OF COMMANDED (±12 PROPOSED)	±0.82% OF COMMANDED
RESPONSE TIME	3 SECONDS/ONE UNIT MAX	3 SECONDS/ONE UNIT
SHUTDOWN		
TIME FROM NPL	2.72 SECONDS MAX	2.0 SECONDS
RATE OF DECREASE	7,000 LB THRUST/10 MS MAX	7,000 LB/10 MS
IMPULSE FROM NPL	525,000 LB-SEC MAX	525,000 LB-SEC (ORBITER)
IMPULSE VARIATION	52,500 LB-SEC MAX	52,500 LB-SEC
IMPULSE FROM MPL	100,000 LB-SEC MIN	100,000 LB-SEC (ORBITER)
PROPELLANT BELOW MPL	480 LB MAX	450 LB
PROPELLANT BELOW NPL	1,340 LB MAX	1,340 LB

Linearization Procedure

Since there are eight first-order differential equations that are necessary to describe the fuel preburner process dynamics, the linearized system will be eighth order with two control variables. The six state and two control variables are shown in Figure 3 with definitions given in Table 2.

The general linearization procedure can be carried out in basically two steps for any set of nonlinear equations. They are:

1. The set of equations must be written in the form

   $$f(\dot{x}, x, u) = 0$$

   by moving all the terms to the left of the equality.

2. Expand f in a multivariable Taylor series expansion about some reference trajectory-given by $f(0, x, u) = 0$. This expansion is valid only for small changes in the state and control variables, x and u, respectively. All second order terms are considered small and are dropped

   $$\Delta\dot{x} = A\,\Delta x + B\,\Delta u$$

where

$$A = \frac{-\partial f^{-1}}{\partial \dot{x}} \frac{\partial f}{\partial x} \text{ (system matrix)}$$

$$B = \frac{-\partial f^{-1}}{\partial \dot{x}} \frac{\partial f}{\partial u} \text{ (control matrix)}$$

$$\frac{\partial f}{\partial \dot{x}} = \begin{bmatrix} \frac{\partial f_1}{\partial \dot{x}_1} & \frac{\partial f_1}{\partial \dot{x}_2} & \cdots & \frac{\partial f_1}{\partial \dot{x}_n} \\ \vdots & & & \vdots \\ \frac{\partial f_n}{\partial \dot{x}_1} & & & \frac{\partial f_n}{\partial \dot{x}_n} \end{bmatrix}_{\text{ref}}$$

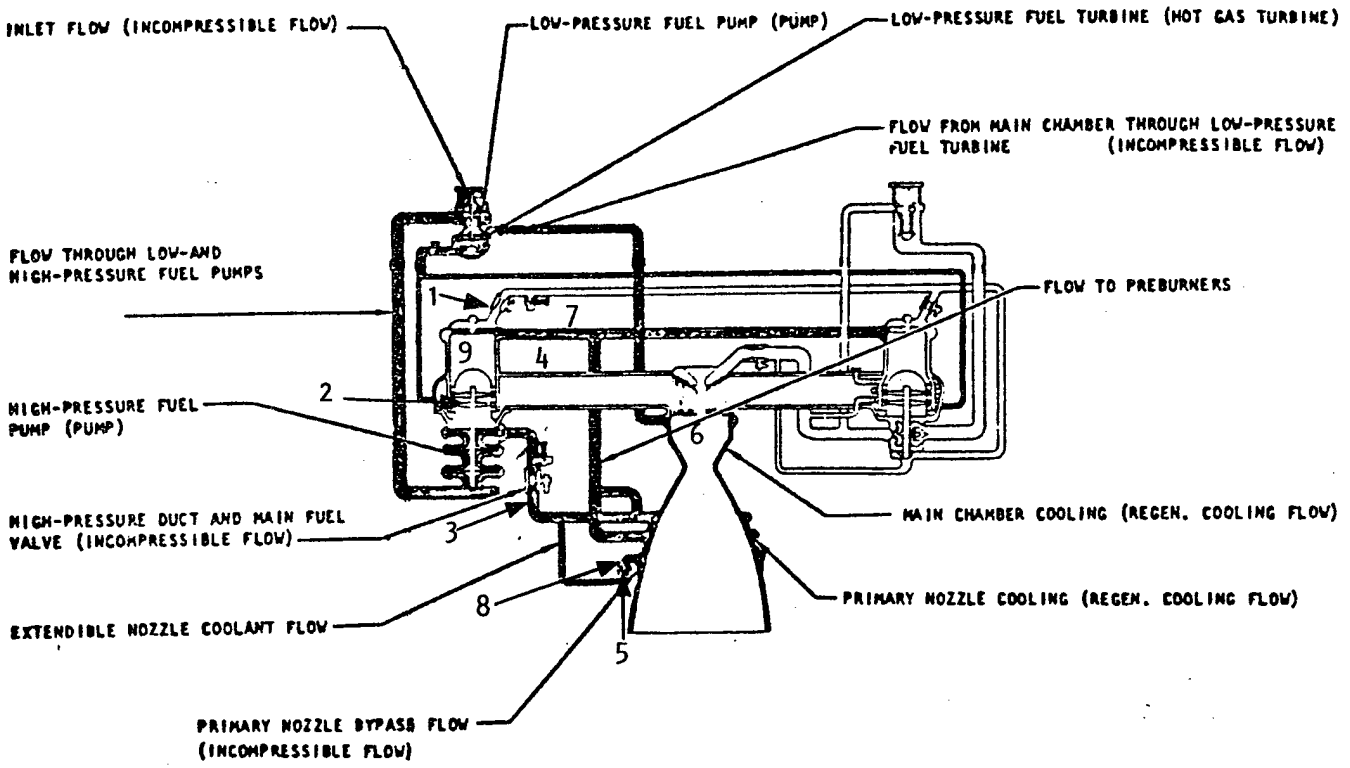

SPACE SHUTTLE MAIN ENGINE SCHEMATIC SHOWING ENGINE STATE, CONTROL, AND AUXILIARY VARIABLES

FIGURE 3

TABLE 2

SUMMARY OF SSME PERFORMANCE CONTROL REQUIREMENTS
STATE, CONTROL AND AUXILIARY
VARIABLE DEFINITIONS

NO.	STATE		DEFINITION
1	DWFPO	-	Fuel Preburner Oxidizer Flow Rate (lbm/s)
2	SF2	-	High Pressure Fuel Turbopump Speed (RPM)
3	PMFVD	-	Main Fuel Valve Downstream Pressure (PSI)
4	DWFPF	-	Fuel Preburner Fuel Flow Rate (lbm/s)
5	DWFNBP	-	Primary Fuel Nozzle Bypass Flow Rate (lbm/s)
6	PC	-	Main Combustion Pressure (PSI)
	CONTROL		
7	FPOV	-	Fuel Preburner Oxidizer Valve Setting (%)
8	CCV	-	Coolant Control Valve Setting (%)
	AUXILIARY		
9	TFP	-	Fuel Preburner Temperature (^{o}R)

and

$$\frac{\partial f}{\partial x} = \begin{bmatrix} \frac{\partial f_1}{\partial x_1} & \frac{\partial f_1}{\partial x_n} \\ \vdots & \vdots \\ \frac{\partial f_n}{\partial x_1} & \frac{\partial f_n}{\partial x_n} \end{bmatrix}_{ref} \qquad \frac{\partial f}{\partial u} = \begin{bmatrix} \frac{\partial f_1}{\partial u_1} & \cdots & \frac{\partial f_1}{\partial u_m} \\ \vdots & & \vdots \\ \frac{\partial f_n}{\partial u_1} & \cdots & \frac{\partial f_n}{\partial u_m} \end{bmatrix}_{ref}$$

where $|_{ref}$ means evaluated at the steady state operating point.

When applied to the sixth order model, the linear model becomes:

$$A = \begin{bmatrix} -2296.1 & 0 & 0 & 0 & 0 & 0 \\ 53.5 & -25.0 & 0 & -51.9 & 0 & .081 \\ 0 & 0 & -24.4 & 0 & 0 & -32000. \\ 0 & 0 & 0 & -983.4 & 0 & 145.3 \\ 21826.7 & 0 & 0 & -21173.7 & 7684.9 & 0 \\ 0 & 0 & 2. & 0 & 0 & 261.4 \end{bmatrix}$$

$$B = \begin{bmatrix} 2.9\times10^5 & 0 \\ 0 & 0 \\ 0 & 0 \\ 0 & 0 \\ 0 & 0 \\ 0 & 2.74\times10^4 \end{bmatrix}$$

where

$$\Delta x^T = \Delta DWFPO,\ \Delta SF2,\ \Delta PMFVD,\ \Delta DWFPF,\ \Delta PC,\ \Delta DWFNBP$$
$$\Delta u^T = \Delta FPOV,\ \Delta CCV$$

function. For example, the frequency bandwidth for thrust modulation will be significantly different than that for turbine inlet temperature spikes.

Actuator Dynamics

For most purposes, it can be assumed that actuator dynamics do not influence the system or plant dynamics significantly. This is equivalent to saying that the actuator dynamics are restricted to high frequency (large eigenvalue) regions that imply fast response. In most instances, the actuator dynamics are significantly "faster" than the plant dynamics. This is not true for the SSME. The fuel preburner oxidizer valve and the coolant control valve have open loop frequencies of -100 RAD/S, which is of the same order of magnitude as other system dynamics. Therefore, the actuator dynamics have been included in the overall design process. The eigenvalues and the corresponding eigenvectors are shown in Table 3. As can be seen, the eigenvalue corresponding to the combustion pressure ΔPc (7684.09 RAD/S) is positive, which implies a nonminimum phase situation. The smallest eigenvalue (-24.9 RAD/S) corresponds directly to $\Delta SF2$, the fuel turbopump speed. The complex conjugate pair of eigenvalues corresponds primarily to $\Delta PMFVD$, the main fuel valve discharge pressure. There is coupling between ΔPc, $\Delta DWFPF$, $\Delta DWFNBP$, and $\Delta PMFVD$. The eigenvalue that corresponds to DWFPO, the oxidizer flow rate, is coupled to the combustion temperature. The two actuator eigenvalues are located at -100 RAD/S. Mathematically, the control problem is to move the nonminimum phase (ΔPc) eigenvalue to the left of the real axis without triggering undamped oscillation of the oxidizer and fuel flow rates, which in turn causes the fuel preburner temperature to oscillate. The actuator dynamics can be approximated as a first-order process with a time constant of 10 ms. For control $\Delta u(t)$ and input $\Delta r(t)$, the differential equation is

$$\Delta\dot{u}(t) = -\frac{1}{\tau}\,u(t) + \frac{1}{\tau}\,\Delta r(t)$$

where τ is the time constant.

The perturbation model for the fuel preburner oxidizer valve ($\Delta FPOV$) and the coolant control valve (ΔCCV) is as follows:

$$\frac{d}{dt}\begin{bmatrix}\Delta FPOV(t)\\ \Delta CCV(t)\end{bmatrix} = \begin{bmatrix}-\frac{1}{\tau} & 0\\ 0 & -\frac{1}{\tau}\end{bmatrix}\begin{bmatrix}\Delta FPOV(t)\\ \Delta CCV(t)\end{bmatrix}$$

$$+\begin{bmatrix}\frac{1}{\tau} & 0\\ 0 & \frac{1}{\tau}\end{bmatrix}\begin{bmatrix}\Delta FPOVI(t)\\ \Delta CCVI(t)\end{bmatrix}$$

TABLE 3 -- EIGENVALUES OF AUGMENTED SYSTEM MATRIX A

EIGENVALUE (S-1)	CORRESPONDING EIGENVECTOR							
	DWFP0	SF2	PMFVD	DWFPF	PC	DWFNBP	FPOV	CCV
-24.9	0.0	1.0	0.0	0.0	0.0	0.0	0.0	0.0
7685.0	0.0	0.0	0.0	0.0	1.0	0.0	0.0	0.0
-983.4	0.0	.02	0.0	.4	1.0	0.0	0.0	0.0
-143.0 + 223.5i	0.0	-.002 +.002i	-0.9 +0.5i	.0003 +.001i	.0008 +.003i	0.0 +.008i	0.0	0.0
-143.0 - 223.5i	0.0	-.002 -.002i	-0.9 -0.5i	.0003 -.001i	.0008 -.003i	0.0 -.008i	0.0	0.0
-2296.0	0.5	-.01	0.0	0.0	-1.0	0.0	0.0	0.0
-100.0	0.0	0.0	0.0	0.0	0.0	0.0	1.0	0.0
-100.0	0.0	0.0	0.0	0.0	0.0	0.0	0.0	1.0

where $\Delta FPOVI(t)$ and $\Delta CCVI(t)$ are the inputs into the actuator. The augmented system and control matrices $\hat{A}$ and $\hat{B}$ respectively are:

$$\hat{A} = \begin{bmatrix} A & B \\ 6 \times 6 & 6 \times 2 \\ 0 & C \\ 2 \times 6 & 2 \times 2 \end{bmatrix}$$

$$\hat{B} = \begin{bmatrix} 0 \\ 6 \times 2 \\ T \\ 2 \times 2 \end{bmatrix}; \quad T = \begin{bmatrix} \frac{1}{\tau} & 0 \\ 0 & \frac{1}{\tau} \end{bmatrix} ; \quad C = -T$$

and 0 is the null matrix.

The linear model for the LQR design process discussed later is therefore:

$$\Delta\dot{x}'(t) = \hat{A} \quad \Delta x'(t) + \hat{B}\Delta u'(t)$$

where

$$\Delta x'^{t} = [\Delta DWFPO, \Delta SF2, \Delta PMFVD, \Delta DWFPF, \Delta PC, \Delta DWFNBP, \Delta FPOV, \Delta CCV]$$

$$\Delta u'^{t} = [\Delta FPOVI, \Delta CCVI]$$

Note that $\Delta FPOVI$ and $\Delta CCVI$ are perturbations away from some nominal operating condition for the actuator. No time lag is associated with the fuel preburner temperature and is considered to be a nonlinear function of the oxidizer fraction in the combustion chamber (ratio of oxidizer flow to oxidizer plus fuel flow):

$$TFP = \Gamma(FFP) + 277.4°R$$

$$FFP = \frac{DWFPO}{DWFPO + DWFPF} \frac{lbm/s}{lbm/s}$$

where

$$DWFPO(t) = \Delta DWFPO(t) + DWFPOref \quad lbm/s$$

$$DWFPF(t) = \Delta DWFPF(t) + DWFPFref \quad lbm/s$$

The steady state operating point corresponds to the following values for the state and control variables:

DWFPOref	= 75.55 lbm/s
SF2ref	= 3615.0 RPM
PMFVDref	= 5963.0 psi
DWFPFref	= 77.88 lbm/s
Pcref	= 2995 psi
DWFNBPref	= 65.48 lbm/s
FPOVref	= 79.0%
CCVref	= 99.9%

OPTIMAL CONTROL TECHNIQUES

INTRODUCTION

Generally, there are two methods of designing control systems -- the classical and the modern theory approach.[8] The classical approach usually deals with single-input, single-output linear systems in the frequency and Laplace or S-domains. The modern control approach, however, deals with multi-input, multi-output linear systems primarily in the time domain. It is the latter concept that is used herein.

The objective of modern control theory is concerned with finding a suitable control law usually optimized in some sense and then finding a controller configuration that will generate such a control law. The control law is not constrained to take on any particular form but for most purposes, it is taken so as to cause control deflections proportional to some error. Typically, the errors of interest are those due to differences in the actual value of variables describing the process such as pressure and flow rate and the values these variables take for some reference or equilibrium conditions; one might say the controls are deflected proportional to some perturbation away from the reference condition. The problem, therefore, is to select gains in such a manner that multiplying the errors by the feedback gains provides a control signal in such a manner as to maintain desired system characteristics, response and stability. The method used to determine these gains is based on linear system theory and because of its nature is called Linear Quadratic Gaussian Theory (LQG).[1]

The LQG design procedure is basically a three point procedure:

1. Deterministic Ideal Response Analysis and Design

Step 1 involves modeling the physical situation in the form of a set of mathematical equations. Usually these equations are nonlinear and must be linearized as discussed previously. This model assumes no uncertainty in the modeling of the plant (physical situation) or measurements. Exact measurement of all

plant state and measurement variables is assumed. Actuator and plant dynamics are also assumed to be known exactly. The SSME deterministic model formulation describes the behavior of the fuel preburner state and measurement variables as well as the interaction of the thrust (combustion pressure) with changes in fuel preburner flow rates. The preburner temperature taken here as an auxiliary variable, is assumed to be a nonlinear function of the oxidizer fraction in the combustion process and the fuel temperature in the lines. For design purposes, this nonlinear equation is used to calculate fuel preburner temperatures. The dynamics of the temperature are of such high frequency, that this dynamic effect can be ignored. The measurement or output variables will be the pressure and volumetric flow rate measured at the fuel flowmeter.

2. Stochastic Estimation Analysis and Design

Step 2 introduces uncertainty into the linear model to compensate for linearization errors as well as errors due to nonlinear model uncertainty. Most plant variables in a real system cannot be directly measured by conventional techniques. Therefore, a state filter or observer[9,10] is used. Not only are plant variables assumed uncertain but sensor errors are also assumed in error. These errors are described statistically by intensity matrices of covariance[10].

3. Stochastic Feedback Control System Design

From Steps 1 and 2, an optimal control correction from the estimated state deviation (error) is derived. The controller is then tested in the linear system to determine how good the control gains are in meeting design goals.

In general, a control system is designed for each set of linearized equations that describe the dynamics of the SSME in the neighborhood of several equilibrium conditions. For this particular problem, the mixture ratio of 6:1 at rated power level (RPL) is of interest and hence is used as the reference condition about which to implement the controller design. The technique for designing the control system is the previously mentioned LQG theory, which provides a somewhat systematic method for determining a set of feedback gains. In most cases, the design for each steady state condition yields a set of unique feedback gains. The resulting designs are then tested by observing the time responses to typical input commands. In this case, these commands consist of a step-type combustion pressure (thrust) or preburner fuel and oxidizer flow rate changes.

THE OPTIMAL REGULATOR

Introduction

For the SSME design point discussed previously dealing with the SSME hybrid model, a Linear Quadratic Regulator (LQR) design is carried out that provides state feedback gains to the control to minimize some cost function.[11] The LQR controller always provides a control law that will drive perturbations or errors from the ideal state and control variables to zero. It must be understood by the designer, however, that the LQR formulation does not allow constraints to be put on the control or state variables. Such constraints, however, can be applied indirectly by the designer in the design process. In general, the LQR design procedure selects feedback gains in such a manner as to minimize the "cost" of the process in a rigid mathematical sense.

In the following sections, the general formulation of the LQR design problem is presented. In addition, a procedure will be discussed that will allow the designer to "constrain" selected variables in order to stay within the prescribed limits of the engine.

The Regulator Design As A Tracking Controller

The LQR problem centers on designing a controller that keeps errors or perturbations small. However, the real problem of interest is that of carrying out step changes in the main combustion pressure, fuel and oxidizer flow rates in the fuel preburner in a reasonably short time while retaining good dynamic characteristics and at the same time not exceeding specified engine limits. Although these two problems appear different, they can be cast into the same form as will be shown. If the engine is operating at one steady state reference point and it is desired to change to another point, the regulator control can be used by simply changing the steady state reference point. Since the regulator tends to drive all errors to zero, it will drive the engine to the new operating point with new steady state conditions. For example, suppose it is desired to change the thrust level in 1% increments. For the various thrust levels, there will be a unique set of steady state operating conditions, as shown in Figure 4. This new set of steady state operating points will then be substituted in place of the old reference points. The change in the variables in the system will then be driven to zero, and hence the engine will be driven to the new operating point (new thrust level).

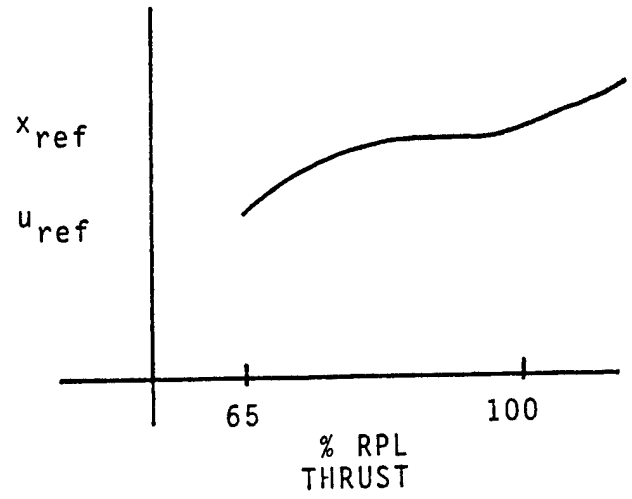

Reference or Desired Variable as a Function of Thrust

Figure 4

The 'reference map' will be stored in the computer as a curve fit or table. Note that thrust is assumed as the independent variable because the space shuttle guidance computer commands a thrust change. It is possible that the reference variables could be a function of other independent plant variables like mixture ratio, for example. It must be remembered, however, that the ability of the LQR controller to accomplish this task is a function of how well the linear and nonlinear model correspond at the steady state reference point. It is possible that a 1% change in the reference condition may exceed the neighborhood about which the linear perturbation model is valid. In that case, other perturbation models must be designed that describe the motion. This 'trim map' methodology of designing feedback gains for various operating conditions is well known. Of course, the necessity of designing new linear models depends on how the linear and nonlinear transients correspond, given the same initial conditions. It is intuitively obvious that 'small' changes will yield good correlation; it is also true, however, that large changes say 10% of the steady state values, may yield results that do not represent the dynamics. There are no easy methods of determining the linearized 'neighborhood' mentioned above other than nonlinear simulation. Hence, although a regulator design is being considered, a tracking controller can be implemented simply by varying the reference control in some prescribed fashion such as a step change used here, or possibly a ramp, sinusoid or some other form.

Mathematical Formulation [11]

Briefly stated, we wish to find a control law that will minimize a cost or penalty function.

$$J = \frac{1}{2} \int_0^\infty (\Delta x^T Q \ \Delta x + \Delta u^T R \ \Delta u) dt \qquad (1)$$

where $Q \geq 0$ and $R > 0$ and hence drive perturbations in x and u to zero. This cost function is subject to the constraint that the variables Δx and Δu must satisfy the differential equations

$$\Delta \dot{x} = A \ \Delta x + B \ \Delta u \qquad (2)$$

where A and B are constant system and control matrices, respectively. A quadratic cost functional as above is chosen because it penalizes large errors much more severely than small errors. As is clearly seen, the first term in Equation (1) penalizes errors in the state and the second term deviations away from the reference conditions for the control. There are two main reasons why Equation (1) is used. They are that it is mathematically tractable; that is, the theory has been well established, and also that it leads to optimal linear feedback systems.

The solution to the problem of minimizing Equation (1) subject to Equation (2) is given by a constant linear feedback matrix K so that

$$\Delta u(t) = -K \ \Delta x(t) \qquad (3)$$

where $K = R^{-1}B^T S$ and $S > 0$ satisfies the steady state matrix Riccati equation.

$$-SA - A^T S + SBR^{-1} B^T S - Q = 0$$

Existence of a unique positive definite solution to the LQR control problem is guaranteed provided the nxmn "controllability matrix"

$$[B : AB : \cdots\cdots : A^{n-1}B]$$

has rank n where n is the dimension of the A matrix and m is the number of controls (columns in the B matrix).

Procedure

In general, the procedure for using the regulator method can be divided into three main steps:

1. The Q and R weighting matrices must be selected for the cost functional. In Equation (1), note that Q must be a positive semi-definite matrix while R must be a positive definite matrix.

2. The gain matrix K must be determined by solving the matrix Riccati equation (4) for the matrix S and substituting the result in Equation (3).

3. The resulting control law must then be incorporated into the original system and tested. In general, this step is carried out in two substeps. Initially, the controller design is tried in the linearized system for which it is designed, and if satisfactory characteristics are achieved, it is then tried in the original nonlinear system. Most often, this controller verification step is carried out using digital simulations of the linear and nonlinear systems on a high speed computer.

Although appearing straightforward, this procedure is not without some difficulties. In particular, problems can be encountered selecting the elements of the weighting matrices in the cost function Q and R. Generally, only the diagonal elements are used with first guesses equal to approximately $1/\varepsilon^2$, where ε is the maximum desired error in the variable associated with that term. Here then, is where the designer can initiate considerations for constraints on the state and control variables; that is, they determine a "ball park" number for ε. Most likely, however, step 3 reveals a dynamic response of the controlled or closed-loop system that is not that desired, and adjustments of the weights are necessary. Oftentimes, in order to avoid unnecessary computer simulations of Step 3 as an aid to selection of Q and R weighting matrices, the eigenvalues from the closed-loop system are used to determine various performance characteristics such as rise time, time-to-half amplitude, etc. If these characteristics are favorable, that is, if the closed-loop system response is "fast", then the system response is simulated on a computer. If the closed-loop system is "slow", then the weights are changed to achieve a faster response. The fast and slow designations are related to the relative time it takes to achieve a steady state condition.

A method that proves to be successful in choosing the Q and R weighting matrices is to change the diagonal terms one at a time and note changes in the closed-loop system characteristics (eigenvalues). Each new system is simulated on a computer to give an indication of how changing one element at a time in the Q and R matrices changes the closed-loop time responses.

As mentioned earlier, the vehicle limits are not part of the LQR problem. They are, however, part of the overall design process. Because this system will be used as a tracking controller, some quick checks can be made to determine if the controls will exceed their prescribed limits for a given design. Since, for a step change in main combustion pressure (flow rates), all the states except for the biased variable will be

zero, the initial control deflections can be determined by multiplying the feedback gain corresponding to the pressure change required by the desired change. The resulting control deflection should be within the vehicle control limits. If the control limit is exceeded, then the element corresponding to the control in the R matrix is increased. This, in effect, penalizes the control.

In general, increasing diagonal elements in the Q and R matrices tends to penalize the variables corresponding to those elements. Therefore, in order to limit a state variable, increase the diagonal element in the Q matrix corresponding to that state variable. In order to limit a control variable, increase the diagonal element in the R matrix corresponding to that controlled variable.

This trial and error approach, augmented by the knowledge of which errors are not important, all come into play when selecting weighting matrices. In any case, a regulator solution and hence, the corresponding feedback matrix yielding desirable closed-loop system dynamics can be obtained with patience.

CONTROLLER DESIGN

INTRODUCTION

The Linear Quadratic Gaussian control scheme as discussed previously is a relatively simple controller to implement in a computer control system once the linearized models are obtained. For this paper, only the LQ regulator design methodology and implementation will be discussed. The addition of the Kalman-Bucy filter is not difficult and the overall "marriage" of the optimal state feedback with the Kalman-Bucy filter can be found in any text on linear optimal control.[12]

The design point of 100% rated power level with the reference conditions for the six states and two controls is used as a design point to determine a feedback matrix, not necessarily the only one, that will produce the desired behavior in the neighborhood of the design point. Ideally, one would like all the feedback matrices found to be the same so that a constant gain system results. In most cases, however, the feedback matrices are different. Consequently, either some scheme must be incorporated into the controller that senses the engine's state and condition or some alternate scheme must be developed. Although there are several variations of gain scheduling techniques, most require some method of estimating states and parameters (Kalman-Bucy filter).

The LQ regulator gains are found from the commanded thrust, which is commanded by the space shuttle guidance computer. From simulation studies, a 'trim map' of state and control

variables as a function of thrust level can be used to 'trim' or drive the system to the new thrust level. For different thrust levels, there will be a unique set of reference values for the state and control variables. Theoretically, if the full set of actual state and control values are at a reference condition, the thrust level should be unique. Therefore, if the computer commanded a 1% change in thrust level from say 65% RPL, the computer would search a set of steady state or reference state and control variables that are curve fitted or in table form for the commanded or desired values of these parameters needed to drive the system to the new commanded thrust level. The feedback gains will then drive the system to the new state and control, and hence to the commanded thrust level.

The LQ gains are found from a curve-fit or table lookup of the gains versus the thrust level. For small changes in thrust level, the gains should vary smoothly. Although there is no guarantee that this will occur, it has been found for vehicle control that LQ gains will vary in a smooth manner if the state and control weighting matrices do not need large adjustments for good control.[13]

The LQ gains determined for the design point model discussed in this paper were found using ORACLS.[14] This package is well-known among the modern control community and will not be discussed. The use of this package of routines, however, is recommended because of its simplicity in accessing various matrix manipulation and LQG design algorithms.

The following sections discuss the controller design for the fuel preburner linear system derived previously. A section discussing controller implementation as well as linear simulation results is included. Also, the effect of limiting the control in the linear simulations is discussed.

LINEAR MODEL SELECTION

From past studies, it was determined that fourteen states and five controls present in the SSME could be used to develop a linear model to describe the engine throughout the flight envelope. However, since the control objective was to control preburner temperatures, it was decided to concentrate on the fuel preburner since thermal spikes there are more severe. Further modeling experience indicated that only nine state and three control variables could have any dynamic effect on fuel preburner temperature. From an eigenstudy of the open-loop dynamics of the system, it was found that certain states had virtually no effect on preburner temperature because of the high frequency character of their associated eigenvalues. It was also discovered that the associated eigenvector was dominated by that state. Intuitively, this means that the particular state at a high frequency equilibrates long before other variables in the system. (This type of analysis can be thought of

as modal decomposition since the system matrix yielded no repeated eigenvalues and hence the Jordon matrix[15] is just the matrix of eigenvalues.)

After eliminating the row and column in the system matrix, the eigenvalues and eigenvectors were calculated again. In the variables deleted from the linear model representation, it was found that all high frequency dynamics were eliminated. It was also discovered that the states needed for the fuel preburner temperatures did not have the same frequency level as the deleted states. The final linear system contained six state and two control variables. It was discovered later, however, that the actuator dynamics associated with the two controls were in the same frequency range as the plant dynamics. Since there is no direct coupling between the actuator equations and the plant equations, the actuator poles were simply negative of the inverse of the actuator time constant (e.g., $-\frac{1}{\tau}$) taken as 10 ms. The resulting eighth order system was used for the controller design model.

As previously discussed, the effectiveness of the control law depends primarily on how well the linear system represents the dynamics of the nonlinear system, since it is almost certain that linear systems found from nonlinear simulations will be inaccurate due mainly to the fact that the nonlinear simulations cannot describe all dynamic variations. Also, since the linear models are not of full-order, i.e., all the state and controls possible are not used, the linear control law derived will yield some steady-state error. Although this error should not be severe, it might be advisable to include elements of further compensation in the controller. The easiest method to implement is to implement trim integrators on those states exhibiting steady state error. This amounts to integrating the steady state error over time and multiplying that by an integral gain.

SINGLE POINT LQR DESIGN

Since this study is a feasibility study into the applicability of the LQG technique toward preburner temperature control, only one reference or design point was chosen about which to derive a linear model. The typical design strategy for this design point linear system is to choose a set of Q and R weighting matrices. Realistically, a real controller must incorporate gains found for a 'trim map' of the engine operating range (e.g., varying thrust levels). For design points that are relatively 'close' to one another, a 'middle' design point can be used to determine a set of Q and R weighting matrices that can be used over the entire set of operating points to design control laws. The LQR design for the one design point was carried out using the method described previously.The resulting optimal design shows that a step change in Pc (main combustion pressure), which corresponds to a change in thrust level with

all other deviations zero, resulted in good dynamic behavior especially as the model dynamics influence the fuel preburner temperature. The linear system simulation run for a Pc chance from nominal of -10 psi for a time interval of 0 to .1 s is shown in Figure 5. For Pc changes greater than -10 psi, multiple step changes could be made until the required step change is made. From iterations on the Q and R diagonal weighting matrices, a final set of gains was found using the weights

$$Q = 1.0,\ 1.0\cdot10^{7},\ 1.0,\ 1.0,\ 1.0\cdot10^{5},\ 1.0\cdot10^{3},$$
$$R = 1.0\cdot10^{6},\ 1.0\cdot10^{3}$$

The eigenvalues from the closed-loop system show considerable improvement over those of the open-loop, as can be seen below:

EIGENVALUES

OPEN-LOOP (s^{-1})	CLOSED-LOOP (s^{-1})
-24.9	-190.0
-142.9 + 223.5i	-951.0 + 130.0i
-142.9 - 223.5i	-951.0 - 131.0i
-983.4	-1145.0 + 1285.0i
-2296.1	-1145.0 - 1285.0i
7684.9	-3323.0 + 3625.0i
-100.0	-3323.0 - 3625.0i
-100.0	-8266.5

The gains are:

	ΔDWFPO	ΔSF2	ΔPMFVD	ΔDWFPP	ΔPC
ΔFPOVI	-7.23	2.73	$-8.04\ 10^{-6}$	7.86	-3.46
ΔCCVI	2.56	1.65	$2.81\ 10^{-2}$	-3.1	1.075

ΔDWFNBP	ΔFPOV	ΔCCV
.107	-204.	.156
-1.59	156.	-28.2

The improvement is mainly in speed of response since the eigenvalues have been moved to higher frequencies. The positive open-loop pole (7684.9 s^{-1}) has been eliminated in the closed-loop system. The closed-loop system eigenvalues show complex conjugate pairs. These eigenvalues, however, appear to be well-damped, as can be seen in the simulation results. One

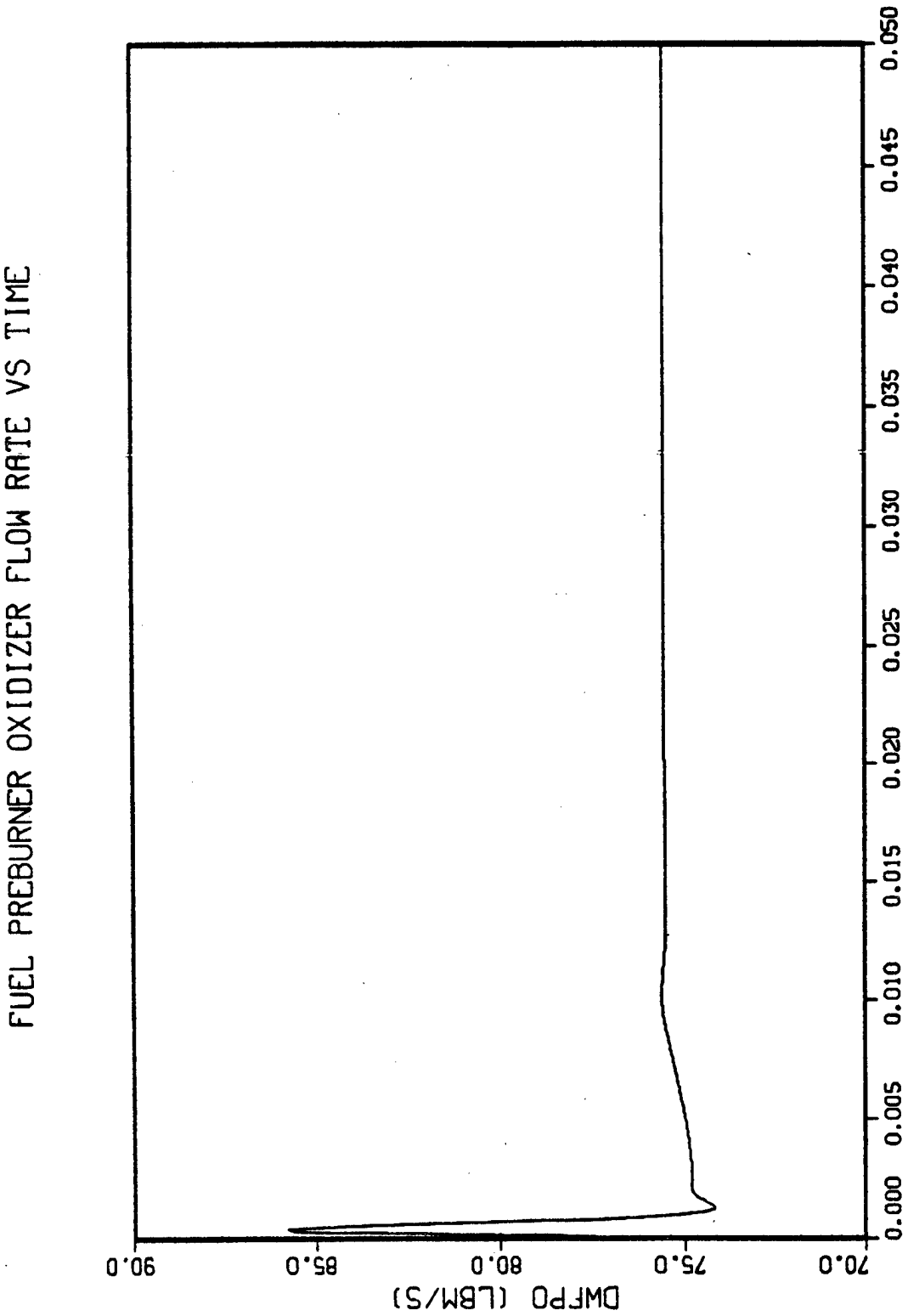

FIGURE 5 -- LINEAR SIMULATION RESULTS

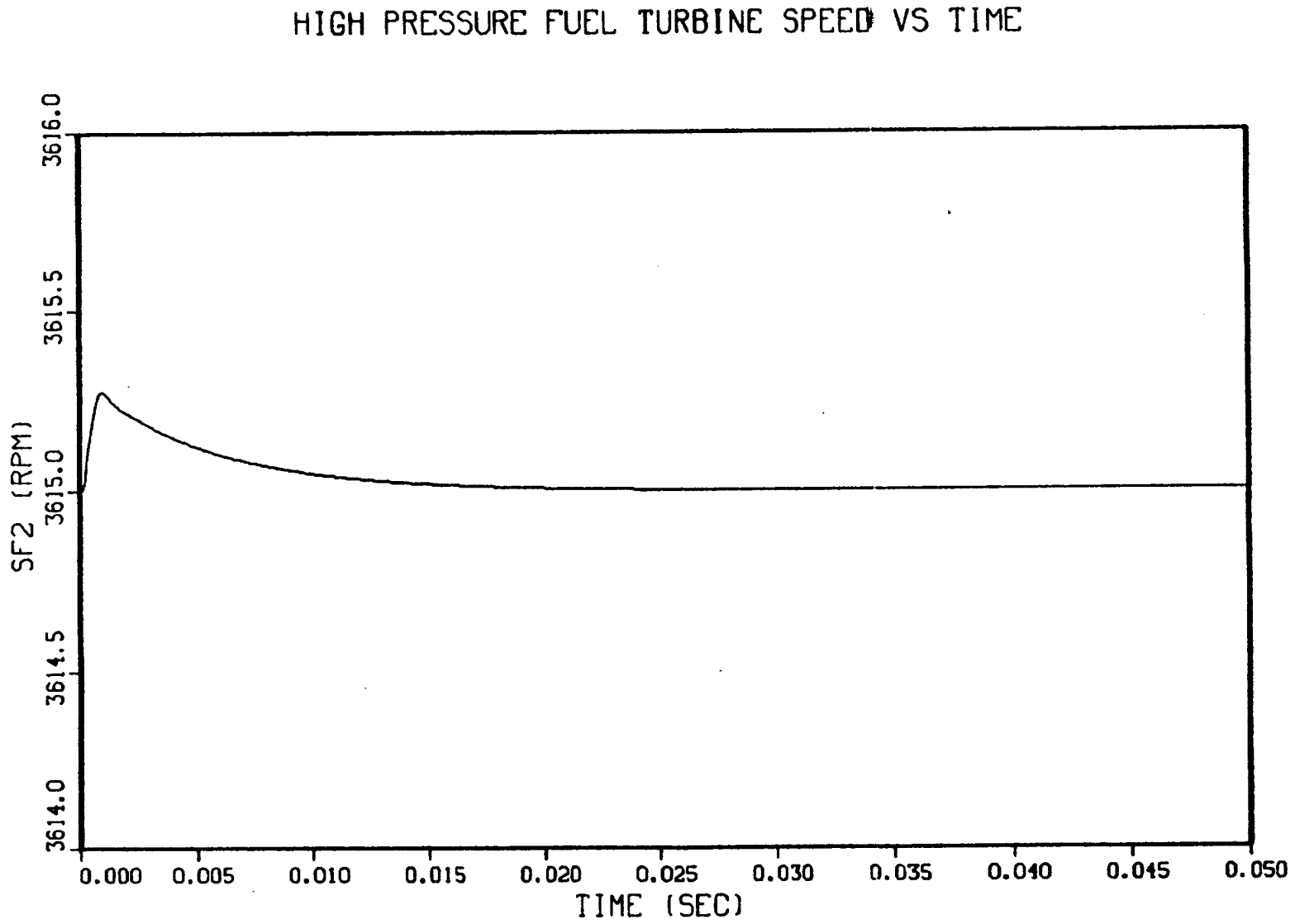

FIGURE 5 -- LINEAR SIMULATION RESULTS (CONTINUED)

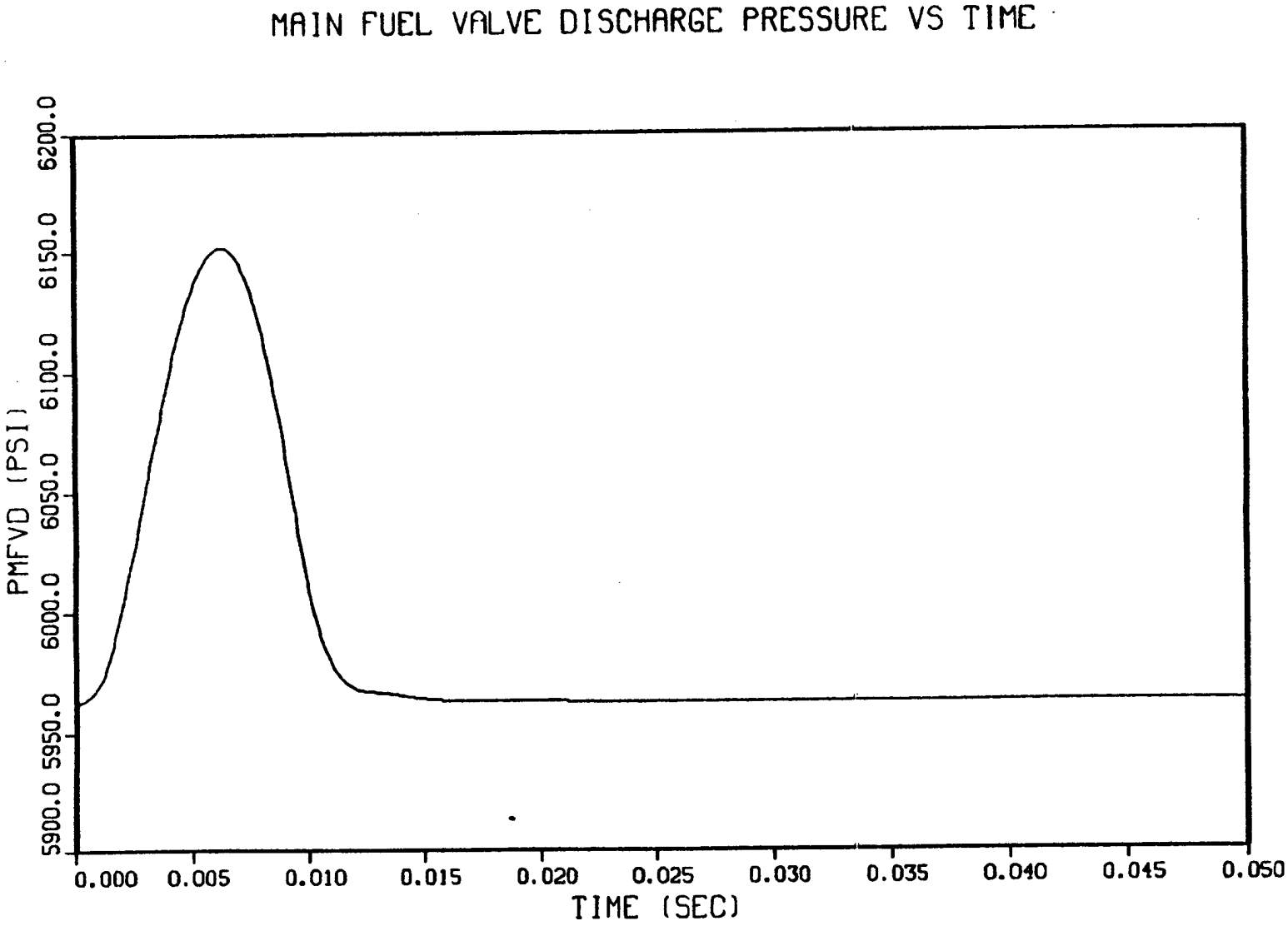

FIGURE 5 -- LINEAR SIMULATION RESULTS (CONTINUED)

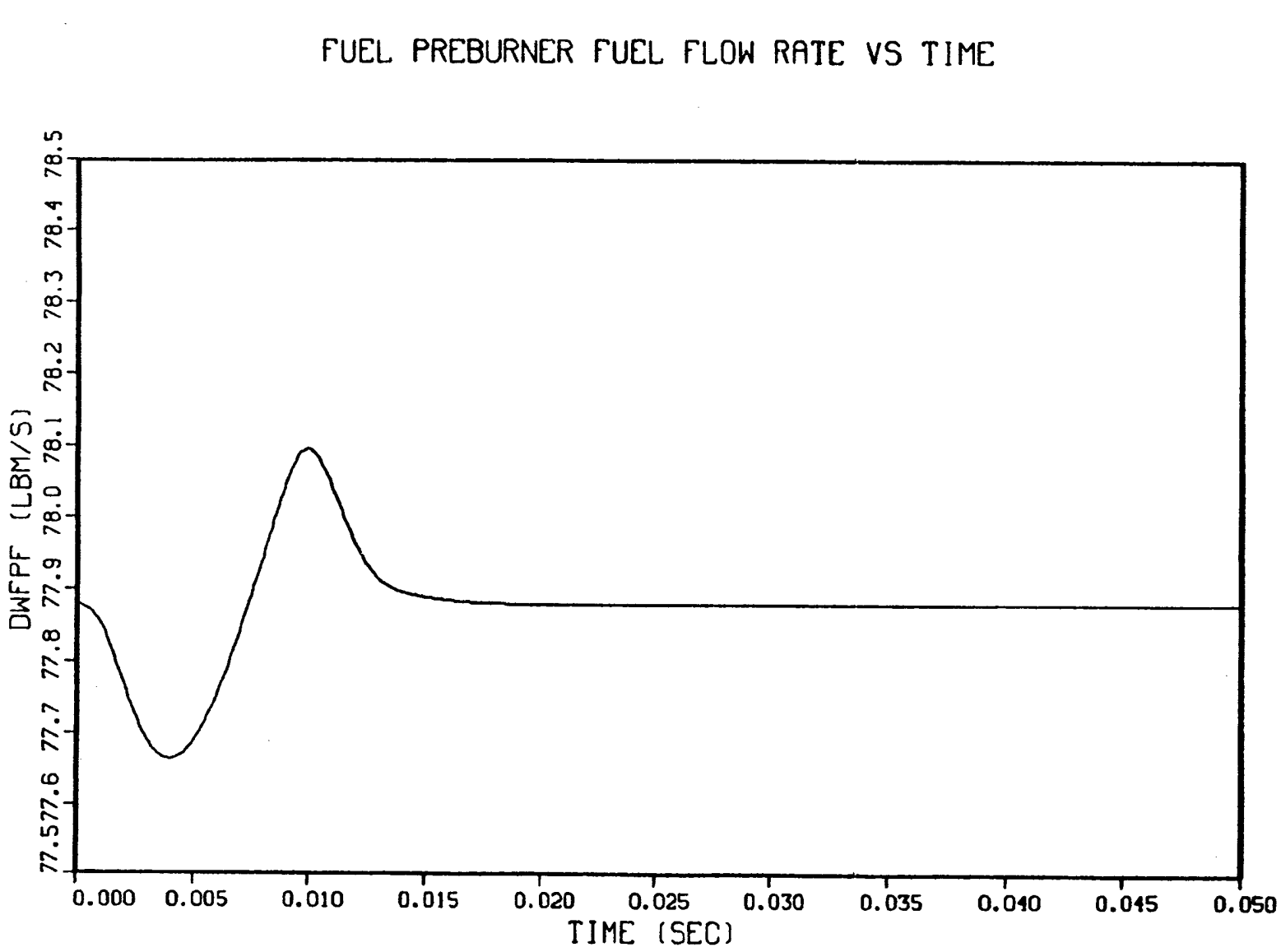

FIGURE 5 -- LINEAR SIMULATION RESULTS (CONTINUED)

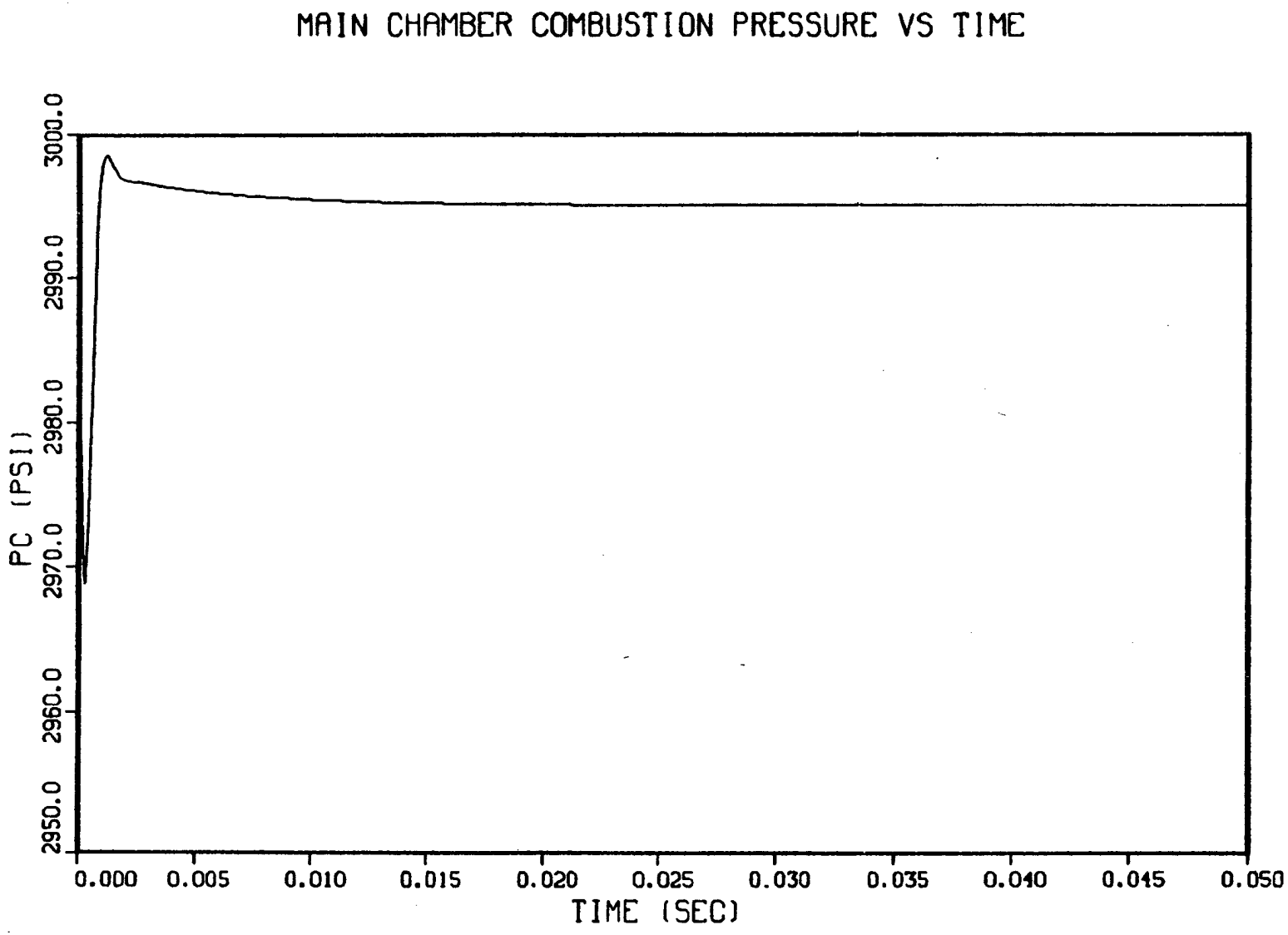

FIGURE 5 -- LINEAR SIMULATION RESULTS (CONTINUED)

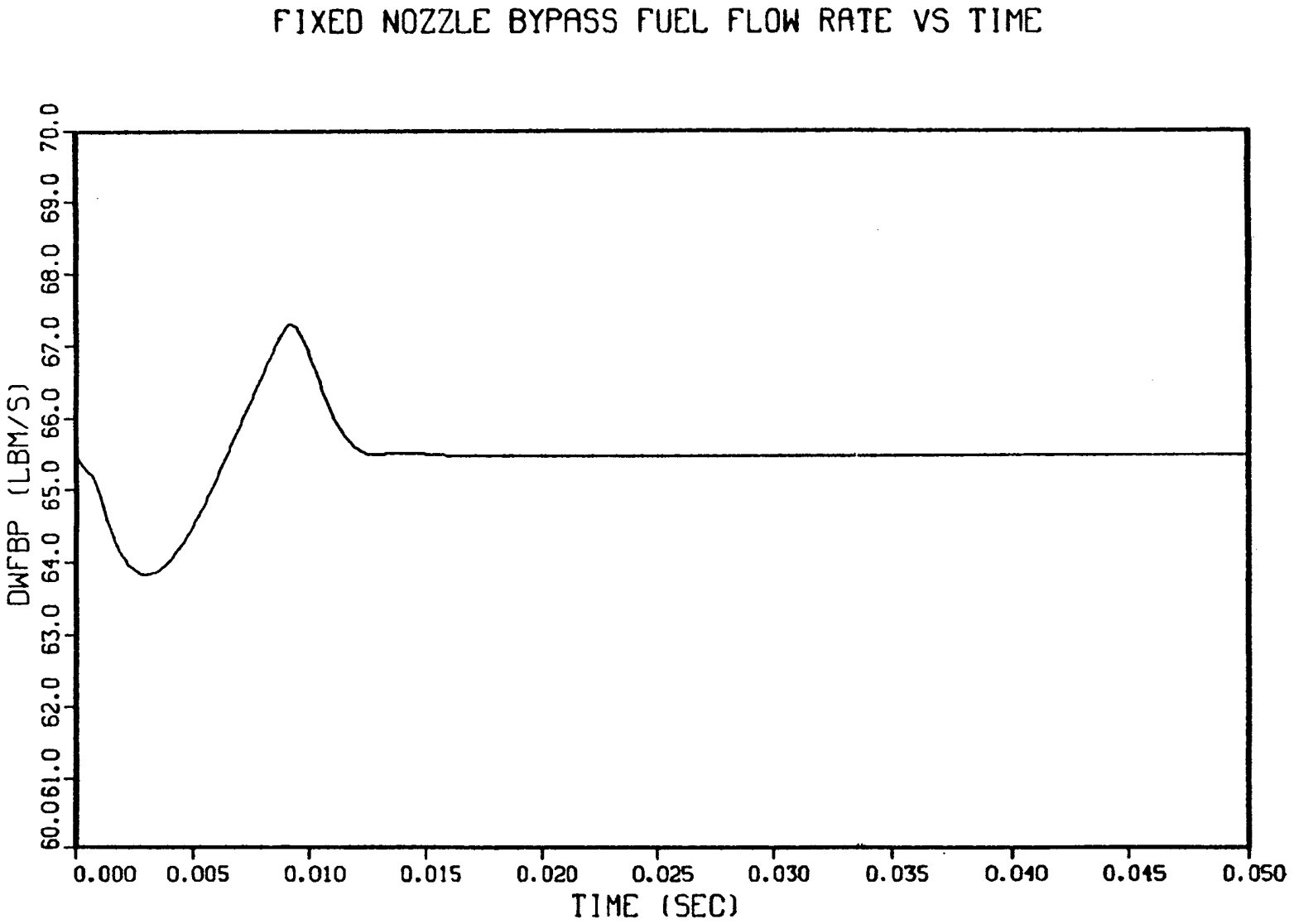

FIGURE 5 -- LINEAR SIMULATION RESULTS (CONTINUED)

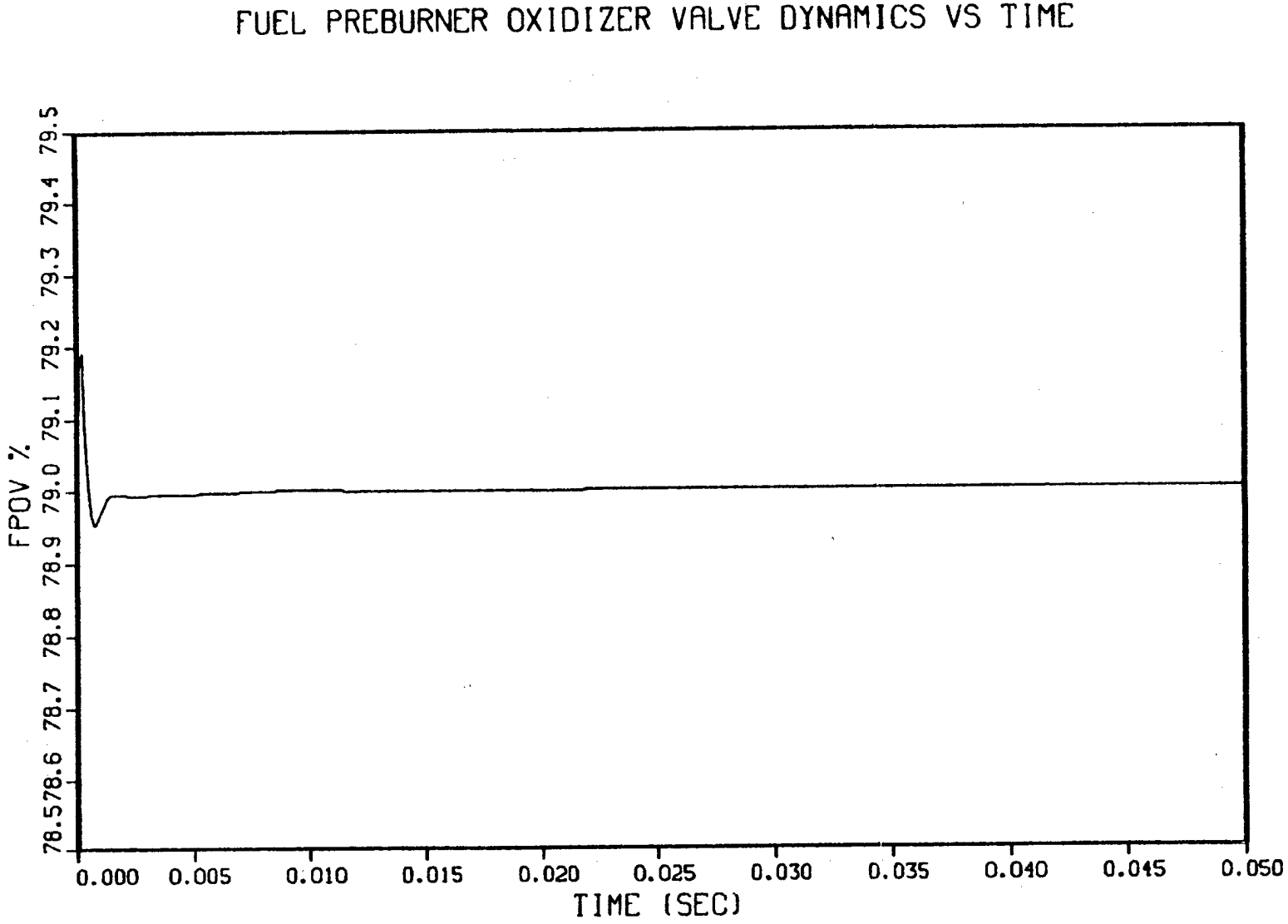

FIGURE 5 -- LINEAR SIMULATION RESULTS (CONTINUED)

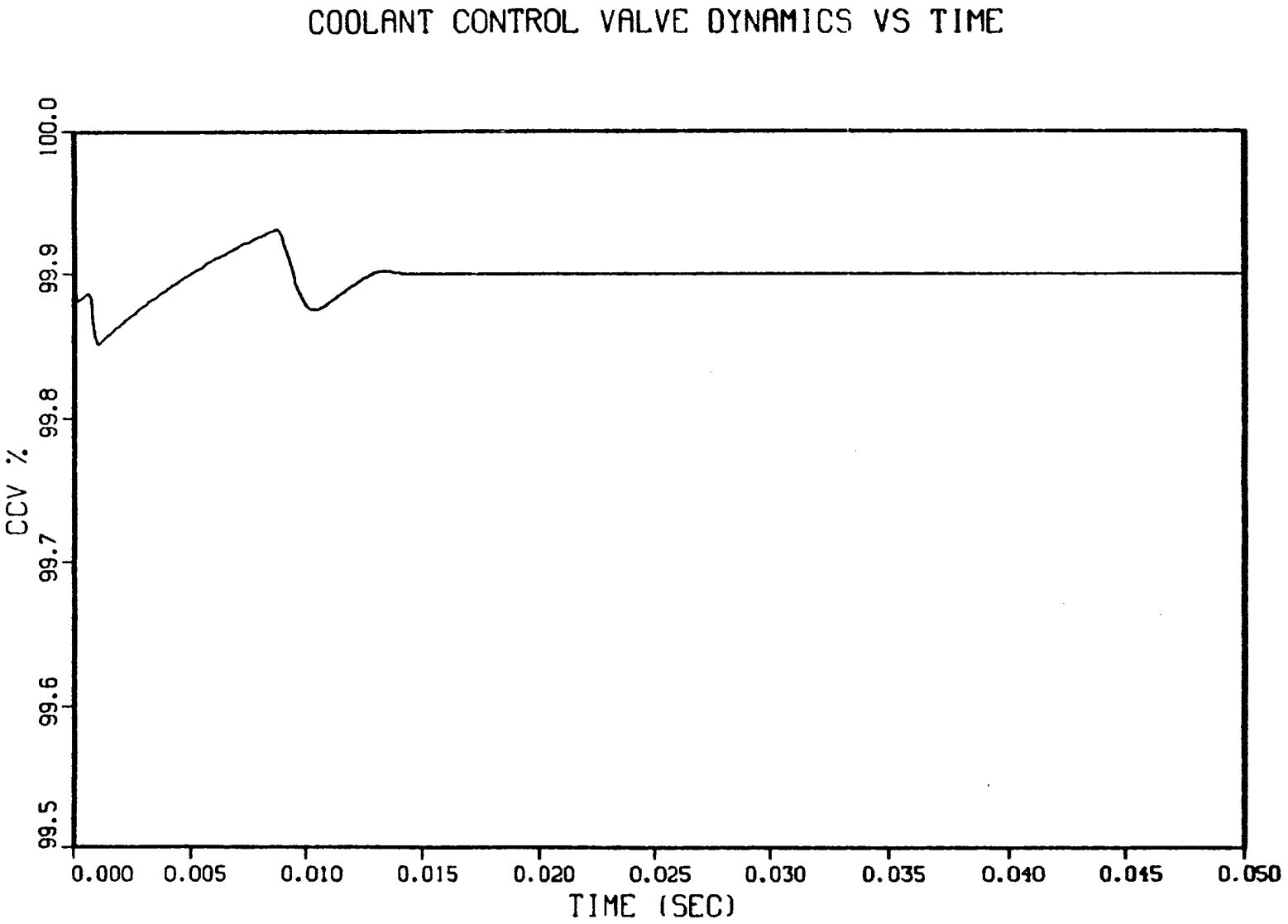

FIGURE 5 -- LINEAR SIMULATION RESULTS (CONTINUED)

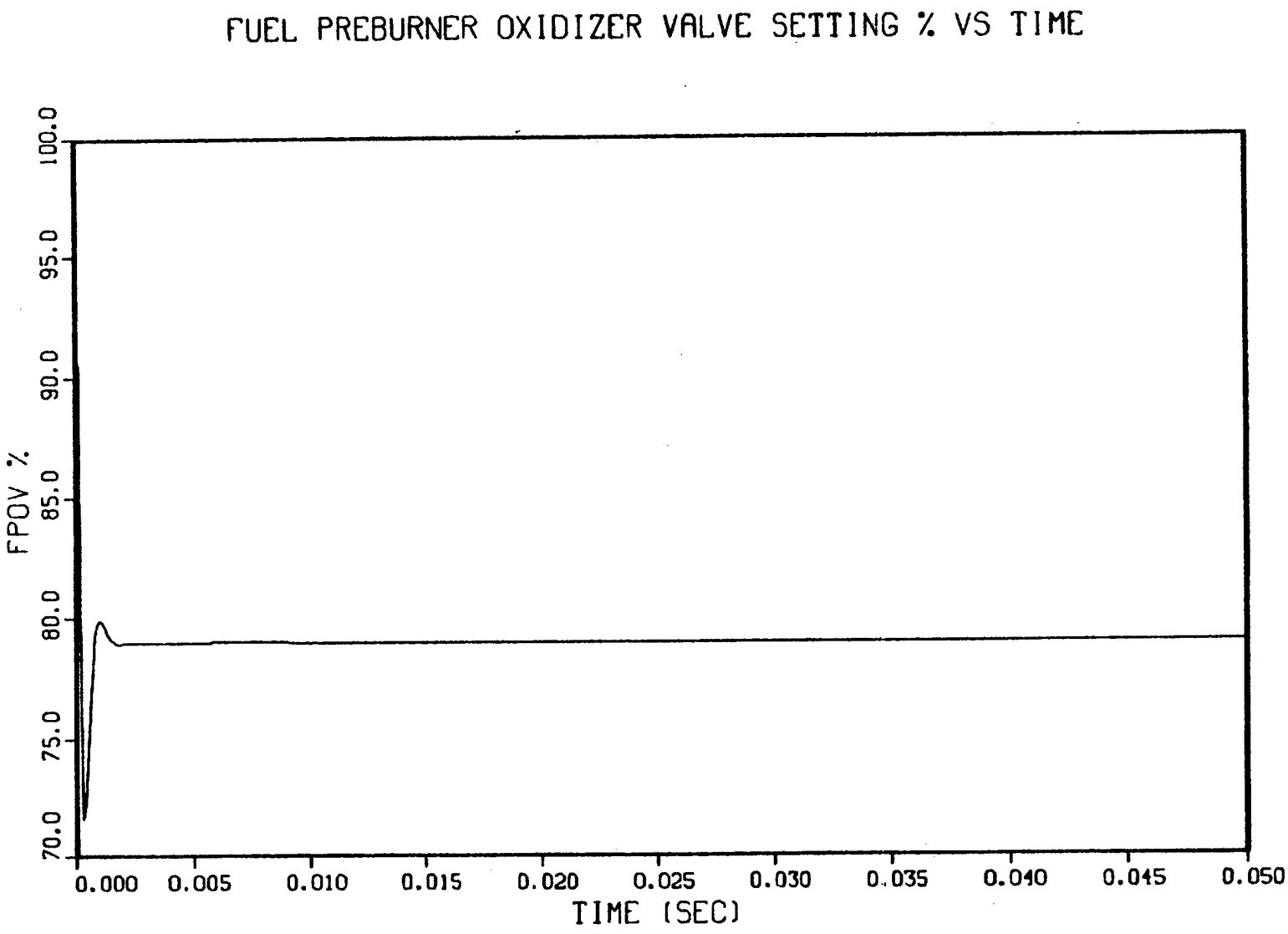

FIGURE 5 -- LINEAR SIMULATION RESULTS (CONTINUED)

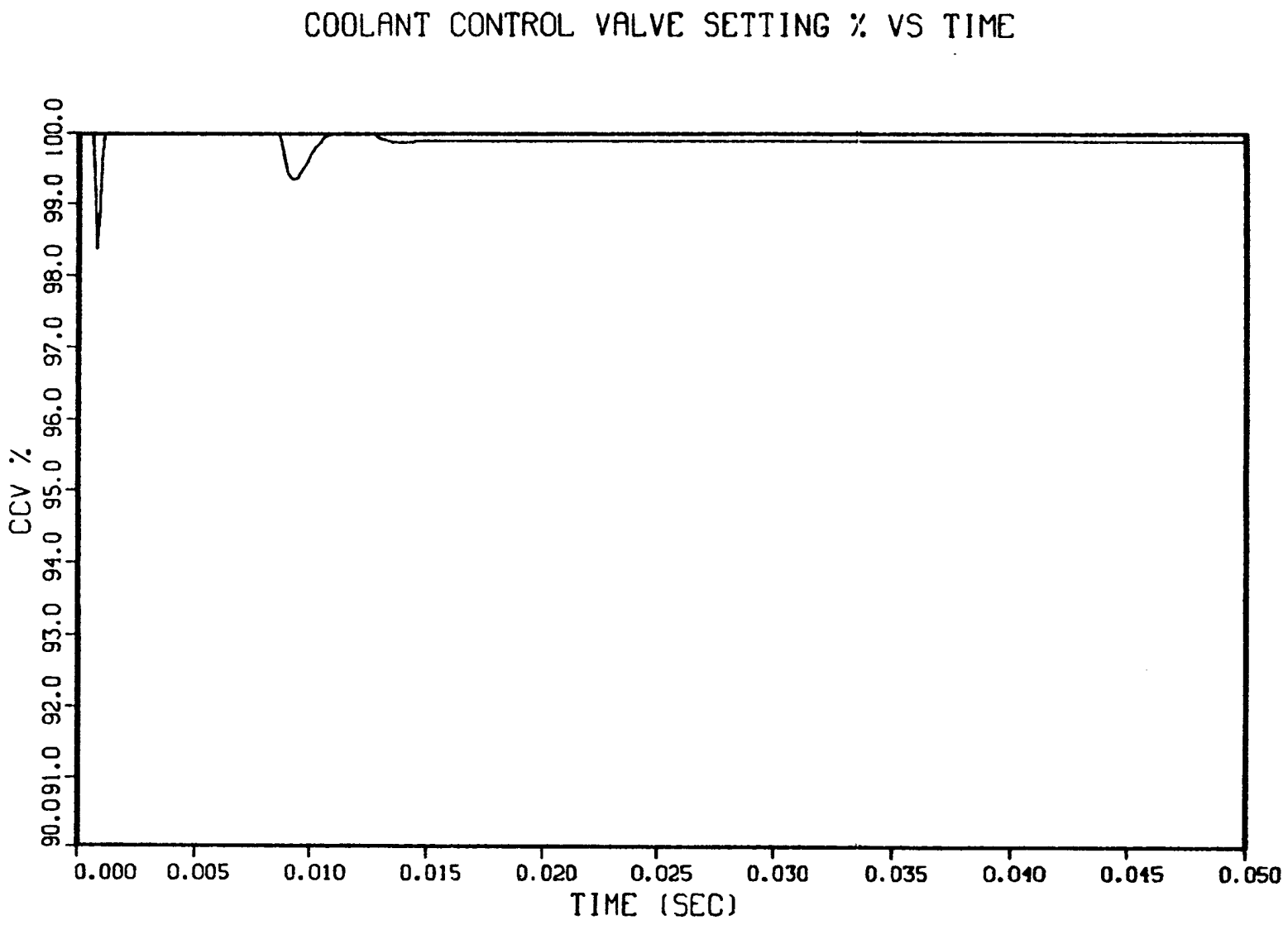

FIGURE 5 -- LINEAR SIMULATION RESULTS (CONTINUED)

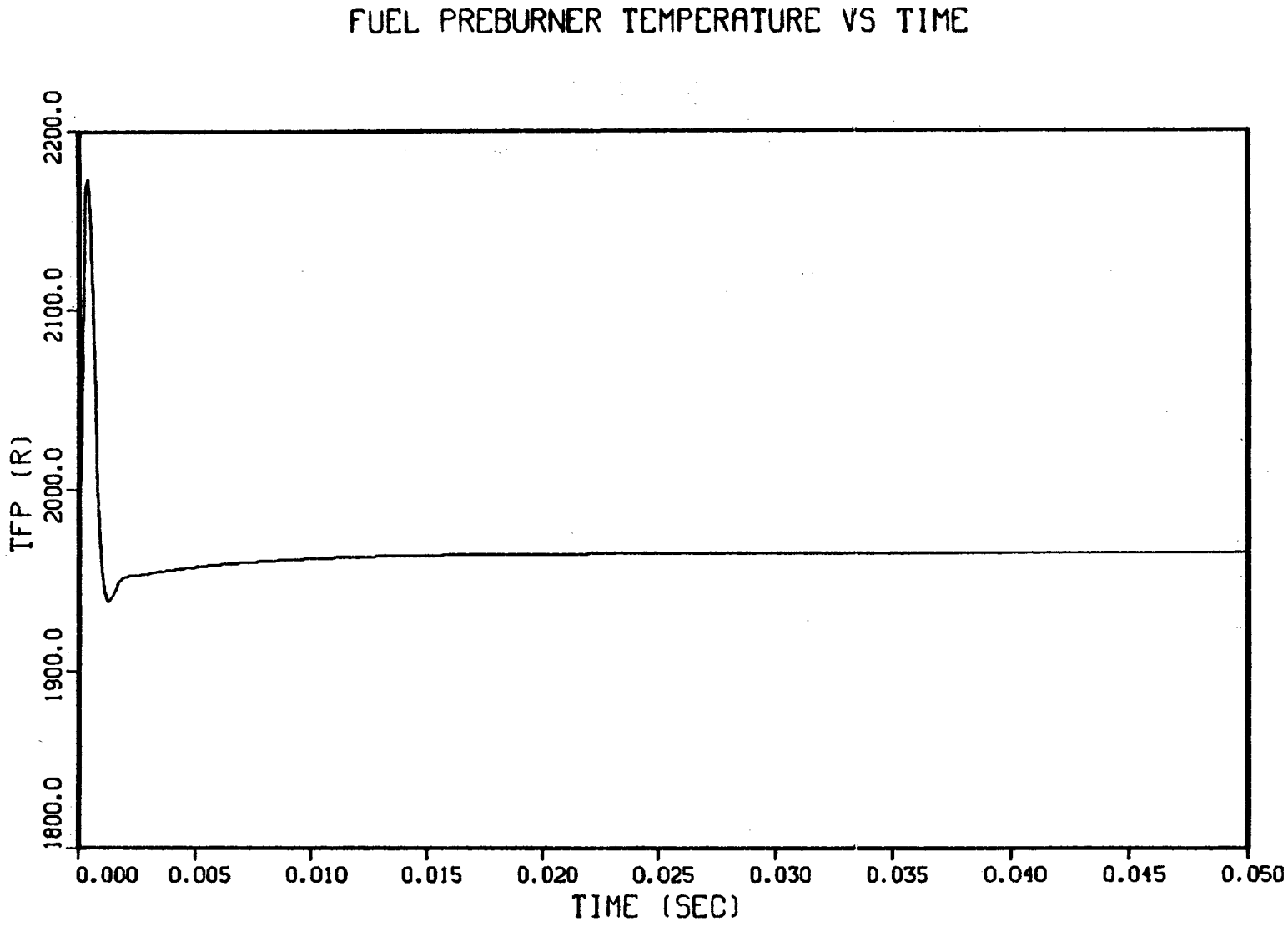

FIGURE 5 -- LINEAR SIMULATION RESULTS (CONTINUED)

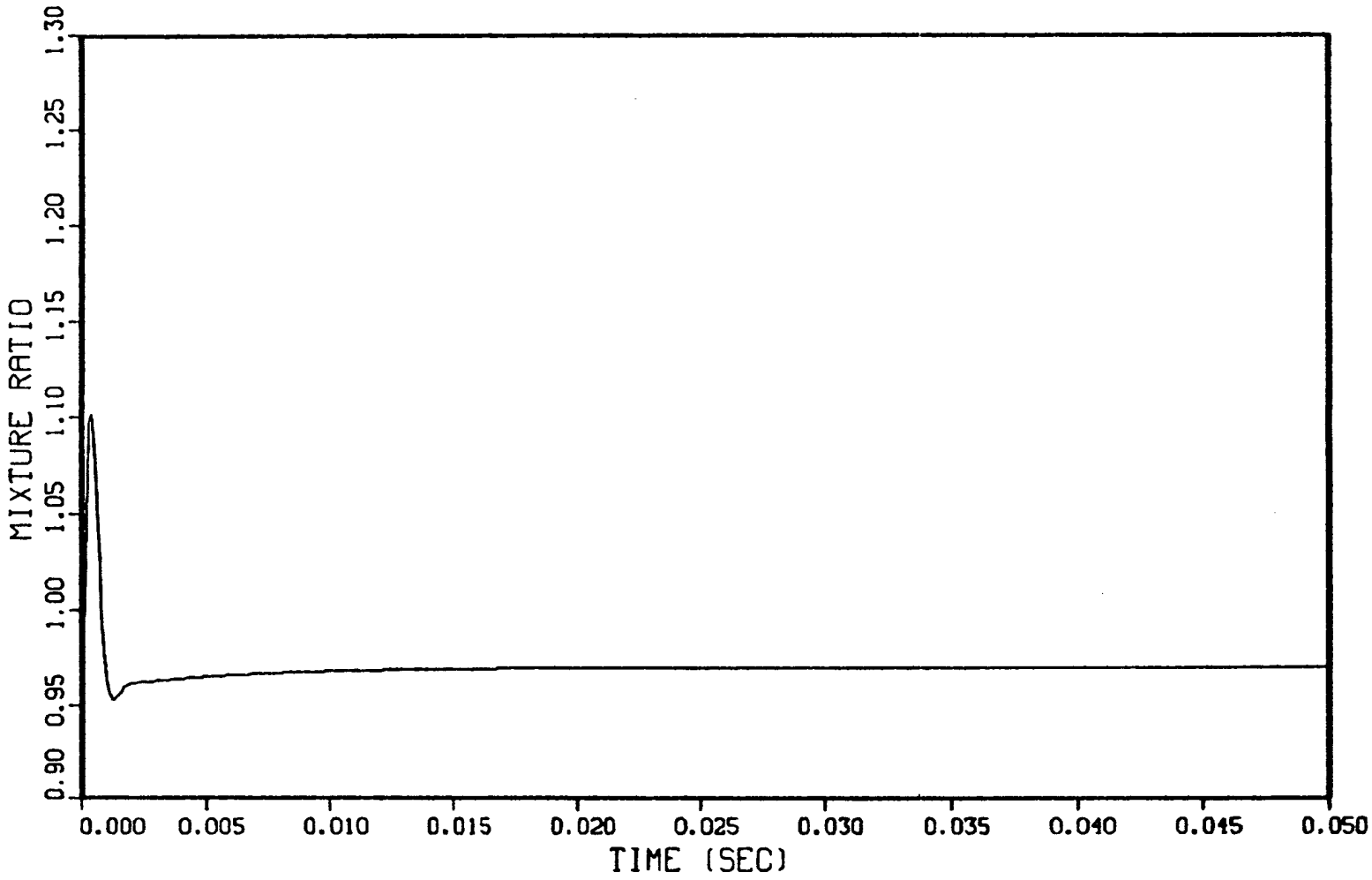

FIGURE 5 -- LINEAR SIMULATION RESULTS (CONTINUED)

of the major goals in this study is to control fuel preburner temperature through oxidizer and fuel flow rate control. Since fuel flow is difficult to regulate at this operating point (i.e., the coolant control valve is 99.9% open, which implies maximum fuel flow rate), fuel control will yield minimal effect on preburner temperature.

The actuator dynamics significantly affect closed-loop response, since commands from the feedback control law do not have enough time to reach their steady state values before the next control command is input. A relatively large commanded change in valve position will not be seen in the actuator dynamics response, since there is not enough time for the valve to respond (e.g., 10 ms time constant). This effect can be seen directly by comparing the graphs of the fuel preburner oxidizer and coolant control valves setting commands with the corresponding actuator response. For large perturbations, a nonlinearity due to saturation of the valve limits the amount of valve movement that can be accomplished.

The maximum oxidizer flow rate amplitude is about 10 lbm/s, which shows up as a temperature increase of about 200°R. However, since the oxidizer flow rate changes damp out in about .03s, the preburner temperature also damps out as fast.

As the coolant control valve position is increased from 99.9%, the main fuel valve discharge pressure increases. However, the CCV limit of 100% full open causes saturation of the valve setting, which causes oscillation in the fuel flow rate. But, since the amplitude of the oscillation is about 0.5 lbm/s, the effect on fuel preburner temperature is minimal. A small 'ripple' can be seen in the temperature transient in the first 10 ms. The commanded change in main combustion temperature of -10 psi is damped out in about 5 ms, although an overshoot of 2 psi can be seen. The other transients associated with fuel flow rate, DWFNBP, DWFPF and SF2 damp out in 2 ms, the mixture ratio transient has settled in less than 2 ms.

Controller Implementation in the Nonlinear System

The feedback gains found earlier are designed using a linear system with constant coefficients. The variables which are involved with the linear system are error or perturbation variables. Hence, the state error is multiplied by the gain matrix and the perturbation control is computed. In order to implement this type of controller in an actual engine or in this case in the nonlinear engine model simulation, it is necessary to convert actual variables into error or perturbed variables, apply the controller, then convert the perturbed control commands to actual control commands.

The feedback gains are implemented as in Figure 6. From the nonlinear system, the state variables $x(t)$ are found. The reference or steady state values, $x_n(t)$, are then subtracted from the current values to give the perturbed values $\Delta x(t)$.

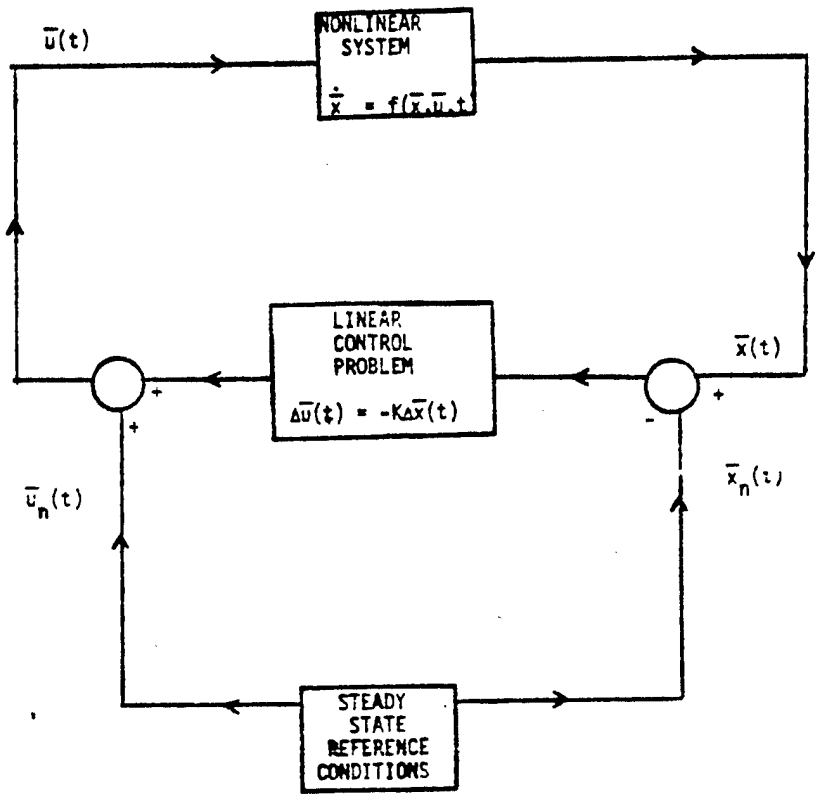

FIGURE 6 -- FLOW CHART SHOWING LQR CONTROLLER IMPLEMENTATION

The control law is then used to generate the perturbed control variables $\Delta u(t)$. This value is then added to the reference control values, $u_n(t)$, to give the actual control variable $u(t)$ which is then limited to set actuator limits of 100%. The feedback matrix, K, is the LQR feedback matrix described earlier.

CONCLUSIONS AND RECOMMENDATIONS FOR FURTHER STUDY

The following conclusions can be drawn regarding the feasibility of implementation of an LQR tracking control on the SSME.

1. The feasibility study was conducted with the assumption of perfect state knowledge. Measurements of some variables may not be available. It is possible, however, to measure enough parameters so that the system will be completely observable and hence a Kalman Filter or stochastic observer can be used to estimate system parameters.

2. Linear models need to be designed at different operating points before any conclusions can be made as to the control of preburner temperature, mixture ratio and thrust for different engine operating conditions.

3. A linear model should be developed which includes both the oxidizer and fuel preburners as well as the main combustion chamber dynamics. A model of this sort will include the oxidizer flow dynamics which from this study affect preburner temperature significantly.

This study has shown that preburner temperature control can be accomplished using a simplified model of the preburner and the Linear Quadratic Regulator theory assuming full-state availability for a typical main combustion pressure change. Further research in this control problem can be divided into the following areas.

1. Low-order linear model derivation that well represents the system dynamics at various operating points. This model should include dynamics relevant to temperature control including the fuel and oxidizer preburners and turbines as well as the thrust chamber dynamics. These models can be derived through perturbation studies of a nonlinear simulation model or by some piecewise elements of the system and control matrices by computer differentiation of the nonlinear equation evaluated at various operating conditions. Most models generated by these methods are too large

and do not contain the most convenient parameterization of the dynamics. Various methods can be used to derive this linear model the most attractive of which involves modal decomposition which simply performs an eigenanalysis of the full-state linearized digital SSME dynamic model. From eigenvalue and eigenvector studies, the matrix of eigenvalues should yield partitioned submatrices that will consist of high, middle, and low frequency dynamics. The high frequency dynamics are assumed to be equilibrated ($\Delta \dot{x}=0$) and hence reduce the model order. Some middle frequencies can probably be eliminated from further study. It must be remembered, however, that the partitioning of the system is dependent on the control designer's estimate of the frequency range of the control function. For example, the frequency bandwidth for thrust modulation will be significantly different than that for turbine inlet temperature dynamics. Actuator dynamics should also be included and realistic time delays built in to the simulation models for control activity.

2. The set of low-order linearized models are then used to design LQ-regulators.

3. A sensitivity study of the system should then be performed to yield information concerning transient changes due to varying system parameters such as thrust for example. A sensitivity study should also yield clues to the type of gain scheduling technique to be implemented.

4. A study should be performed that will develop a set of Kalman-Bucy filter gains (state estimator) assuming an observable system for each linear model. Gain scheduling techniques should also be investigated.

5. The Kalman-Bucy filters and their associated LQ-regulator gains should then be tested on the linear and nonlinear models for controller effectiveness over the flight envelope.

6. A feasibility study using performance results from above should then be performed to determine any hardware incompatibilities ignored in the above steps. If the control designer has done his job correctly, a test program should be investigated to test the controller on a real engine.

This sequence is not meant to be all inclusive. Any changes in this sequence will be a function of experience as the control study progresses. This sequence if followed should yield an excellent multivariable control law for the SSME that will significantly increase engine performance.

ACKNOWLEGEMENTS

The author wishes to express his thanks to S. Brandt for her patience and excellent typing ability. This paper could not have been completed without her. The author would also like to thank R. Brewster, R. Searle, E. Bekir, C. Landis and L. Sack for their technical assistance in modeling and applying the LQR methodology to a very difficult problem.

BIBLIOGRAPHY

1. Athans, M., "The Role and Use of the Stochastic Linear -Quadratic-Gaussian Problem in Control System Design," IEEE Transactions of Automatic Control, Vol. AC-16, Number 6, Dec. 1971

2. De Hoff, R. L., Hall, W.E. Jr., "Design of a Multivariable Controller for an Advanced Turbofan Engine," 1976 IEEE Conference on Decision and Control, Clearwater Beach Florida, Dec. 1976

3. De Hoff, R. L., Hall, W.E. Jr., "Optimal Control of Turbine Engines," Journal of Dynamic Systems, Measurement, and Control, June 1979, Vol. 101

4. Taiwo, O., "Design of Multivariable Controllers for an Advanced Turbofan Engine by Zakian's Method of Inequalities," Journal of Dynamic Systems, Measurement, and Control, Dec. 1979, Vol. 101

5. Merrill, W., "An Application of Modern Control Theory to Jet Propulsion Systems," NASA Technical Memorandum, NASA TM X-71726, May 1975

6. Michael, G. and Farrar, F. (1973) "Development of Optimal Control Modes for Advanced Technology Propulsion Systems," United Aircraft Research Laboratories (UARL) Report No. M9-11620-1

7. Nguyen, D. G., "Engine Balance and Dynamic Model," Rockwell International Corporation, Rocketdyne Division, RL00001, Rev. Ltr. G

8. Brogan, W. L., Modern Control Theory, Quantum Publishers, New York, 1974.

9. Luenberger, D. (1966) "Observers for Multivariable Systems," IEEE Transactions on Automatic Control, Vol. AC-11.

10. Junkins, J. L., Mechanics: Dynamical Systems Introduction to Optimal Estimation of Dynamic Systems, Sijthoff & Noordhoff, 1978.

11. Bryson, A. E. and Ho, Y. C.: Applied Optimal Control, Ginn and Company, Waltham, Mass. 1969.

12. Kwakernaak, H., Sivan, R., Linear Optimal Control Systems, Wiley-Interscience, 1972.

13. Evatt, T. C., "Control Alternatives for an Unmanned Free Swimming Submersible Vehicle", Master of Science Thesis, Dept. of Aerospace and Ocean Engineering, VPI & SU, August 1981.

14. Armstrong, E. S., Control and Systems Theory, Volume 10: ORACLS A Design System for Linear Multivariable Control, Marcel Dekker, Inc. 1980.

Next page intentionally left blank.

VEHICLE SUSPENSION DYNAMIC OPTIMIZATION

Edward J. Haug
Vikram N. Sohoni
Sang S. Kim
Hwal-G. Seong
Center for Computer Aided Design
The University of Iowa

Next page intentionally left blank.

VEHICLE SUSPENSION DYNAMIC OPTIMIZATION

Edward J. Haug
Vikram N. Sohoni
Sang S. Kim
Hwal-G. Seong
Center for Computer Aided Design
College of Engineering
The University of Iowa
Iowa City, Iowa 52242

ABSTRACT

A vehicle suspension dynamic response design sensitivity analysis and optimization technique is presented and illustrated. Dynamic response measures included in the formulation, for use as the objective function or as constraints, include driver absorbed power, driver peak acceleration, and suspension element travel. Design parameters available to the designer include suspension spring and damper characteristics, suspension dimensions, and parameters in feedback control suspension subsystems. An adjoint variable technique that is generally applicable to such problems is employed and formulas for derivatives of dynamic response measures with respect to design parameters are derived. Numerical results with a five degree-of-freedom vehicle model demonstrate feasibility of the method and may serve as a guide for application to more complex models.

INTRODUCTION

Vehicle mobility modelling has progressed to the point that performance of actual or concept vehicles can be analyzed using proven computer simulations. The NATO Reference Mobility Model (NRMM) [1] has been used extensively to evaluate vehicle ride quality and overall performance. It makes use of driver absorbed power [2,3] as a criteria for determining maximum acceptable sustained vehicle speed over terrain and driver acceleration as a criteria for maximum acceptable vehicle speed over an obstacle. More recently, the Dynamic Analysis and Design System (DADS) methodology has been used in detailed analysis of vehicle dynamic response to gun firing, passage over terrain and obstacles, and weapon station stabilization [4,5].

To date, the mobility modelling methods noted above have been used almost exclusively for evaluation of vehicles. Little effort has been devoted to extending these techniques as design tools. Methods of control system optimization [6] have been

developed for mechanical system optimization [7], but have not yet been brought to bear on vehicle system design optimization. The purpose of this paper is to present and illustrate a method that can be used to build upon modelling methodology to obtain a design tool.

In order to be concrete in presentation of the method, a five degree-of-freedom vehicle model that is similar to idealizations used in the NRMM is employed as an illustrative example. System equations are derived using Lagranges equations to yield second order differential equations that depend on system design parameters. These equations are then reduced to first order form, to allow easy development of design sensitivity equations. Absorbed power calculations, using a system of first order differential equations, is then reviewed as a key ingredient in design problem formulation.

A vehicle design optimization formulation is presented to minimize driver absorbed power on a nominal road, subject to bounds on absorbed power on a rough road, driver peak acceleration over a discrete obstacle, suspension jounce and rebound travel, wheel hop, and limits on design parameters. An adjoint variable method borrowed from optimal control theory [6] is then derived for calculation of design derivatives of vehicle dynamic response measures. An iterative optimization algorithm [8] is then outlined for vehicle design optimization. Its use for solution of the five degree-of-freedom example is then illustrated.

VEHICLE MODEL AND EXCITATION

The vehicle model used in this study is a five degree-of-freedom (5-DOF) plane linear model shown in Fig. 1. The generalized vehicle coordinates are the passenger seat displacement x_1, the vehicle body vertical displacement x_2 and rotation x_3, and the front and rear wheel vertical displacements x_4 and x_5. The spring stiffnesses are denoted by k_1 to k_5 and damping coefficients are c_1 to c_5. Lengths are denoted by L_1 to L_4. The functions $f_1(t)$ and $f_2(t)$ represent displacements of the front and rear wheels due to undulation in the road surface on which the vehicle is traveling.

The equations of motion for the vehicle are derived using Lagrange's equations of motion. In matrix form, they are

$$[M]\ddot{x} + [C]\dot{x} + [K]x = q(t) \qquad (1)$$

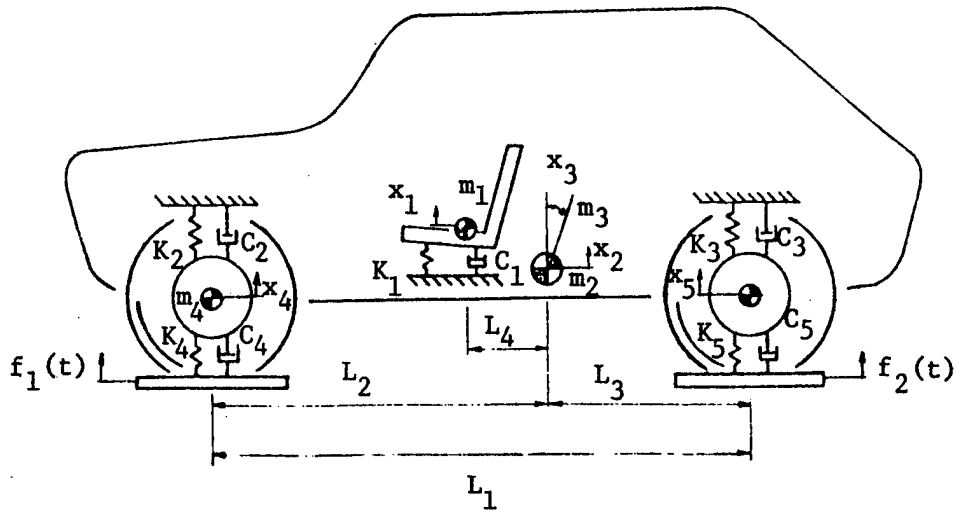

Figure 1. Five degree-of-freedom vehicle model

where

$$[M] = \begin{bmatrix} m_1 & & & & \\ & m_2 & & 0 & \\ & & m_3 & & \\ & 0 & & m_4 & \\ & & & & m_5 \end{bmatrix} \tag{2}$$

where m_3 is the pitch moment of inertia of mass m_2 and

$$[C] = \begin{bmatrix} c_1 & -c_1 & -L_4c_1 & 0 & 0 \\ & (c_1+c_2+c_3) & (L_4c_1+L_2c_2-L_3c_3) & -c_2 & -c_3 \\ & & (L_4^2c_1+L_2^2c_2+L_3^2c_3) & -L_2c_2 & L_3c_3 \\ & \text{Symmetric} & & (c_2+c_4) & 0 \\ & & & & (c_3+c_5) \end{bmatrix} \tag{3}$$

$$[K] = \begin{bmatrix} k_1 & -k_1 & -L_4k_1 & 0 & 0 \\ & (k_1+k_2+k_3) & (L_4k_1+L_2k_2-L_3k_3) & -k_2 & -k_3 \\ & & (L_4^2k_1+L_2^2k_2+L_3^2k_3) & -L_2k_2 & L_3k_3 \\ & \text{Symmetric} & & (k_2+k_4) & 0 \\ & & & & (k_3+k_5) \end{bmatrix} \quad (4)$$

$$q(t) = \begin{bmatrix} 0 \\ 0 \\ 0 \\ k_4f_1(t) + c_4\dot{f}_1(t) \\ k_5f_2(t) + c_5\dot{f}_2(t) \end{bmatrix} \quad (5)$$

If one defines

$$\left.\begin{aligned} z_i &= x_i \\ z_{5+i} &= \dot{x}_i \end{aligned}\right\} \quad i = 1,2,3,4,5 \quad (6)$$

then Eq. 1 and initial conditions can be transformed to the first-order form

$$\left.\begin{aligned} \dot{z}(t) &= f(t, z, b) \\ z(0) &= 0 \end{aligned}\right\} \quad (7)$$

where

$$z(t) = [z_1, z_2, \ldots z_{10}]^T \quad (8)$$

$$b = [b_1, b_2, \ldots b_6]^T = [k_1, k_2, k_3, c_1, c_2, c_3]^T \qquad (9)$$

and

$$f(t,z,b) = \begin{bmatrix} z_6 \\ z_7 \\ z_8 \\ z_9 \\ z_{10} \\ \frac{1}{m_1}(-b_1z_1+b_1z_2+L_4b_1z_3-b_4z_6+b_4z_7+L_4b_4z_8) \\ \frac{1}{m_2}\{b_1z_1-(b_1+b_2+b_3)z_2-(L_4b_1+L_2b_2-L_3b_3)z_3+b_2z_4+b_3z_5 \\ b_4z_6-(b_4+b_5+b_6)z_7-(L_4b_4+L_2b_5-L_3b_6)z_8+b_5z_9+b_6z_{10}\} \\ \frac{1}{m_3}\{L_4b_1z_1-(L_4b_1+L_2b_2-L_3b_3)z_2-(L_4^2b_1+L_2^2b_2+L_3^2b_3)z_3 \\ +L_2b_2z_4-L_3b_3z_5+L_4b_4z_6-(L_4b_4+L_2b_5-L_3b_6)z_7 \\ -(L_4^2b_4+L_2^2b_5+L_3^2b_6)z_8+L_2b_5z_9-L_3b_6z_{10}\} \\ \frac{1}{m_4}\{b_2z_2+L_2b_2z_3-b_2z_4-k_4(z_4-f_1(t)) \\ +b_5z_7+L_2b_6z_8-b_5z_9-c_4(z_9-\dot{f}_1(t)) \\ \frac{1}{m_5}\{b_3z_2-L_3b_3z_3-b_3z_5-k_5(z_5-f_2(t)) \\ +b_6z_7-L_3b_6z_8-b_6z_{10}-c_5(z_{10}-\dot{f}_2(t))\} \end{bmatrix} \qquad (10)$$

Numerical values of the model parameters used in this study are given in Table 1. The spring and damping coefficients given for the driver's seat and suspension will be the starting values for optimization.

Table 1. System Parameters

Index	1	2	3	4	5
Generalized masses m_i (lb or lb-in-sec^2)	290	4500	41000	96.6	96.6
Spring coeff. k_i (lb/in.)	100	300	300	1500	1500
Damping coeff. c_i (lb-sec/in.)	10	25	25	5	5
Distance, L_i (in)	120	40	80	10	-

In this vehicle model, the tires are modeled as point followers, which are always in contact with the ground. If a tensile force occurs between wheel and ground, wheel hop would actually occur. In the design formulation, a constraint precluding wheel hop is imposed.

In vehicle dynamic response analysis, the input road conditions are quite important. Dynamic response of the vehicle depends strongly on the vertical displacement history of the wheels on the road surface. Typical road conditions are defined as a sinusoidal undulation, with amplitude y_0 and variable half-wavelength ℓ_i. The front tire displacement v(y) at a location y is defined as

$$v(y) = \begin{cases} y_0\left[1 - \cos\frac{\pi(y-y^{i-1})}{\ell_i}\right], & y^{i-1} < y < y^i, \ i \text{ is odd} \\ y_0\left[1 + \cos\frac{\pi(y-y^{i-1})}{\ell_i}\right], & y^{i-1} < y < y^i, \ i \text{ is even} \end{cases}$$

where y is a coordinate measured along the road and $y^i = \sum_{j=1}^{i} \ell_j$.

If the constant speed of the vehicle is denoted by s, the elapsed time between front and rear tire encounter of the same point on the road surface is $t_\sigma = L_1/s$, where L_1 is the distance between front and rear wheels. Then,

$$v(t) = \begin{cases} y_0[1 - \cos w_i(t-t^{i-1})], & t^{i-1} < t < t^i, \ i \text{ is odd} \\ y_0[1 + \cos w_i(t-t^{i-1})], & t^{i-1} < t < t^i, \ i \text{ is even} \end{cases} \quad (11)$$

where $w_i = \pi s/\ell_i$ and $t^i = y^i/s$. The vertical displacement function for the front wheel can therefore be defined as

$$f_1(t) = \begin{cases} v(t), & 0 < t < T_1 \\ 0, & \text{otherwise} \end{cases} \quad (12)$$

where T_1 is the time at which the road undulation ceases. The vertical displacement of the rear wheel has the same value as that of the front wheel, but with a time lag. That is,

$$f_2(t) = f_1(t-t_\sigma), \quad t_\sigma < t < T_1 + t_\sigma \quad (13)$$

In this study, three different road profiles are used for determining the vertical displacement functions of the tires, as shown in Fig. 2. Profile (1) is a continuous sinusoidal curve with a constant half-wavelength of 480 in. and an amplitude of $y_0 = 2$ in. This profile represents a smooth highway condition. Profile (2) is a continuous sinusoidal curve with a constant half-wavelength of 60 in. and an amplitude of 2 in., which represents a rough highway condition. Profile (3) is a combination of two sinusoidal curves with different half-wavelengths $\ell_1 = 360$ in. and $\ell_2 = 144$ in. and an amplitude of 5 in. This profile represents a severe bump condition.

The vehicle speeds for each road profile are as follows:

960 in/sec (54.5 mile/h) for profile No. 1
616 in/sec (35.0 mile/h) for profile No. 2
450 in/sec (25.6 mile/h) for profile No. 3.

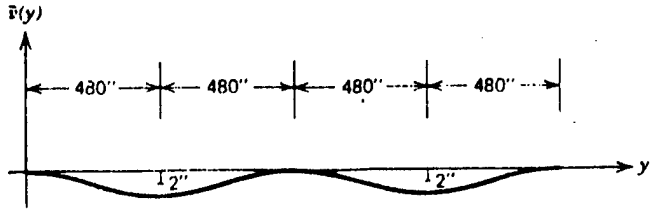

(a) profile no. 1

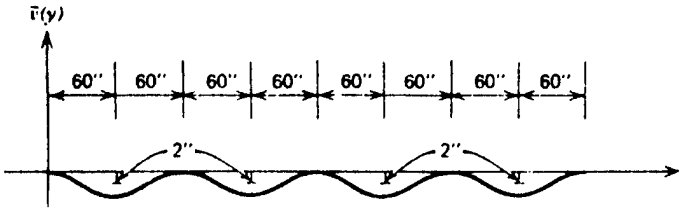

(b) profile no. 2

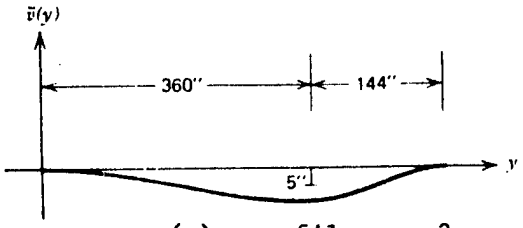

(c) profile no. 3

Figure 2. Road surface profiles

ABSORBED POWER

Absorbed power is a measure of the rate at which vibrational energy is absorbed by a human and is a quantity that may be used to determine human tolerance to vibration when a vehicle is negotiating rough terrain. The "absorbed power" concept was developed in the 1960's(2), although it has not been widely used until recent years(1). In this study, the absorbed power in the time domain is used as a measure of ride comfort.

Absorbed power equations given in the NATO Reference Mobility Model [1,2,3] are as follows:

$$\dot{p}(t) = g(p,z,b), \quad 0 < t < \tau$$
$$p(0) = 0 \qquad (14)$$

where

$$p(t) = [p_1, p_2, \ldots, p_7]^T$$

$$g = \begin{bmatrix} -29.8p_1 - 497.49\ddot{z}_1 - 100p_2 \\ 10p_1 \\ 1736.9p_1 - 108p_4 \\ 100p_1 - 35.19p_3 - 39.1p_4 \\ -315.7p_1 + 34.0956p_4 + 171.075p_6 \\ -80.0p_1 - 91.36p_4 - 30.28p_5 \\ p_1 - 0.108p_4 + 0.25p_6 - 6p_7 \end{bmatrix} \qquad (15)$$

Here, $\ddot{z}_1$ is the vertical acceleration of the driver's seat of the vehicle, in units of g's. Thus, from Eq. 10,

$$\ddot{z}_1 = -\frac{1}{m_1 g}\{b_1(z_1-z_2-L_4z_3) + b_4(z_6-z_7-L_4z_8)\} \qquad (16)$$

where g is the gravitational acceleration.

The average absorbed power AP is defined, in units of Watts, as

$$AP \equiv \frac{1}{\tau}\int_0^{\tau} \{p_1(t)-0.108p_4(t)+0.25p_6(t)-p_7(t)\}^2 dt \qquad (17)$$

Using the solution of Eq. 14, absorbed power can be calculated numerically.

THE OPTIMAL DESIGN PROBLEM

With equations of motion, absorbed power equations, and terrain displacement functions defined for the wheels, one can now define the optimal design problem. It is desired to make the driver as comfortable as possible, over a range of road conditions and traveling speeds. Thus, the design objective is to minimize the absorbed power of the driver on the smooth highway condition, by adjusting suspension parameters of the vehicle, subject bounds on the following:

i) absorbed power and wheel hop at the rear wheel on the rough highway condition,

ii) maximum vertical acceleration of the driver's seat, wheel hop at the rear wheel, and the rattle space between seat

and body, body and wheels, and wheels and ground on the bump road condition,

iii) design variables.

The optimal design problem may be written as follows:

$$\text{Minimize } \psi_0 = \int_0^\tau G(p^1(t))dt \tag{18}$$

where

$$G(p) = \{p_1(t)-0.108p_4(t)+0.25p_6(t)-p_7(t)\}^2/\tau \tag{19}$$

subject to the state equation of Eq. 7, the absorbed power equation of Eq. 14, and the constraints

$$\psi_1 = \int_0^\tau G(p^2(t))dt - \theta_1 \leq 0 \tag{20}$$

$$\psi_2 = z_5^2-f_2(t) - \theta_2 \leq 0,\ 0 \leq t \leq \tau \tag{21}$$

$$\psi_3 = -(z_5^2-f_2(t)) - \theta_3 \leq 0,\ 0 \leq t \leq \tau \tag{22}$$

$$\psi_4 = \left|\frac{1}{m_1}\{b_1(z_2^3+L_4z_3^3-z_1)+b_4(z_7^3+L_4z_8^3-z_6^3)\}\right| - \theta_4 \leq 0,\ 0\leq t\leq\tau, \tag{23}$$

$$\psi_5 = |z_2^3+L_4z_3^3-z_1^3| - \theta_5 \leq 0,\quad 0 \leq t \leq \tau, \tag{24}$$

$$\psi_6 = |z_4^3-z_2^3-L_2z_3^3| - \theta_6 \leq 0,\quad 0 \leq t \leq \tau, \tag{25}$$

$$\psi_7 = |z_5^3-z_2^3-L_3z_3^3| - \theta_7 \leq 0,\quad 0 \leq t \leq \tau, \tag{26}$$

$$\psi_8 = |z_4^3-f_1(t)| - \theta_8 \leq 0\ ,\quad 0 \leq t \leq \tau, \tag{27}$$

$$\psi_9 = z_5^3 - f_2(t) - \theta_9 \leq 0,\ 0 \leq t \leq \tau \tag{28}$$

$$\psi_{10} = -(z_5^3-f_2(t)) - \theta_{10} \leq 0,\ 0 \leq t \leq \tau \tag{29}$$

where θ_i, $i = 1,2,\ldots,10$ are constraint bounds and z^j and p^j are state and power solutions and j is the road profile number, defined as j=1 for the smooth highway, j=2 for the rough highway, and j=3 for the bump, and the constraints of design bounds

$$b_i^L \leq b_i \leq b_i^U, \quad i=1,2,3,4,5,6 \tag{30}$$

where

θ_1 = maximum allowable absorbed power.

θ_2, θ_9 = maximum allowable upward distance between rear wheel and road surface. Since the tire should be always in contact with the road, this value may be static deflection of rear tire, neglecting dynamic effect of tire.

θ_3, θ_{10} = maximum allowable downward distance between rear wheel and road surface.

θ_4 = maximum allowable acceleration at driver's seat.

θ_5 = maximum allowable distance between driver's seat and chassis.

θ_6, θ_7 = maximum allowable distance between body, and front wheel and rear wheel, respectively.

θ_8 = maximum allowable distance between front wheel and road.

The values of θ_i and design bounds for this study are given in Tables 2 and 3.

Table 2. θ_i Values

θ_1	3.5 watts
θ_2	1.1127 in
θ_3	3.0 in
θ_4	350 in/sec^2
θ_5	2.0 in
θ_6	5.5 in
θ_7	5.5 in
θ_8	2.0 in
θ_9	1.1127 in
θ_{10}	3.0 in

Table 3. Design Bounds

i	b_i^L	b_i^U
1	25lb/in	500lb/in
2	100lb/in	10001b/in
3	100lb/in	10001b/in
4	1.01b-sec/in	501b-sec/in
5	2.51b-sec/in	801b-sec/in
6	2.51b-sec/in	801b-sec/in

DESIGN SENSITIVITY ANALYSIS

Dynamic systems treated here are described by a design variable vector $b = [b_1, b_2, \ldots b_6]^T$ and two state variable vectors, $z(t) = [z_1(t), z_2(t), \ldots z_{10}(t)]^T$ and $p(t) = [p_1(t), p_2(t), \ldots p_7(t)]^T$, which are the solutions of initial value problem of Eqs. 7 and 14, rewritten here as

$$\dot{z}(t) = f(t,z,b), \quad 0 < t < \tau$$
$$z(0) = 0 \tag{31}$$

$$\dot{p}(t) = g(p,z,b), \quad 0 < t < \tau$$
$$p(0) = 0 \tag{32}$$

The design problem may be written in terms of functionals of the form

$$\psi_i = \int_0^\tau G(p^i(t))dt - \theta_i, \quad i=0,1 \tag{33}$$

where $\theta_0 = 0$ and

$$\psi_i = h_i(t_i,z,b) - \theta_i, \quad i=2,3,\ldots 10 \tag{34}$$

where t_i is determined by conditions

$$\Omega_i(t_i,z,b) = \frac{d}{dt} h_i(t,z,b)\Big|_{t=t_i} = 0, \quad i=2,3,\ldots 10 \tag{35}$$

The dependence on design variable b in Eq. 33 arises through the absorbed power state variable $p = p(t; b)$. In Eq. 34, it arises both explicitly and through the displacement state variable $z = z(t; b)$. In order to obtain the derivatives of ψ_i with respect to b, an adjoint variable technique [6,7] may be introduced. For the i=0 and 1,

$$\frac{d\psi_i}{db} = \int_0^\tau G_p \, p_b^i \, dt, \quad i=0,1 \tag{36}$$

where subscript denotes differentiation. One may introduce an adjoint variable γ to obtain the identity

$$\int_0^\tau \gamma^T[\dot{p}-g]dt = 0 \tag{37}$$

Taking the derivative of Eq. 37 with respect to b, one has

$$-\int_0^\tau \gamma^T[\dot{p}_b-g_p p_b-g_z z_b-g_b]dt = 0$$

Integrating the first term by parts gives

$$\int_0^\tau [\dot{\gamma}^T+\gamma^T g_p]p_b + \gamma^T g_z z_b + \gamma^T g_b \; dt$$

$$- \gamma^T(\tau)p_b(\tau) = 0 \tag{38}$$

since $p_b(0) = 0$ from Eq. 32.

Since Eq. 38 holds for any function γ, a function γ can be chosen to satisfy the following differential equation and terminal condition:

$$\dot{\gamma}^i + g_p^T\gamma^i = G_p, \quad 0 \leq t \leq \tau$$

$$\gamma^i(\tau) = 0 \quad , \quad i=1,2 \tag{39}$$

Equation 36 may thus be written, using Eq. 38, as

$$\frac{d\psi_i}{db} = \int_0^\tau (-\gamma^{i^T} g_b - \gamma^{i^T} g_z z_b^i)dt, \quad i=0,1 \tag{40}$$

Another adjoint variable λ is introduced through the identity

$$\int_0^\tau \lambda^T[\dot{z}-f]dt = 0 \tag{41}$$

Taking the derivative of Eq. 41 and integrating by parts gives

$$\int_0^\tau [\dot{\lambda}^T+\lambda^T f_z]z_b + \lambda^T f_b \; dt - \lambda^T(\tau)z_b(\tau) = 0 \qquad (42)$$

since $z_b(0) = 0$. By the same reasoning as above, the additional adjoint equation is obtained as

$$\dot{\lambda}^i + f_z^T\lambda^i = -g_z^T\gamma^i, \quad 0 < t < \tau \quad , \quad i=1,2 \qquad (43)$$

$$\lambda^i(\tau) = 0$$

Thus, Eq. 40 becomes

$$\frac{d\psi_i}{db} = -\int_0^\tau (\gamma^{i^T} g_b+\lambda^{i^T} f_b)dt, \quad i=0,1 \qquad (44)$$

For the second kind of functional, Eq. 34 gives

$$\frac{d\psi_i}{db} = h_{i_z}[z_b(t_i)+\dot{z}(t_i)(t_i)_b]+h_{i_b}+h_{i_t}t_b \quad i=2,3,\ldots 10 \qquad (45)$$

Differentiating Eq. 35 with respect to b, one obtains

$$[\Omega_{i_{t_i}}+\Omega_{i_z}\dot{z}(t_i)](t_i)_b + \Omega_{i_z}z_b(t_i) + \Omega_{i_b} = 0 \qquad (46)$$

Since Eq. 35 is to determine t_i, the coefficient of $(t_i)_b$ cannot be zero and one has

$$(t_i)_b = -\frac{\Omega_{i_z}}{\Omega_{i_{t_i}}+\Omega_{i_z}f(t_i)} z_b(t_i) - \frac{\Omega_{i_b}}{\Omega_{i_{t_i}}+\Omega_{i_z}f(t_i)} \qquad (47)$$

Substituting Eq. 47 into Eq. 45, one has

$$\frac{d\psi_i}{db} = \{h_{i_z}+\beta_i\Omega_{i_z}\}z_b(t_i) + \beta_i\Omega_{i_b} + h_{i_b}, \quad i=2,3,\ldots 10 \qquad (48)$$

where

$$\beta_i = - \frac{h_{i_z} f(t_i) + h_{i_t}}{\Omega_{i_{t_i}} + \Omega_{i_z} f(t_i)} \quad , \quad i=2,3,\ldots,10 \tag{49}$$

Using Eq. 42, one has the following adjoint problem

$$\left.\begin{aligned} &\dot{\lambda}^i + f_z^T \lambda^i = 0, \quad 0 < t < t_i \\ &\lambda^i(t_i) = -h_{i_z}^T - \beta_i \Omega_{i_z}^T \equiv H_i(t_i, z, b) \end{aligned}\right\} \quad i=2,3,\ldots 10 \tag{50}$$

Then, from Eq. 44, one has

$$\frac{d\psi_i}{db} = h_{i_b} + \beta_i \Omega_{i_b} - \int_0^{t_i} \lambda^{i^T} f_b dt \tag{51}$$

Computation of design sensitivities for a given design is thus summarized as follows:

For ψ_i, i=0,1 (absorbed power functional):

1. Integrate state equations of Eqs. 7 and 14 from t=0 to τ, where τ is the time when dynamic response of the vehicle is in the steady state.
2. Integrate adjoint equations Eqs. 39 and 43 backward from τ to 0, using known state variables.
3. Calculate design derivatives of Eq. 44.

For ψ_i, i=2,3,4,...10:

1. Integrate state equation of Eq. 7 from t=0 to some large time for given road condition to include maximum h_i.
2. Find t_i satisfying Eq. 35 by using a root finding algorithm.
3. Integrate the adjoint equation of Eq. 50 backward from $t=t_i$ to 0.
4. Calculate design derivatives of Eq. 51.

The cost and constraint values and their design derivatives for an initial design $b = [100, 200, 230, 2.8, 70, 22]^T$ are calculated. In that design, only ψ_1 and ψ_5 are violated.

The state and absorbed power, and the corresponding adjoint equations are integrated by using a Runge-Kutta-Fiehlberg method of order 4 and 5, with a relative error of 10^{-9} and absolute error of 10^{-6}. The error tolerance of Ω_i to find t_2 is given 10^{-9}.

To check the validity of design derivatives, design variations are created by making a change of 5% in each design variable. Results for ψ_0, ψ_1, and ψ_5 are given in Tables 4, 5, and 6. The predicted variations calculated by using design derivatives derived here show very good correspondence with the actual variation, within 9% difference.

With design variation $\delta b = 0.05[b_1, b_2, \ldots b_6]^T$ and multiples $b^i = b^0 + i\delta b$, i=1,2,3,4, i.e., from 5% to 20% design variation, the actual and predicted values of cost and constraints are given in Figs. 3 to 13, where the solid line is actual value and the dotted line is the predicted value. The predicted values show good correspondence with actual values.

ITERATIVE OPTIMIZATION ALGORITHM

Many mathematical programming algorithms for solving optimization problems have been developed and evaluated for engineering design optimization. In selecting an algorithm to be used, one may base his choice on accuracy of the result, rate of convergence, time required for computing, computer storage required, and compatibility with engineering analysis methods. It is not possible, however, to order all algorithms in one and only one way to say which is best. An algorithm may be poor as applied to a certain class of problems, but effective in another class. Hence it may be necessary to have a reserve of algorithms and to choose one, depending on the class of problems at hand. In this paper, the linearization method of Pshenichny [8] for optimal design of mechanical systems is used. This algorithm was originally presented in the Russian literature, but has apparently only recently come to the attention of workers in the west. Pshenichny has proved convergence of the algorithm, using an active-set strategy that is essential in large scale mechanical optimization problems.

The general mathematical programming problem is to find $b \in R^n$ to minimize $f_0(b)$, with constraints

$$\begin{aligned} f_i(b) &< 0, \qquad i=1,2,\ldots,m' \\ f_i(b) &= 0, \qquad i=m'+1,\ldots,m \end{aligned} \tag{52}$$

where $f_i(b)$, i=0,1,...,m, are continuously differentiable functions. Note that $f_i(b) = 0$ is equivalent to the inequalities $f_i(b) < 0$, and $-f_i(b) < 0$. Hence, one can limit considerations to the case with inequality constraints. Thus, one wishes to minimize $f_0(b)$, subject to the constraints

$$f_i(b) < 0, \quad i=1,2,\ldots,m \tag{53}$$

Table 4. Variation of cost (ψ_0) with 5% change of each design variable

Design Variable Changed	Current Cost	Actual Change	Predicted Change	Percentage* Sensitivity
b_1	6.568191E-01	-2.013850E-02	-2.070104E-02	102.79
b_2	6.920365E-01	1.507890E-02	1.487186E-02	98.63
b_3	6.935858E-01	1.662815E-02	1.686925E-02	101.45
b_4	6.708257E-01	-6.131887E-03	-6.188627E-03	100.93
b_5	6.779610E-01	1.003385E-03	1.089884E-03	108.62
b_6	6.745058E-01	-2.451777E-03	-2.576824E-03	105.10

*percentage sensitivity is defined as $\frac{\text{Estimated change}}{\text{True change}} \times 100$

Table 5. Variation of absorbed power constraint (ψ_1) with 5% change of each design variable

Design Variable Changed	Current Constraint Value	Actual Change	Predicted Change	Percentage Sensitivity
b_1	9.389435E-01	2.795217E-01	2.734298E-01	97.82
b_2	6.628705E-01	3.448725E-03	3.209578E-03	93.07
b_3	6.558615E-01	-3.560305E-03	-3.849868E-03	108.13
b_4	7.461878E-01	8.676600E-02	8.307421E-02	95.75
b_5	8.069681E-01	1.475463E-01	1.490884E-01	101.05
b_6	7.095821E-01	5.016029E-02	4.964487E-02	98.97

Table 6. Variation of rattle space constraint between driver's seat and chassis (ψ_5) with 5% change of each design variable

Design Variable Changed	Current Constraint	Actual Change	Predicted Change	Percentage Sensitivity
b_1	1.403466E-01	-7.959181E-02	-8.304382E-02	104.34
b_2	2.304623E-01	1.052389E-02	1.075973E-02	102.24
b_3	2.265486E-01	6.610185E-03	6.895010E-03	104.31
b_4	2.059015E-01	-1.403692E-02	-1.416363E-02	100.90
b_5	2.309891E-01	1.105070E-02	1.098409E-02	99.40
b_6	2.150365E-01	-4.901916E-03	-4.976799E-03	101.53

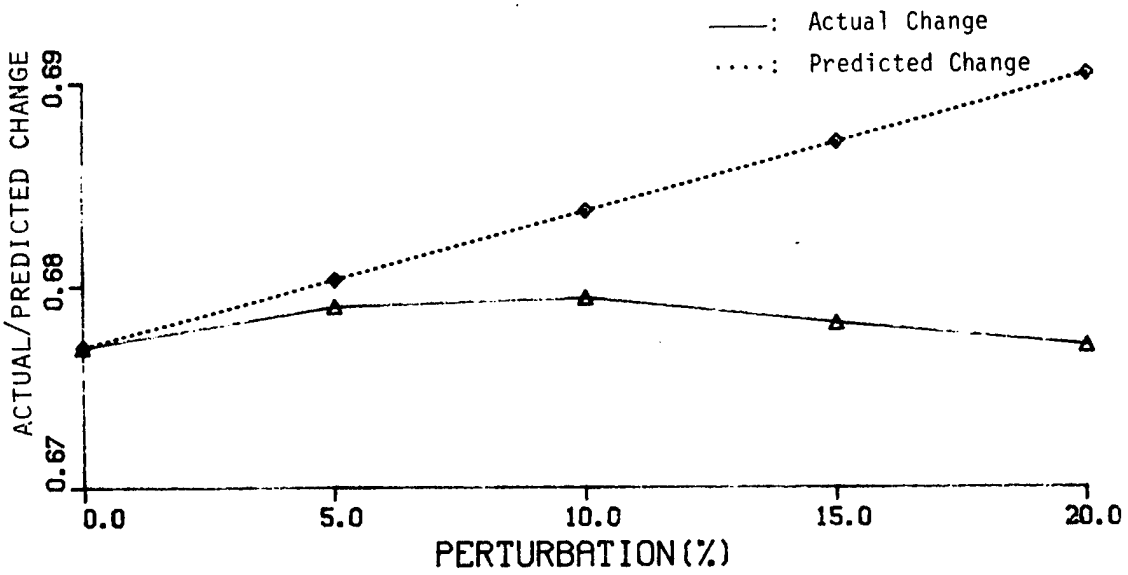

Figure 3. Accuracy test of design sensitivity of cost (ψ_0)

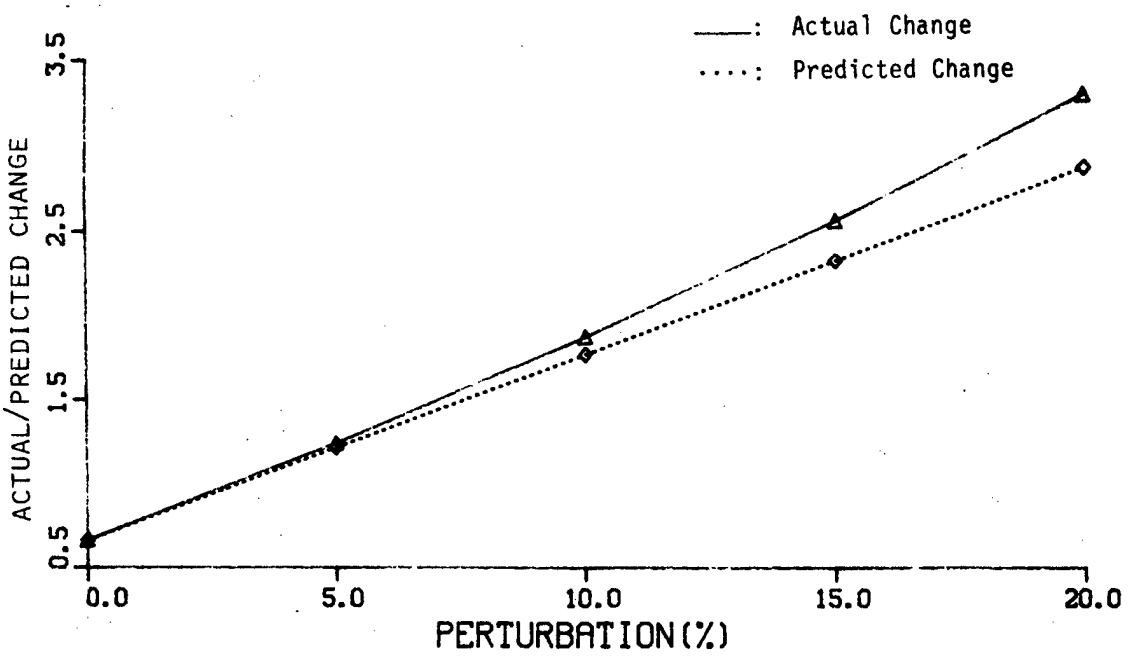

Figure 4. Accuracy test of design sensitivity of absorbed power constraint on rough highway (ψ_1)

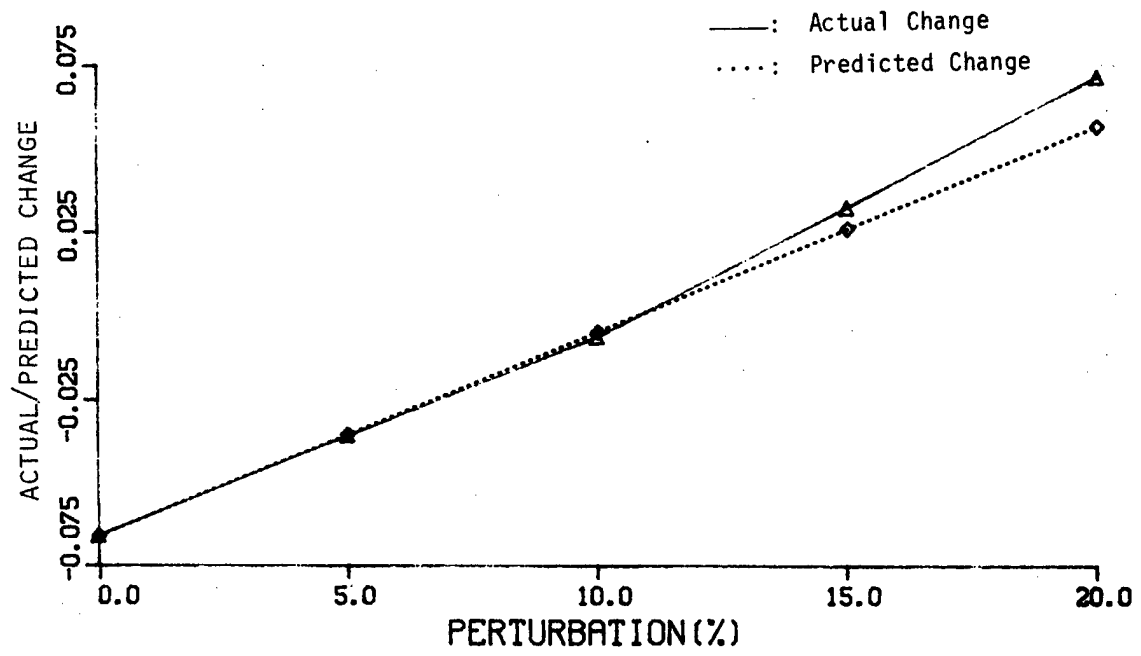

Figure 5. Accuracy test of design sensitivity of rear wheel hop constraint on rough highway (ψ_2)

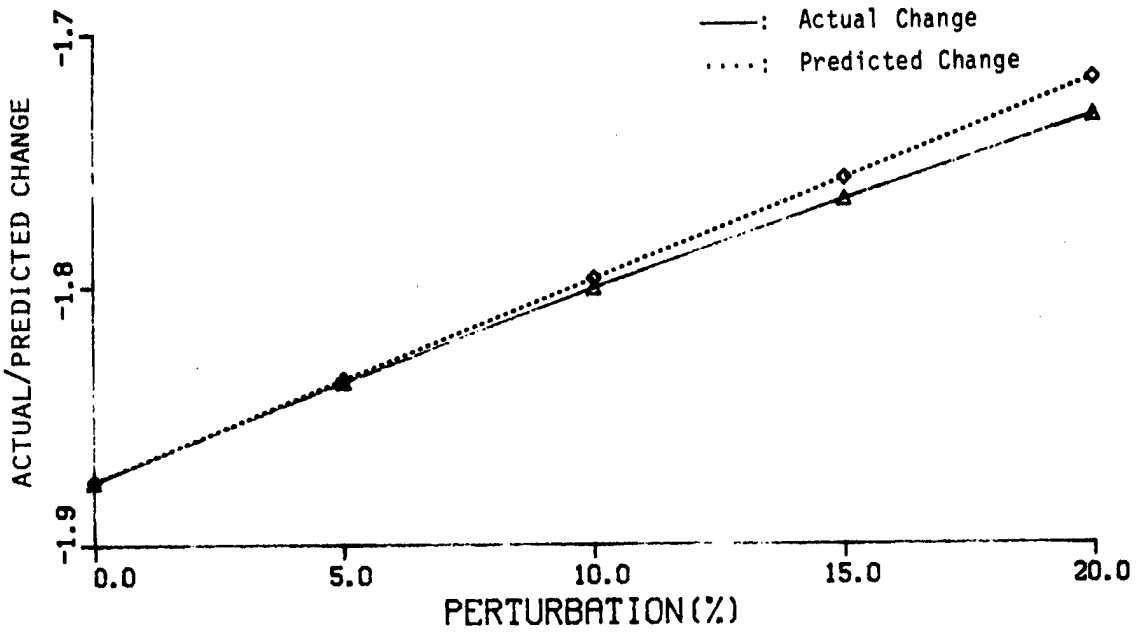

Figure 6. Accuracy test of design sensitivity of rear wheel penetration constraint on rough highway (ψ_3)

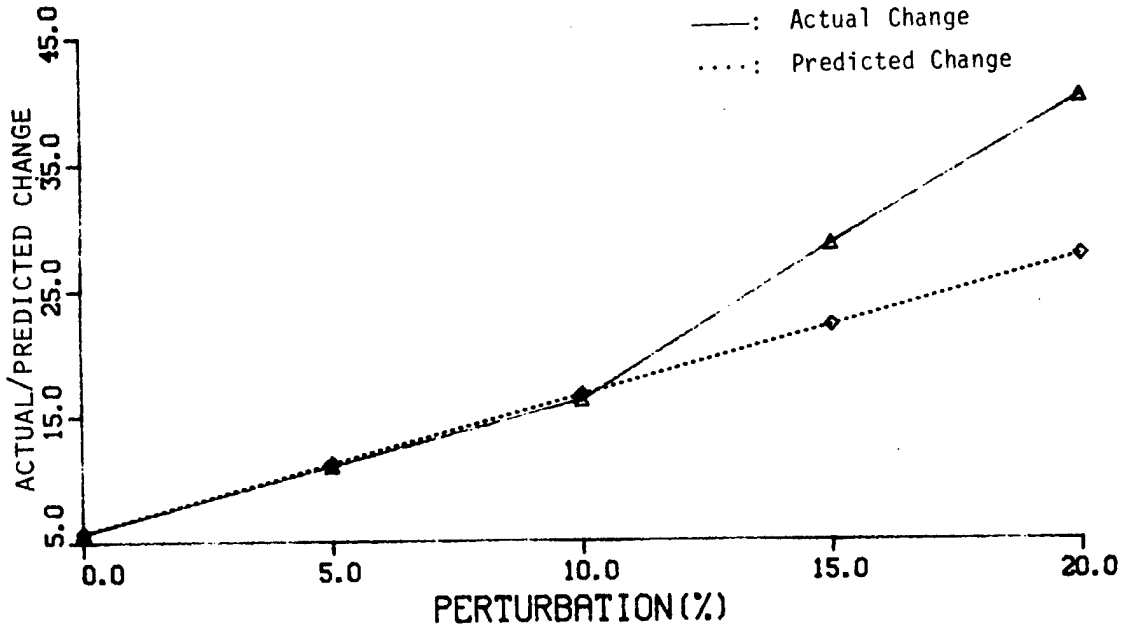

Figure 7. Accuracy test of design sensitivity of peak acceleration constraint on bump road (ψ_4)

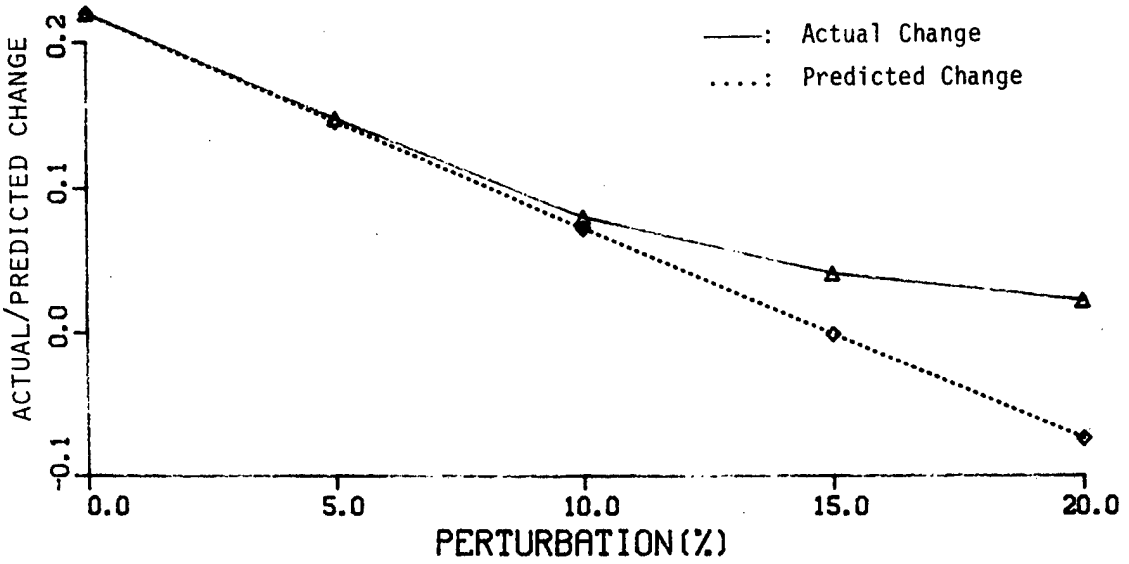

Figure 8. Accuracy test of design sensitivity of rattle space constraint between driver's seat and chassis (ψ_5)

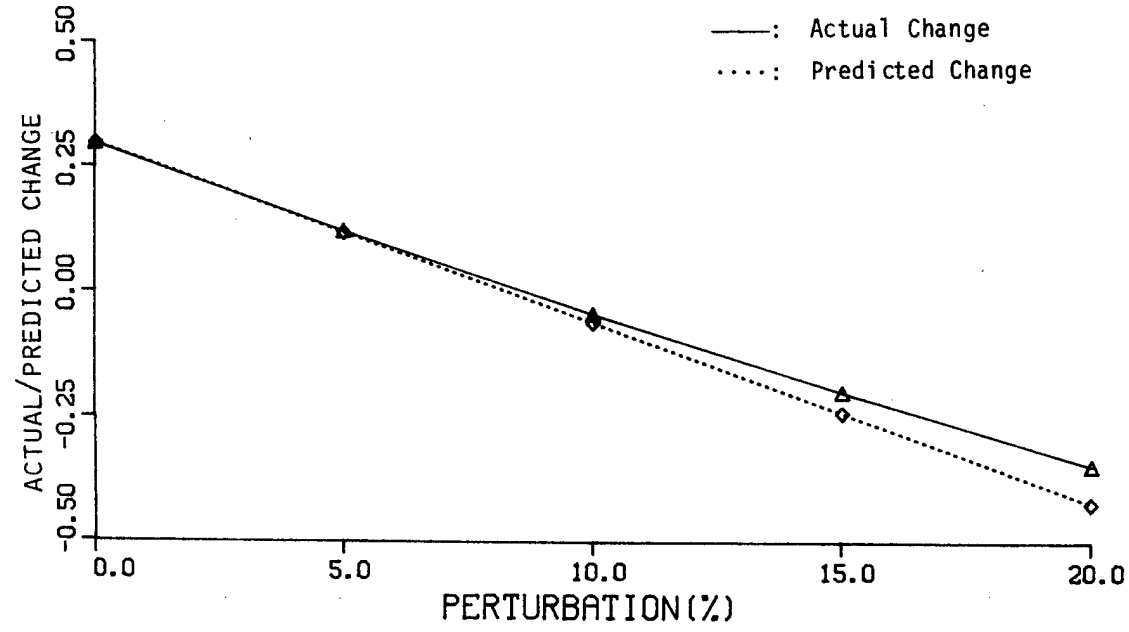

Figure 9. Accuracy test of design sensitivity of rattle space constraint between chassis and front wheel assembly (ψ_6)

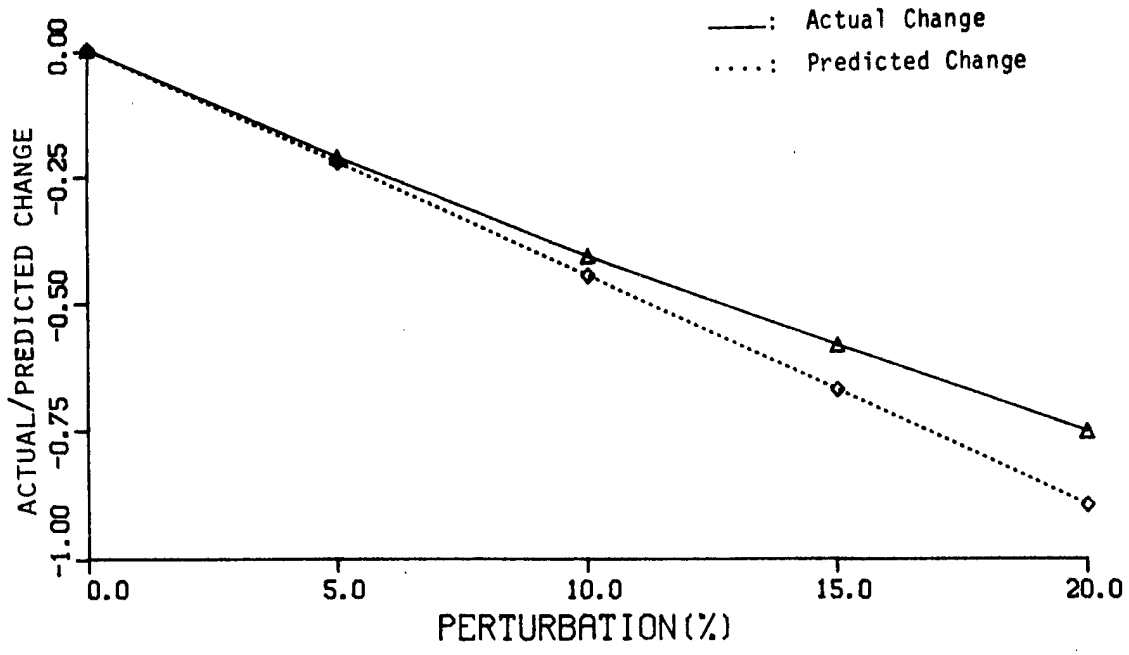

Figure 10. Accuracy test of design sensitivity of rattle space constraint between chassis and rear wheel assembly (ψ_7)

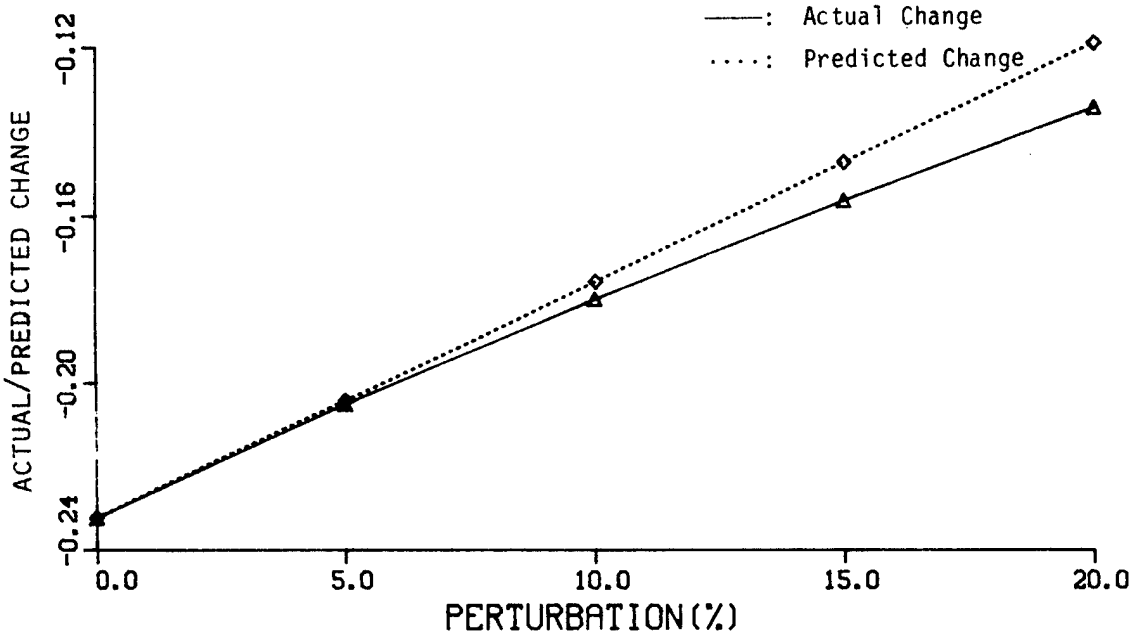

Figure 11. Accuracy test of design sensitivity of rattle space constraint between front wheel assembly and road (ψ_8)

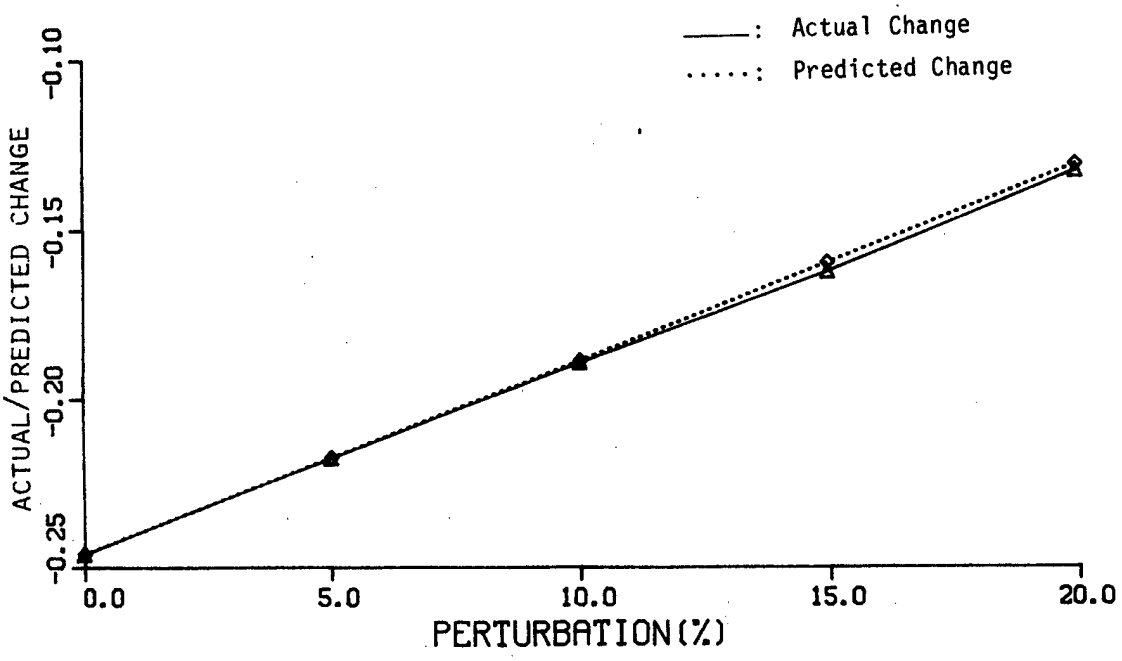

Figure 12. Accuracy test of design sensitivity of rear wheel hop constraint on bump road (ψ_9)

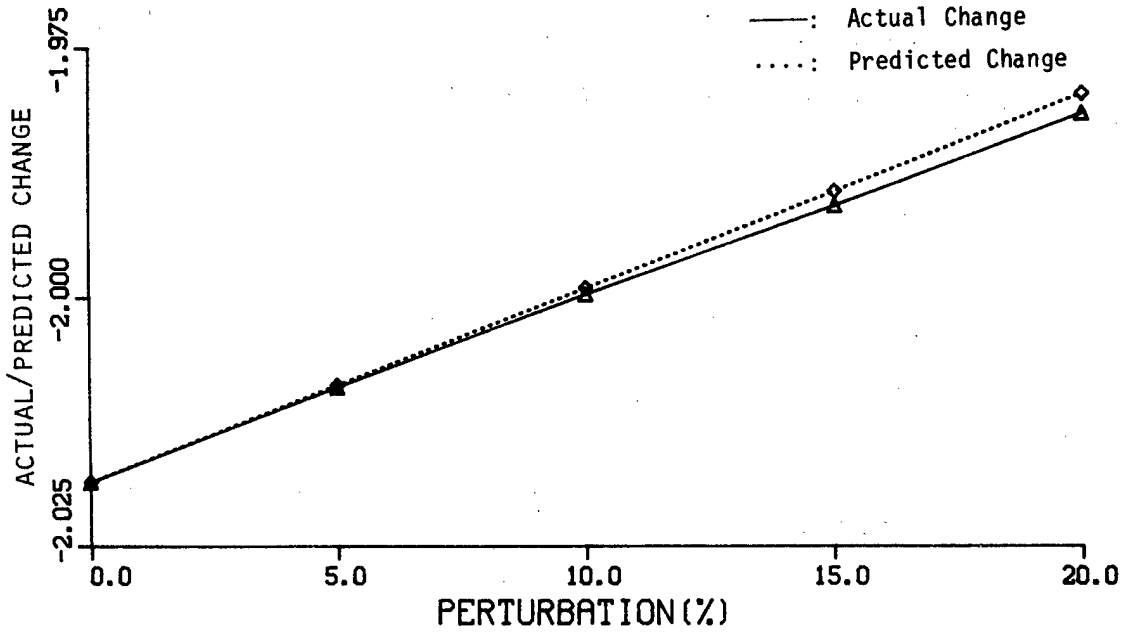

Figure 13. Accuracy test of design sensitivity of rear wheel penetration constraint on bump road (ψ_{10})

BASIC ASSUMPTIONS: Let

$$F(b) = \max \{0, f_1(b), \ldots, f_m(b)\} \tag{54}$$

Note that $F(b) \geq 0$ for all $b \in R^n$. Given $\varepsilon > 0$, define the ε-active constraint set

$$A(b,\varepsilon) = \{i: f_i(b) \geq F(b) - \varepsilon,\ i=1,2,\ldots,m\} \tag{55}$$

(a) Suppose there is an integer $N > 0$ such that the set

$$\Omega_N = \{b: \Phi_N(b) \leq \Phi_N(b^0)\} \tag{56}$$

is bounded, where b^0 is an initial design and $\Phi_N(b) = f_0(b) + NF(b)$.

(b) Suppose gradients of the functions $f_i(b)$, $i=0,1,2,\ldots,m$, satisfy Lipschitz conditions in Ω_N; i.e., there exists $L > 0$ such that

$$||f_i'(b^1) - f_i'(b^2)|| \leq L||b^1 - b^2|| \tag{57}$$

where $f_i' = [\partial f_i/\partial b_1, \ldots, \partial f_i/\partial b_n]^T$. This condition is satisfied if f_i has piecewise continuous first derivatives.

(c) Suppose the problem of quadratic programming; find $p \in R^n$ to minimize

$$(f_0'(b), p) + \frac{1}{2}||p||^2 \tag{58}$$

subject to the linearized constraints

$$(f_i'(b), p) + f_i(b) \leq 0, \quad i \in A(b,\varepsilon) \tag{59}$$

is solvable with any $b \in \Omega_N$ and there are Lagrange multipliers $u_i(b)$, $i \in A(b,\varepsilon)$, such that

$$\sum_{i \in A(b,\varepsilon)} u_i(b) \leq N \tag{60}$$

THEORETICAL ALGORITHM: Under the above hypotheses, one may state the following theoretical Linearization Algorithm of Pshenichny [8]:

Let b^0 be an initial approximation and $0 < \delta < 1$. For the kth iteration,

(1) Solve the quadratic programming problem of Eqs. 58 and 59, with $b = b^k$ and solution $p^k = p(b^k)$.

(2) Find the smallest integer i such that

$$\Phi(b^k + \frac{1}{2^i} p^k) \leq \Phi(b^k) - \frac{1}{2^i} \delta ||p^k||^2 \qquad (61)$$

If this inequality is satisfied with $i = i_0$, let $\alpha_k = 2^{-i_0}$

$$b^{k+1} = b^k + \alpha_k p^k.$$

Under the basic assumptions, Pshenichny [8] has proved convergence criteria for the algorithm.

NUMERICAL ALGORITHM: The following numerical algorithm is intended for solving the problem of minimizing $f_0(b)$, subject to the constraints of Eq. 52:

Define

$$F(b) = \max\{0, f_1(b), \ldots, f_{m'}(b), |f_{m'+1}(b)|, \ldots, |f_m(b)|\}$$
$$A(b,\varepsilon) = \{i: f_i(b) > F(b) - \varepsilon,\ i = 1,2,\ldots,m'\}$$
$$B(b,\varepsilon) = \{i: |f_i(b)| > F(b) - \varepsilon,\ i = m'+1,\ldots,m\}$$
$$\Phi_N(b) = f_0(b) + NF(b)$$

Select the initial approximation b^0, N_0 sufficiently large, $\varepsilon_0 > 0$, and $0 < \delta < 1$.

Step 1. In the kth iteration, solve the problem of finding u to minimize

$$\Phi(u) = \frac{1}{2} ||f_0'(b^k) + \sum_{i \in A(b^k,\varepsilon) \cup B(b^k,\varepsilon)} u_i f_i'(b^k)||^2 - \sum_{i \in A(b^k,\varepsilon) \cup B(b^k,\varepsilon)} u_i f_i(b^k)$$

subject to $u_i \geq 0$, $i \in A(b^k,\varepsilon)$, and u_i arbitrary for $i \in B(b^k,\varepsilon)$, where $f_i' = [\frac{\partial f_i}{\partial b_1}, \ldots, \frac{\partial f_i}{\partial b_n}]^T$.

If the solution u^k is such that $\phi(u^k) = -\infty$, then set $b^{k+1} = b^k$, $\varepsilon_{k+1} = (1/2)\varepsilon_k$, and $N_{k+1} = N_k$ and return to Step 1. Otherwise, let

$$p^k = -f_0'(b^k) - \sum_{i \in A(b^k,\varepsilon) \cup B(b^k,\varepsilon)} u_i^k f_i'(b^k) \qquad (62)$$

and go to Step 2.

Step 2. Set

$$b^{k+1} = b^k + \alpha_k p^k$$

$$\varepsilon_{k+1} = \varepsilon_k$$

where α_k is chosen equal to $\frac{1}{2^{q_0}}$ and q_0 is the smallest integer for which

$$\Phi_{N_k}\left(b^k + \frac{1}{2^q} p^k\right) < \Phi_{N_k}(b^k) - \frac{1}{2^q} \delta \, ||p^k||^2$$

Step 3. If

$$2\left(\sum_{i \in A(b^k,\varepsilon)} u_i^k + \sum_{i \in B(b^k,\varepsilon)} |u_i^k|\right) > N_k > \sum_{i \in A(b^k,\varepsilon)} u_i^k + \sum_{i \in B(b^k,\varepsilon)} |u_i^k|$$

Then let $N_{k+1} = N_k$. Otherwise, let

$$N_{k+1} = 2\left(\sum_{i \in A(b^k,\varepsilon)} u_i^k + \sum_{i \in B(b^k,\varepsilon)} |u_i^k|\right)$$

Step 4. If $||p^k||$ is sufficiently small, terminate. Otherwise, return to Step 1.

In implementing the algorithm, the derivatives f_i' are calculated using the adjoint variable method, which requires that the state and adjoint equations be solved forward and backward in time, respectively. This is a substantial amount of computation that must be carried out during each optimization iteration.

NUMERICAL RESULTS

Optimization of the vehicle suspension is carried out using the linearization method. The initial design shown in Table 7 is chosen from Ref. 7. With the given initial design, the peak

acceleration is 331.8 in/sec^2 and the cost is 0.847 watts. Also, in this design, constraints on absorbed power on the rough highway, rear wheel-hop, and rattle space constraint between chassis and wheel assemblies are violated. This initial design, from the viewpoint of "ride comfort" and "safety," is very poor.

After the 7th iteration, the rear wheels are constantly in touch with the road surface; i.e., the wheel hop constraint is satisfied. Constraints on absorbed power and rattle space between chassis and front wheel assembly are satisfied after the 21st iteration. The optimum design, shown on Table 7, is obtained at the 23rd iteration. The peak acceleration is 342 in/sec^2 and the cost is 1.08 watts. However, the comfort and safety on each road condition are much improved. As a measure of comfort, the history of absorbed power constraint on rough highway is shown in Fig. 14. Cost and maximum violation are plotted in Fig. 15.

The general tendency in design optimization is

i) to increase stiffness and damping in the front wheel suspension and

ii) to reduce stiffness and damping in the rear wheel suspension.

This indicates that more energy should be dissipated by the front wheel suspension system to satisfy the given constraints.

Table 7. Initial and Optimum Designs

Design Variable Description			Initial Design	Optimum Design
Driver seat spring constant	[lb/in]	b_1	100.	126.258392
Spring constant of front suspension	[lb/in]	b_2	300.	356.348755
Spring constant of rear suspension	[lb/in]	b_3	300.	274.080944
Driver seat damping coefficient	[lb-sec/in]	b_4	10.	2.466310
Damping coefficient of front suspension	[lb-sec/in]	b_5	25.	49.873016
Damping coefficient of rear suspension	[lb-sec/in]	b_6	25.	14.904079

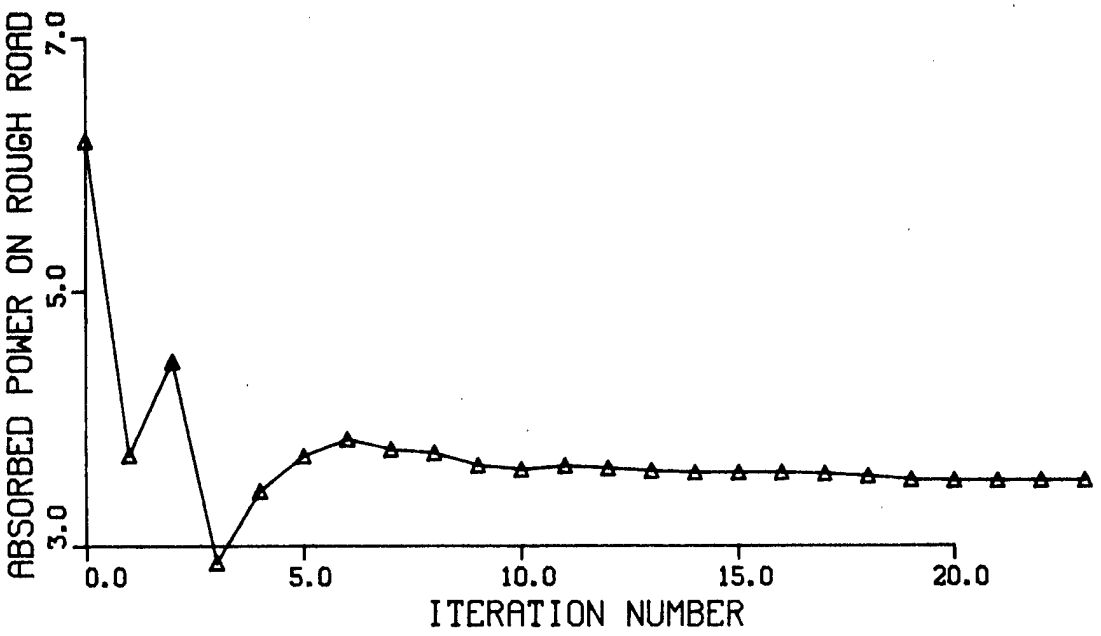

Figure 14. History of absorbed power constraint (ψ_1)

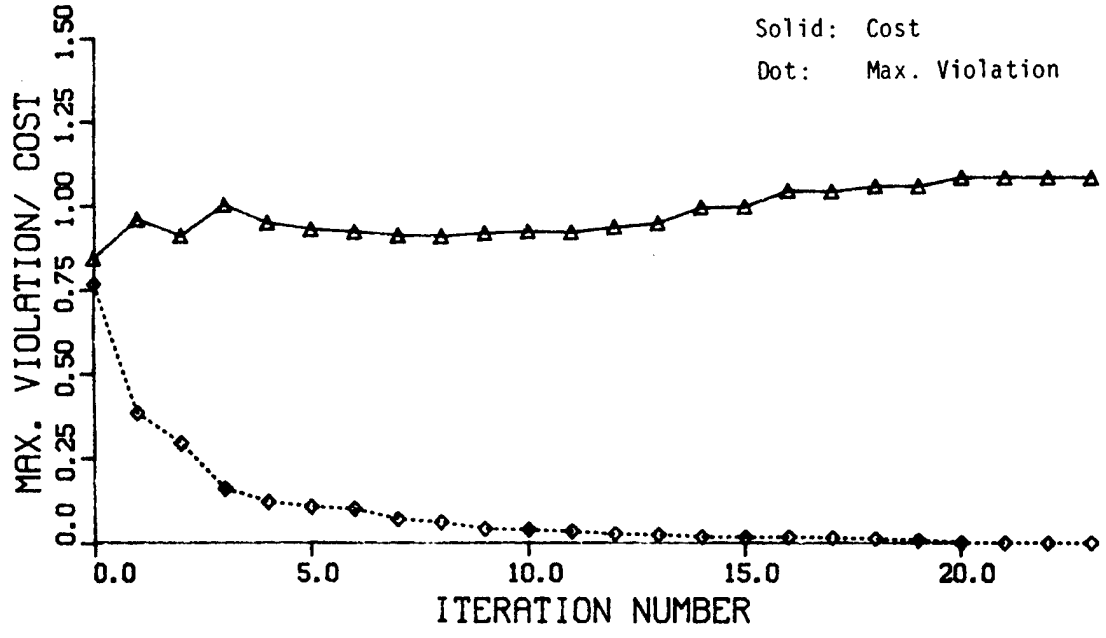

Figure 15. History of cost and maximum violation

CONCLUSION

The final results of the optimization, shown in Fig. 15 show that the absorbed power over the smooth highway has been increased slightly, but that potential hazardous characteristics of the initial design have been brought under control by virtually eliminating violations in constraints.

The success of the method for this simple dynamic system demonstrates the potential that exists in optimizing design for more complex and realistic systems. The computer optimization method, using the adjoint variable technique has been demonstrated to be a useful tool in the design of vehicle suspension.

REFERENCES

1 Murphy, N.R. and Ahlvin, R.B. (1976), AMC-74 Vehicle Dynamics Module, Technical Report No. M-76-1, Waterways Experiment Station.

2 Pradko, F., Lee, R. and Kaluza, V. (1966), "Theory of Human Vibration Response," ASME paper.

3 Lins, W.F. (1972), Human Vibration Response Measurement, Technical Report No. 1151, US Army Tank-Automotive Command.

4 Haug, E.J., Jackson, G. and Beck, R. (1982), "Full Scale Simulation of Large Scale Mechanical Systems," Proceedings, Fourth Meeting of the Coordinating Group on Modern Control Theory, Oakland University, October, 1982.

5 Lance, G.M., Liang, C-G. and McCleary, M.A., "Integrated Simulation of Vehicular Systems with Stabilization," Proceedings, Fourth Meeting of the Coordinating Group on Modern Control Theory, Oakland University, October, 1982.

6 Bryson, A.E. and Ho, Y.C. (1975), Applied Optimal Control, Wiley-Halstead, New York.

7 Haug, E.J. and Arora, J.S. (1979), Applied Optimal Design, Wiley-Interscience, New York.

8 Choi, K.K., Haug, E.J., Hou, J.W. and Sohoni, V.N. (1982), "Pshenichny's Linearization Method for Mechanical System Optimization," Journal of Mechanical Design, to appear.

Next page intentionally left blank.

COMPONENT MODE ANALYSIS OF LARGE SCALE INERTIA VARIANT MECHNAICAL SYSTEMS WITH FLEXIBLE ELEMENTS AND CONTROL SYSTEMS

Ahmed A. Shabana and Roger A. Wehage
Center for Computer Aided Design
The University of Iowa

Next page intentionally left blank.

COMPONENT MODE ANALYSIS OF LARGE SCALE INERTIA VARIANT MECHANICAL SYSTEMS WITH FLEXIBLE ELEMENTS AND CONTROL SYSTEMS

Ahmed A. Shabana and Roger A. Wehage
Center for Computer Aided Design
College of Engineering
The University of Iowa
Iowa City, Iowa 52242

ABSTRACT

A method is presented for transient dynamic analysis of mechanical systems composed of interconnected rigid and flexible bodies that undergo large angular displacements. Gross displacement of elastic bodies is represented by superposition of local linear elastic deformation on nonlinear displacement of body reference coordinate systems. Flexible bodies are thus represented by combined sets of reference and local elastic variables. Modal analysis and substructuring of the local elastic system is employed to identify all modes and eliminate the insignificant ones. Equations of motion and constraints are formulated in terms of a minimal set of modal and reference generalized coordinates, which are then dynamically adjusted to a time and inertia-variant eigenspectrum.

Control system differential equations are formulated and coupled with mechanical system models. The composite nonlinear system of equations is then numerically integrated in the time domain, to obtain complete system dynamic response. Example problems are presented to demonstrate the algorithms and computer code.

1. INTRODUCTION

Dynamic analysis of large scale spatial nonlinear elastic mechanical and control systems require efficient numerical methods. Modal techniques are desirable because they often allow reduction of problems with thousands of degrees of freedom to manageable sizes. The main difficulty with analyzing interconnected flexible mechanical systems, is that composite systems are generally inertia-variant and their corresponding eigenspectrums are time dependent. This necessitates periodic re-evaluation of eigenvectors, an expensive process that should be avoided.

To circumvent this problem, elastic properties of bodies are characterized locally, relative to body-fixed reference frames. When elastic displacements are small, which is often the case, they can be efficiently represented locally by modal analysis

techniques because the local eigenspectrums are essentially constant. Thus it is possible to efficiently reduce the dimension of a problem locally and then transform the much smaller problem to the global system and solve it using existing numerical methods.

The study of system flexibility has been a subject of major interest to many researchers. In the field of mechanics, there have been a number of attempts to arrive at general algorithms for dynamic analysis of mechanisms with elastic links [1-11]. However, most of these techniques assume that elastic deformations do not significantly affect gross body motion. Inertia forces of gross rigid body motion are first determined and then introduced as externally applied forces to the elastic model. In addition, most of these techniques are suitable for only certain classes of problems.

Some investigators [12-13] have solved simultaneously for coupled gross body and elastic deformation. However, because of the highly nonlinear nature of these equations, these techniques have not utilized coordinate reduction techniques, nor are they suitable for large scale systems.

A general method for dynamic analysis of large scale inertia-variant systems has been developed [14-15] which utilizes coordinate reduction techniques commonly employed in structural dynamics and solves simultaneously for gross body motion and elastic deformation. The method in [14] is applied to large scale control systems that contain elastic components. Mechanical systems are considered as collections of subsystems called bodies, substructures or components. Finite element or experimental methods can be used to characterize the elastic properties of each deformable body. Energy equations of subelements are written separately and the elements of each body (substructure) are then assembled using a Boolean matrix approach. The degrees of freedom of each body are then reduced using a component mode technique. Adjacent substructures are then interconnected using a Lagrange multiplier technique. Then a coordinate partitioning method [16] is employed to eliminate excess dependent equations of motion resulting from imposition of the constraint equations.

2. GENERALIZED COORDINATES AND ENERGY EQUATIONS

In order to specify the configuration of a body or substructure it is necessary to define a set of generalized coordinates such that the global position and orientation of every infinitesimal volume on the body is determined in terms of these generalized coordinates. As shown in Fig. 1 let the XYZ Cartesian coordinate system represent an inertial frame and the $X^iY^iZ^i$ axes represent a Cartesian coordinate system rigidly attached to some infinitesimal volume on the ith body. Using finite elements, the ith body is divided into a number of rigidly

interconnected subelements. The location of an arbitrary infinitesimal volume on the jth element of this body is defined in terms of two sets of generalized coordinates. The first set are reference coordinates locating the position of the body-fixed coordinate system relative to the inertial XYZ frame. The second set are elastic coordinates characterizing elastic deformation of the body. Elastic coordinates represent relative translational and angular displacement of infinitesimal volumes at nodal points on the body. In addition the location and angular orientation of every infinitesimal volume in each element can be approximated in terms of its elastic coordinates and its shape function [17].

Let $X^{ij}Y^{ij}Z^{ij}$, as shown in Fig. 1, be a Cartesian coordinate system with its origin affixed to an infinitesimal volume at some point on the jth element of the ith body, that rotates with this infinitesimal volume. The location of an arbitrary infinitesimal volume, identified by the point p^{ij} on this element, can be determined by specifying the position of $X^iY^iZ^i$ and the location of the point p^{ij} with respect to $X^iY^iZ^i$. Let $\underline{R}^i$ and and $\underline{\theta}^i$ be, respectively, the translational and rotational coordinates of $X^iY^iZ^i$ with respect to XYZ. Let $X^{ij}Y^{ij}Z^{ij}$ be a coordinate system parallel to the element $X^{ij}Y^{ij}Z^{ij}$ coordinate system and located at the origin of $X^iY^iZ^i$. Let $\underline{e}^{ij}$ be the nodal coordinates of the ijth element with respect to $X^{ij}Y^{ij}Z^{ij}$. Let $\underline{u}^{ij}$ denote the location of point p^{ij} with respect to $X^{ij}Y^{ij}Z^{ij}$. The vector $\underline{u}^{ij}$ can be written as

$$\underline{u}^{ij} = \phi^{ij}\,\underline{\bar{e}}^{ij} \qquad (1)$$

where ϕ^{ij} is the shape function of the ijth element. The position of point p^{ij} is specified by

$$\underline{r}_p^{ij} = \underline{R}^i + A^i\,C^{ij}\,\phi^{ij}\,\bar{C}^{ij}\underline{e}^{ij} \qquad (2)$$

where $A^i(\theta^i)$ is the transformation matrix from $X^iY^iZ^i$ to XYZ, $\underline{e}^{ij}$ is the vector of elastic generalized coordinates of the ith body defined relative to $X^iY^iZ^i$, and C^{ij} and $\bar{C}^{ij}$ are transformation matrices from $X^{ij}Y^{ij}Z^{ij}$ to $X^iY^iZ^i$.

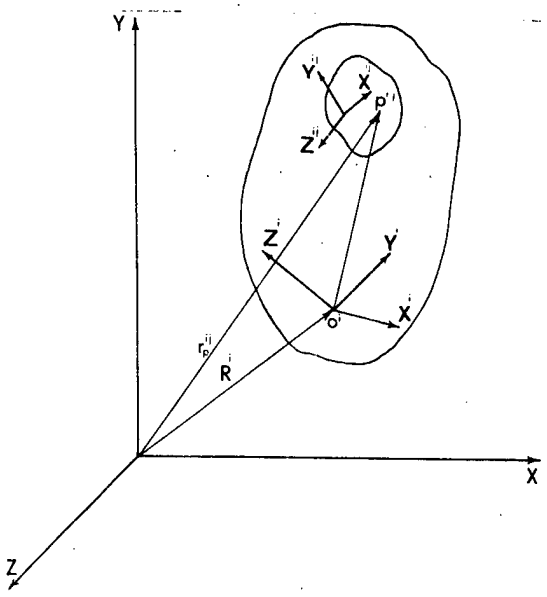

Figure 1. Generalized Coordinates

If the rotation of $X^{ij}Y^{ij}Z^{ij}$ with respect to $X^iY^iZ^i$ is small, which is the case for small elastic deformation, the matrices C^{ij} and $\bar{C}^{ij}$ are approximately constant and Eq. 2 becomes

$$\underline{r}_p^{ij} = \underline{R}^i + A^i N^{ij} \underline{e}^{ij} \tag{3}$$

where $N^{ij}(x^{ij}, y^{ij}, z^{ij})$ is the modified shape function of the ijth element given by

$$N^{ij} = C^{ij} \phi^{ij} \bar{C}^{ij} \tag{4}$$

The kinetic energy of the ijth element is obtained from the velocity vector of the infinitesimal volume at point p^{ij} on the element as

$$\dot{\underline{r}}_p^{ij} = \dot{\underline{R}}^i + \dot{A}^i N^{ij} \underline{e}^{ij} + A^i N^{ij} \dot{\underline{e}}^{ij} \tag{5}$$

where $(\cdot)$ denotes differentiation with respect to time. The second term of Eq. 5 can be expressed as

$$\dot{A}^i N^{ij} \underline{e}^{ij} = B^{ij} (\underline{\theta}^i, \underline{e}^{ij}) \dot{\underline{\theta}}^i \tag{6}$$

in order to isolate the velocity terms. Equation 5 is then expressed as

$$\dot{\underline{r}}_p^{ij} = [I \quad B^{ij} \quad A^i N^{ij}] \; [\dot{\underline{R}}^{iT} \quad \dot{\underline{\theta}}^{iT} \quad \dot{\underline{e}}^{ijT}]^T \tag{7}$$

where I is an identity matrix. The kinetic energy of the ijth element is obtained by integrating over the volume V^{ij}

$$T^{ij} = \frac{1}{2} \int_{V^{ij}} \rho^{ij} \dot{\underline{r}}_p^{ijT} \dot{\underline{r}}_p^{ij} \, dV^{ij} \tag{8}$$

where the mass density of the ijth element at p^{ij} is ρ^{ij} and the superscript T implies transpose of a matrix. Using vector notation $\dot{\underline{q}}^{ij} = [\dot{\underline{R}}^{iT} \; \dot{\underline{\theta}}^{iT} \; \dot{\underline{e}}^{ijT}]^T$ and substituting Eq. 7 into Eq. 8, kinetic energy becomes

$$T^{ij} = \frac{1}{2} \dot{\underline{q}}^{ijT} M^{ij} \dot{\underline{q}}^{ij} \tag{9}$$

where M^{ij}, the mass matrix of the ijth element, is

$$M^{ij} = \int_{V^{ij}} \rho^{ij} \begin{bmatrix} I & B^{ij} & A^{i}N^{ij} \\ B^{ij^T} & B^{ij^T}B^{ij} & B^{ij^T}A^{i}N^{ij} \\ N^{ij^T}A^{i^T} & N^{ij^T}A^{i^T}B^{ij} & N^{ij^T}N^{ij} \end{bmatrix} dV^{ij} \tag{10}$$

The submatrix $N^{ij^T}N^{ij}$ associated with element elastic generalized coordinates is constant (see Eqs. 1 and 4).

Kinetic energy T^i of the ith body is obtained by summing over each of its elements. Denoting the number of elements by n^i

$$T^i = \sum_{j=1}^{n^i} T^{ij} \tag{11}$$

In vector notation $\bar{q}^i = [q^{i1^T}, q^{i2^T}, \ldots, q^{in^{iT}}]^T$, $\bar{M}^i = \text{diag}\,(M^{i1}, M^{i2}, \ldots, M^{in^i})$, and Eq. 11 becomes

$$T^i = \frac{1}{2}\dot{\bar{q}}^{i^T}\bar{M}^i\dot{\bar{q}}^i \tag{12}$$

The vector $\dot{\bar{q}}^i$ is partitioned as

$$\dot{\bar{q}}^i = [\dot{\bar{q}}_r^{i^T}, \dot{\bar{q}}_f^{i^T}]^T \tag{13}$$

where $\bar{q}_r^i = [\underline{R}^{i^T}, \underline{\theta}^{i^T}]^T$ are reference coordinates locating $X^iY^iZ^i$ relative to XYZ and $\bar{q}_f^i = [\underline{e}^{i1^T}, \underline{e}^{i2^T}, \ldots, \underline{e}^{in^{iT}}]^T$ are elastic generalized coordinates of the ith body.

Since $\bar{q}_f^i$ is defined relative to $X^iY^iZ^i$ a constant Boolean matrix can be employed to impose constraints between adjacent elements on the ith body. These constraints in matrix form are

$$\bar{q}^i = B_1^i \, q^i \tag{14}$$

Differentiating Eq. 14 with respect to time and substituting into Eq. 12 yields

$$T^i = \frac{1}{2} \dot{q}^{iT} M^i \dot{q}^i \tag{15}$$

where

$$M^i = B_1^{iT} \bar{M}^i B_1^i \tag{16}$$

The kinetic energy of the ith body can be partitioned as

$$T^i = \frac{1}{2} \begin{Bmatrix} \dot{q}_r^i \\ \dot{q}_f^i \end{Bmatrix}^T \begin{bmatrix} m_{rr}^i(q^i) & m_{rf}^i(q^i) \\ m_{fr}^i(q^i) & m_{ff}^i \end{bmatrix} \begin{Bmatrix} \dot{q}_r^i \\ \dot{q}_f^i \end{Bmatrix} \tag{17}$$

where subscripts r and f denote reference and flexible coordinates respectively. Observe that m_{ff}^i is a constant matrix and also that coupling between elastic and reference coordinates exists through the nonlinear matrices m_{fr}^i and m_{rf}^i. Elastic and reference coordinates can be dynamically decoupled by neglecting these two matrices and the dependence of B_1^{ij} on elastic coordinates.

Strain energy of the ijth elastic element is given by [17]

$$U^{ij} = \frac{1}{2} \int_{V^{ij}} \varepsilon^{ij^T} \sigma^{ij} \, dV^{ij} \tag{18}$$

where ε^{ij} and σ^{ij} are the respective strain and stress components at the infinitesimal volume. The stress-strain equation is given by the elastic constitutive relation

$$\underline{\sigma}^{ij} = G^{ij}\underline{\varepsilon}^{ij} \tag{19}$$

and the strain-displacement relation can be expressed as

$$\begin{aligned}\underline{\varepsilon}^{ij} &= D^{ij}\underline{u}^{ij} \\ &= D^{ij}N^{ij}\underline{e}^{ij}\end{aligned} \tag{20}$$

where D^{ij} is a differential operator relating strains and displacements. Substituting Eqs. 19 and 20 into Eq. 18 yields

$$\begin{aligned}U^{ij} &= \frac{1}{2}\int_{V^{ij}} \underline{e}^{ij^T}(D^{ij}N^{ij})^T G^{ij} D^{ij}N^{ij}\underline{e}^{ij}dV^{ij} \\ &= \frac{1}{2}\,\underline{e}^{ij^T}K^{ij}\underline{e}^{ij}\end{aligned} \tag{21}$$

where K^{ij} is the ijth element stiffness matrix. The element stiffness matrix is constant and the strain energy expression is independent of reference coordinates because elastic generalized coordinates are defined with respect to $X^iY^iZ^i$. The total strain energy of the ith body is

$$\begin{aligned}U^i &= \frac{1}{2}\,\bar{q}_f^{i^T}\,\bar{K}_{ff}^i\,\bar{q}_f^i \\ &= \frac{1}{2}\begin{Bmatrix}\bar{q}_r^i \\ \bar{q}_f^i\end{Bmatrix}^T\begin{bmatrix}0 & 0 \\ 0 & \bar{K}_{ff}^i\end{bmatrix}\begin{Bmatrix}\bar{q}_r^i \\ \bar{q}_f^i\end{Bmatrix}\end{aligned} \tag{22}$$

where $\bar{K}_{ff}^i = \text{diag}\,(\bar{K}_{ff}^{i1}, \bar{K}_{ff}^{i2},\ldots,\bar{K}_{ff}^{in^i})$

Substituting Eq. 14 into Eq. 22 and partitioning gives

$$U^i = \frac{1}{2}\begin{Bmatrix}q_r^i \\ q_f^i\end{Bmatrix}^T\begin{bmatrix}0 & 0 \\ 0 & K_{ff}^i\end{bmatrix}\begin{Bmatrix}q_r^i \\ q_f^i\end{Bmatrix} \tag{23}$$

where $\underline{q}_r^i$ and $\underline{q}_f^i$ are as defined before and K_{ff}^i is the stiffness matrix associated with the ith body elastic coordinates.

Finally virtual work of the ijth element is

$$\delta W^{ij} = \underline{Q}^{ij^T} \delta \underline{q}^{ij} \tag{24}$$

where $\underline{Q}^{ij}$ is the vector of generalized forces associated with the generalized coordinates $\underline{q}^{ij}$. All forces except workless constraint forces between elements are included in δW^{ij}. The virtual work of the ith body is

$$\delta W^i = [\underline{Q}_r^{i^T} \quad \underline{Q}_f^{i^T}] \; [\delta \underline{q}_r^{i^T} \quad \delta \underline{q}_f^{i^T}]^T \tag{25}$$

where $\underline{Q}_r^i$ and $\underline{Q}_f^i$ are respectively generalized forces associated with reference and elastic generalized coordinates.

3. SUBSTRUCTURE SYSTEM EQUATIONS OF MOTION

The composite vector of all system generalized coordinates is designated as $\underline{q} = [\underline{q}^{1^T}, \underline{q}^{2^T}, \ldots, \underline{q}^{N^T}]^T$, where N is the total number of bodies (substructures) in the system. Nonlinear constraint equations between adjacent substructures can be written in vector form as

$$\underline{\Phi}(\underline{q}, t) = \underline{0} \tag{26}$$

where $\underline{\Phi}(\underline{q}, t) = [\Phi_1(\underline{q}, t), \ldots, \Phi_m(\underline{q}, t)]^T$ and all equations are assumed to be independent. The equations of motion of the ith substructure can be written as [18].

$$\frac{d}{dt}\left(\frac{T_{\cdot i}^i}{\underline{q}}\right)^T - \left(\frac{T_i^i}{\underline{q}}\right)^T + \left(\frac{U_i^i}{\underline{q}}\right)^T - \underline{Q}^i + \frac{\underline{\Phi}^T}{\underline{q}_i}\underline{\lambda} = \underline{0} \tag{27}$$

where $\underline{\lambda}$ is the vector of Lagrange multipliers.

Recall that all elastic deformation in the ith body is defined relative to the body reference frame attached to node ℓ which implies no elastic displacement at node ℓ. Thus

$$\underline{q}^i_{f_\ell} = \underline{0} \tag{28}$$

where $\underline{q}^i_{f_\ell}$ is the vector of elastic generalized coordinates at node ℓ. Denoting $\underline{q}^i_f = [\underline{q}^{iT}_{f_\ell} \; \bar{p}^{iT}_f]^T$, where $\bar{p}^i_f$ is the set of elastic generalized coordinates of the ith body excluding node ℓ, Eq. 27 reduces to

$$\bar{M}^i(\bar{p}^i)\,\ddot{\bar{p}}^i + \bar{K}^i\bar{p}^i = \bar{Q}^i(\bar{p}, \dot{\bar{p}}, t) + \underline{F}^i(\bar{p}^i, \dot{\bar{p}}^i) - \underline{\Phi}^T_{\underline{p}_i}\underline{\lambda} \tag{29}$$

which is the general form of the equations of motion for the ith body. The vector $\underline{F}^i$ absorbs quadratic velocity terms of Eq. 27. These equations along with Eq. 26 form the constrained equations of motion of the substructure. A coordinate reduction technique is now employed to eliminate insignificant elastic degrees of freedom.

4. COORDINATE REDUCTION

Efficient solution of the system equations of motion requires a transformation from the space of system nodal elastic generalized coordinates to the space of system modal generalized coordinates with lower dimension. This transformation is a constant mapping [19]. The problem is complicated by a time variant system transfer function which implies that monitoring the frequency content of external forcing functions alone is usually not sufficient for predicting mode excitation because the mass matrix depends on generalized coordinates. Accordingly, no judgement can be made beforehand of the number of significant modes to be retained for an accurate solution.

The method developed here is based on solving the eigenvalue problem of the substructure once. From Fourier analysis of the forcing functions, an initial estimate of the number of modes to be retained is made, and during the simulation additional eigenvectors are recalled or deleted as required. For the purpose of determining eigenvalues and eigenvectors, if a substructure is assumed to vibrate freely about a reference configuration, Eq. 29 yields

$$\bar{m}^i_{ff}\ddot{\bar{p}}^i_f + \bar{k}^i_{ff}\bar{p}^i_f = \underline{0} \tag{30}$$

where $\bar{m}^i_{ff}$ and $\bar{k}^i_{ff}$ are the respective mass and stiffness matrices associated with the elastic coordinates. The stiffness matrix $\bar{k}^i_{ff}$ is positive definite because the reference coordinate system is fixed. Equation 30 yields a set of eigenvectors and a modal matrix. A coordinate transformation from the physical elastic coordinates to the modal coordinates is obtained by

$$\bar{p}^i_f = B^i_2 \, \chi^i \tag{31}$$

where B^i_2 is the modal matrix consisting of the eigenvectors obtained from Eq. 30, and χ^i is a vector containing the modal coordinates. Using Eq. 31 the reference and elastic generalized coordinates are written in terms of the reference and modal coordinates as follows

$$\begin{Bmatrix} \bar{p}^i_r \\ \bar{p}^i_f \end{Bmatrix} = \begin{bmatrix} I & 0 \\ 0 & B^i_2 \end{bmatrix} \begin{Bmatrix} \bar{p}^i_r \\ \chi^i \end{Bmatrix} \tag{32}$$

Substituting Eq. 32 into Eq. 29 and premultiplying by the transpose of the matrix in Eq. 32 yields

$$\bar{M}^i(p^i)\ddot{p}^i = \bar{P}^i(p, \dot{p}, t) - \Phi^T_{p^i}(p, t)\lambda \tag{33}$$

The constraint Jacobian matrix of Eq. 33 is evaluated in terms of physical coordinates and converted to modal coordinates using Eq. 32 as

$$\begin{aligned} \Phi_{pi} &= \Phi_{\bar{p}^i}(\partial \bar{p}^i / \partial p^i) \\ &= \Phi_{\bar{p}^i} \begin{bmatrix} I & 0 \\ 0 & B^i_2 \end{bmatrix} \end{aligned} \tag{34}$$

Equation 33 represents the reduced system of equations for the ith substructure. The number of equations in Eq. 33 depends on the number of elastic degrees of freedom required to achieve the desired accuracy.

5. CHARACTERIZATION OF PLANAR ELASTIC SYSTEMS

Figure 2 illustrates a typical jth element denoted as ijth on the ith body. The element X^{ij} axis is located at an angle β^{ij} relative to the body-fixed X^i coordinate axis. The reference coordinates for this body are the translational variables (x^i, y^i) and the rotational variable θ^i. This set of coordinates defines the position of the body-fixed coordinate system X^iY^i relative to the inertial X-Y frame. The elastic generalized coordinates are defined initially with respect to a coordinate $\bar{X}^{ij}$ $\bar{Y}^{ij}$ system which is always parallel to the element X^{ij} Y^{ij} axis with origin located at the point 0^i. This set of generalized coordinates is denoted by $\underline{\bar{e}}^{ij}_k$ $(k = 1, \ldots, 6)$. These coordinates are called the nodal coordinates and represent the location of the nodes and slopes of reference lines at the nodes relative to $\bar{X}^{ij}$ $\bar{Y}^{ij}$.

The location of an arbitrary point p^{ij} on the ijth element, with respect to $\bar{X}^{ij}$ Y^{ij}, can be expressed as [20]:

$$\underline{w}^{ij} = \phi^{ij}\, \underline{\bar{e}}^{ij} \tag{35}$$

where

$$\phi^{ij} = \begin{bmatrix} 1 - \xi^{ij} & 0 & 0 & \xi^{ij} & 0 & 0 \\ 0 & 1 - 3(\xi^{ij})^2+2(\xi^{ij})^3 & \ell^{ij}[\xi^{ij}-2(\xi^{ij})^2+(\xi^{ij})^3] & 0 & 3(\xi^{ij})^2-2(\xi^{ij})^3 & \ell^{ij}[(\xi^{ij})^3-(\xi^{ij})^2] \end{bmatrix} \tag{36}$$

and

$$\xi^{ij} = x^{ij}/\ell^{ij} \tag{37}$$

A transformation is employed to define $\underline{w}^{ij}$ with respect to X^i Y^i as follows

$$\underline{w}^{ij} = C^{ij} \phi^{ij} \bar{\underline{e}}^{ij} \tag{38}$$

where

$$C^{ij} = \begin{bmatrix} \cos \beta^{ij} & -\sin \beta^{ij} \\ \sin \beta^{ij} & \cos \beta^{ij} \end{bmatrix} \tag{39}$$

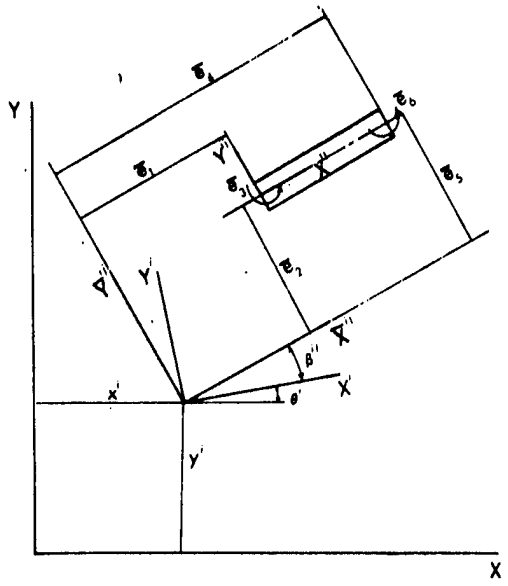

Figure 2. Two Dimensional Beam Element

The compatibility conditions between elements on a given substructure are simpler if the generalized elastic coordinates are defined with respect to the body-fixed coordinate system of the substructure. This is accomplished by the following transformation

$$\bar{\underline{e}}^{ij} = \bar{C}^{ij} \underline{e}^{ij} \tag{40}$$

where $\underline{e}^{ij}$ is the set of generalized elastic coordinates defined with respect to X^i Y^i, and

$$\bar{C}^{ij} = \begin{bmatrix} \bar{C}_1^{ij} & 0 \\ 0 & \bar{C}_1^{ij} \end{bmatrix} \tag{41}$$

with

$$\bar{C}_1^{ij} = \begin{bmatrix} \cos \beta^{ij} & \sin \beta^{ij} & 0 \\ -\sin \beta^{ij} & \cos \beta^{ij} & 0 \\ 0 & 0 & 1 \end{bmatrix} \tag{42}$$

Substituting Eq. 40 into Eq. 38 yields

$$\underline{w}^{ij} = C^{ij}\ \phi^{ij}\ \bar{C}^{ij}\ \underline{e}^{ij} \tag{43}$$

It is important to note that the variation in the angle β^{ij} is assumed to be small, thus the matrices C^{ij} and $\bar{C}^{ij}$ are assumed constant. Finally, Eq. 43 can be written as

$$\underline{w}^{ij} = N^{ij}\ \underline{e}^{ij} \tag{44}$$

where

$$N^{ij} = C^{ij}\ \phi^{ij}\ \bar{C}^{ij} \tag{45}$$

The position vector $\underline{r}_p^{ij}$ of an arbitrary point p^{ij} on the ijth element can be expressed as

$$\underline{r}_p^{ij} = \underline{R}^i + A^i\ N^{ij}\ \underline{e}^{ij} \tag{46}$$

where

$$\underline{R}^i = [x^i\ y^i]^T$$

and

$$A^i = \begin{bmatrix} \cos\theta^i & -\sin\theta^i \\ \sin\theta^i & \cos\theta^i \end{bmatrix} \tag{47}$$

Differentiating Eq. 46 with respect to time gives

$$\dot{\underline{r}}_p^{ij} = \dot{\underline{R}}^i + \dot{A}^i\ N^{ij}\ \underline{e}^{ij} + A^i\ N^{ij}\ \dot{\underline{e}}^{ij} \tag{48}$$

where

$$\dot{A}^i = \dot{\theta}^i \begin{bmatrix} -\sin\theta^i & -\cos\theta^i \\ \cos\theta^i & -\sin\theta^i \end{bmatrix}$$

$$= \dot{\theta}^i A^{i'} \tag{49}$$

and $A^{i'}$ is the partial derivative of A^i with respect to the reference rotational degree of freedom θ^i. Substituting Eq. 49 into Eq. 48 and writing $\dot{\underline{r}}_p^{ij}$ in partitioned form yields

$$\dot{\underline{r}}_p^{ij} = \begin{bmatrix} I & A^{i'}N^{ij}\underline{e}^{ij} & A^iN^{ij} \end{bmatrix} \begin{Bmatrix} \dot{\underline{R}}^i \\ \dot{\theta}^i \\ \dot{\underline{e}}^{ij} \end{Bmatrix} \tag{50}$$

Equation 50 is equivalent to Eq. 7 in the general formulation with the matrix B^{ij} given by

$$B^{ij} = A^{i'}N^{ij}\underline{e}^{ij} \tag{51}$$

The kinetic energy expression for the ijth element is given by

$$T^{ij} = \frac{1}{2}\int_{V^{ij}} \rho^{ij}\, \dot{\underline{r}}^{ij^T}\, \dot{\underline{r}}_p^{ij}\, dV^{ij}$$

$$= \frac{1}{2}\dot{\underline{q}}^{ij^T} M^{ij} \dot{\underline{q}}^{ij} \tag{52}$$

where V^{ij} is the element volume, ρ^{ij} is the density of element material $\underline{q}^{ij} = [\underline{R}^{i^T}\ \theta^i\ \underline{e}^{ij^T}]^T$ and

$$M^{ij} = \int_{V^{ij}} \rho^{ij} \begin{bmatrix} I & B^{ij} & A^i N^{ij} \\ B^{ij^T} & B^{ij^T} B^{ij} & B^{ij^T} A^i N^{ij} \\ N^{ij^T} A^{i^T} & N^{ij^T} A^{i^T} B^{ij} & N^{ij^T} N^{ij} \end{bmatrix} dV^{ij} \tag{53}$$

The mass matrix m_{ff}^{ij} associated with the flexible coordinates is the same matrix that occurs frequently in the finite element approach [20].

Utilizing orthonormality of $A^{i'}$, the central term of Eq. 53 becomes

$$\int_{V^{ij}} \rho^{ij} B^{ij^T} B^{ij} dV^{ij} = \underline{e}^{ij^T} \int_{V^{ij}} \rho^{ij} N^{ij^T} N^{ij} dV^{ij} \underline{e}^{ij}$$

$$= \underline{e}^{ij^T} m_{ff}^{ij} \underline{e}^{ij} \tag{54}$$

Similarly

$$\int_{V^{ij}} \rho^{ij} B^{ij} dV^{ij} = A^{i'} \int_{V^{ij}} \rho^{ij} N^{ij} dV^{ij} \underline{e}^{ij} = A^{i'} C^{ij} S_1^{ij} \bar{C}^{ij} \underline{e}^{ij}$$

$$= A^{i'} S^{ij} \underline{e}^{ij} \tag{55}$$

where

$$S_1^{ij} = \frac{m^{ij}}{12} \begin{bmatrix} 6 & 0 & 0 & 6 & 0 & 0 \\ 0 & 6 & \ell^{ij} & 0 & 6 & -\ell^{ij} \end{bmatrix} \tag{56}$$

where m^{ij} and ℓ^{ij} are the mass and length of the ijth element respectively.

The matrix product $A^{i'^T} A^i$ is skew symmetric, i.e.,

$$\tilde{I} = A^{i'^T} A^i = \begin{bmatrix} 0 & 1 \\ -1 & 0 \end{bmatrix} \tag{57}$$

Thus from Eq. 51

$$\int_{V^{ij}} \rho^{ij} B^{ij^T} A^{i} N^{ij} dV^{ij} = \underline{e}^{ij^T} \int_{V^{ij}} \rho^{ij} N^{ij^T} \tilde{I} N^{ij} dV^{ij}$$

$$= \underline{e}^{ij^T} \bar{C}^{ij^T} \tilde{S}_1^{ij} \bar{C}^{ij} = \underline{e}^{ij^T} \tilde{S}^{ij} \tag{58}$$

where $\tilde{S}_1^{ij}$ is a skew symmetric matrix given by

$$\tilde{S}_1^{ij} = \frac{m^{ij}}{60} \begin{bmatrix} 0 & 21 & 3\ell^{ij} & 0 & 9 & -2\ell^{ij} \\ -21 & 0 & 0 & -9 & 0 & 0 \\ -3\ell^{ij} & 0 & 0 & -2\ell^{ij} & 0 & 0 \\ 0 & 9 & 2\ell^{ij} & 0 & 21 & -3\ell^{ij} \\ -9 & 0 & 0 & -21 & 0 & 0 \\ 2\ell^{ij} & 0 & 0 & 3\ell^{ij} & 0 & 0 \end{bmatrix} \tag{59}$$

It is noteworthy that the flexibility mass matrix m_{ff}^{ij} is given in the finite element literature [20], thus it is necessary to carry out only the integrations required for the matrices S^{ij} and $\tilde{S}^{ij}$ to completely define the mass matrix in Eq. 53 and accordingly the kinetic energy expression in Eq. 52. Using the above notations, the mass matrix is written as

$$M^{ij} = \begin{bmatrix} m^{ij}I & & \text{(symmetric)} \\ \underset{(1\times 2)}{\underline{e}^{ij^T} S^{ij^T} A^{i,T}} & \underline{e}^{ij^T} m_{ff}^{ij} \underline{e}^{ij} & \\ \underset{(6\times 2)}{S^{ij^T} A^{i^T}} & \underset{(6\times 1)}{\tilde{S}^{ij^T} \underline{e}^{ij}} & \underset{(6\times 6)}{m_{ff}^{ij}} \end{bmatrix} \quad (60)$$

where I is a (2×2) identity matrix. The total kinetic energy of the ith body is given by

$$T^i = \sum_{j=1}^{n^i} T^{ij}$$

$$= \frac{1}{2} \dot{q}^{i^T} M^i \dot{q}^i \quad (61)$$

where $q^i = [\underline{R}^{i^T} \ \theta^i \ \underline{q}_f^{i^T}]^T$ represents the generalized coordinates of the ith substructure, $\underline{q}_f^i$ the elastic coordinates,

$$M^i = \begin{bmatrix} m^i I & & \text{(symmetric)} \\ \underline{q}_f^{i^T} S^{i^T} A^{i,T} & \underline{q}_f^{i^T} m_{ff}^i \underline{q}_f^i & \\ S^{i^T} A^{i^T} & \tilde{S}^{i^T} \underline{q}_f^i & m_{ff}^i \end{bmatrix} \quad (62)$$

and

m^i is the total mass of the substructure

S^i is the composite matrix of the S^{ij} matrices of the individual elements

m_{ff}^i is the composite matrix of the m_{ff}^{ij} matrices of the individual elements

$\tilde{S}^i$ is the composite matrix of the $\tilde{S}^{ij}$ matrices of the individual elements

It is important to note that each of the above matrices is constant and the implied assembly need only be done once. This is because the elastic generalized coordinates of each substructure are defined locally which leads to time invariant compatibility conditions between the elements.

Neglecting shear deformation, the strain energy of the jth element on the ith body is given by

$$U^{ij} = \frac{1}{2}\int_0^{\ell^{ij}} [E^{ij}I^{ij}(v^{ij''})^2 + E^{ij}A^{ij}(u^{ij'})^2]dx^{ij} \qquad (63)$$

where primes indicate derivatives with respect to x^{ij}, E^{ij} is the modulus of elasticity, I^{ij} is the second area moment and A^{ij} is the element cross-sectional area.

Using Eq. 35, Eq. 63 becomes

$$\begin{aligned} U^{ij} &= \frac{1}{2}\,\underline{\bar{e}}^{ij^T}\bar{K}_{ff}^{ij}\,\underline{\bar{e}}^{ij} \\ &= \frac{1}{2}\,\underline{e}^{ij^T}\,\bar{C}^{ij^T}\,\bar{K}_{ff}^{ij}\,\bar{C}^{ij}\,\underline{e}^{ij} \\ &= \frac{1}{2}\,\underline{e}^{ij^T}\,K_{ff}^{ij}\,\underline{e}^{ij} \end{aligned} \qquad (64)$$

where K_{ff}^{ij} is the element stiffness matrix defined with respect to the body-fixed coordinate system.

Again, the stiffness matrix is constant because the elastic generalized coordinates are defined with respect to the body-fixed coordinate system. The total strain energy of the ith body is obtained as follows

$$\begin{aligned} U^i &= \sum_{j=1}^{n^i} U^{ij} \\ &= \begin{Bmatrix} q_r^i \\ q_f^i \end{Bmatrix}^T \begin{bmatrix} 0 & 0 \\ 0 & K_{ff}^i \end{bmatrix} \begin{Bmatrix} q_r^i \\ q_f^i \end{Bmatrix} \\ &= \frac{1}{2}\,q^{i^T}K^i q^i \end{aligned} \qquad (65)$$

where K_{ff}^{i} is the assembled stiffness matrix of the ith body and

$$K^{i} = \begin{bmatrix} 0 & 0 \\ 0 & K_{ff}^{i} \end{bmatrix} \tag{66}$$

6. NUMERICAL EXAMPLE

The Peaucillier mechanism shown in Fig. 3 is designed to generate a straight line path. Its geometry is such that BC = BP = EC = EP = 0.359m and AB = AE = 0.254m. Points A, C and P should always lie on a straight line passing through A. The mechanism always satisfies the condition AC × AP = C, where C is a constant called the inversion constant. In case AD = CD, point C must trace a circular arc and point P should follow an exact straight line. However this will not be the case when flexibility of the links is considered.

All mechanism members are assumed constructed of steel bars of circular cross-sectional area of diameter 0.01m. The input crank OC is assumed to rotate such that

$$\theta = \sin 200t$$

where θ is the angular rotation of the input link with respect to the XY inertial frame and t is time.

Links BP and EP are assumed flexible and their body-fixed coordinate systems are located at their corresponding centers of mass. Each of these links are divided into two beam elements. Because of the flexibility of these links, point P will no longer move in a straight line. The deviation β of point P is plotted in Fig. 4 versus Ω, where $\Omega = 200t$. The figure shows two solutions. The first is a two-mode solution, in which the deformation of each flexible link is described by its corresponding two lowest modes. Second, a four-mode solution described by the lowest four modes of each flexible link. The figure indicates that the first two modes of each link are dominant. The displacement β can be substantially reduced if the amplitude of the dominant modes is kept small.

Equation (33), representing the equations of motion of the ith substructure, is expressed in terms of reference and modal coordinates. Therefore a modal control method [21] can be employed to control the deviation β of point P. Equation (33), in this case, can be written as

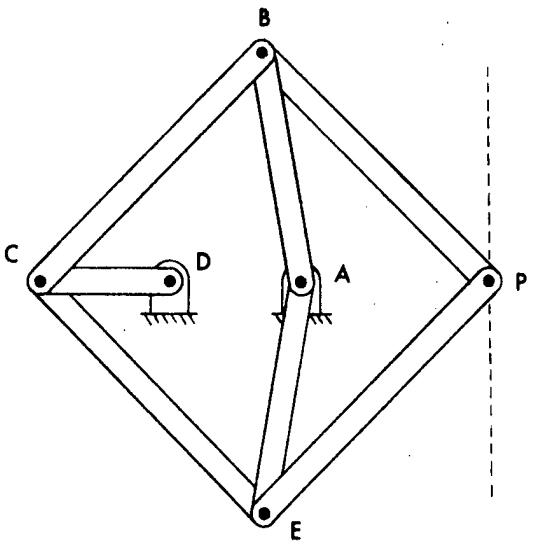

Figure 3. Peaucillier Lipkin Mechanism

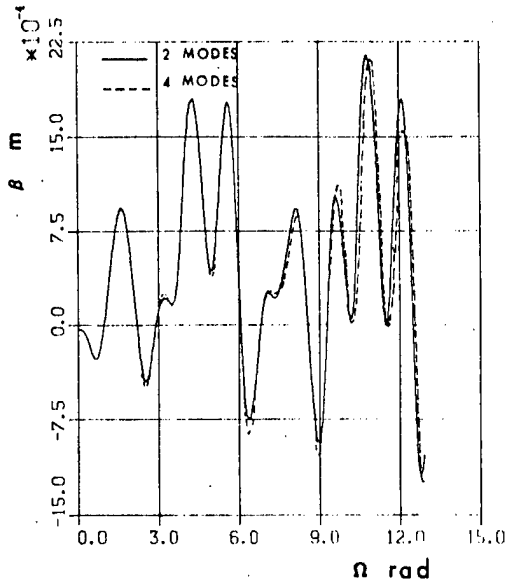

Figure 4. The Two-Mode and Four-Mode Solution

$$\bar{M}^i(\underline{p}^i)\ddot{\underline{p}} = \bar{\underline{P}}^i(\underline{p},\dot{\underline{p}},t) - \underline{\Phi}^T_{\underline{p}^i}(\underline{p},t)\underline{\lambda} - \underline{u}(\underline{p},t)$$

Where $\underline{u}(\underline{p},t)$ is a control input. This control input represents a controller to the system designed in such a way to reduce the deviation β of point P. This displacement can be measured physically using a displacement meter. However, β can also be expressed mathematically as a function of the elastic modes which are obtained in the solution of Eq. 33. Controlling these modes will reduce the deviation of P from the desired path. In the present example $\underline{u}(\underline{p},t)$ is designed as a proportional controller which is expressed mathematically as

$$\underline{u}(\underline{p},t) = G\ \underline{p}$$

where G is a diagonal matrix containing the gain factors (Fig. 5). This matrix is defined such that the dominant modes are multiplied by equal gain. The modal coordinates, for different values of gain are shown in Figs. 6 to 9. Figure 10 shows β of the four-mode solution for different gains. It can be seen that increasing the gain leads to a significant reduction in the modal coordinates and, accordingly, to a reduction in β. This increase in the gain is physically equivalent to a change in the elastic member stiffness which can be accomplished by changing the member dimensions and shapes.

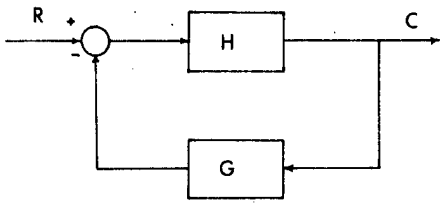

Figure 5. The System Representation with Proportional Controller

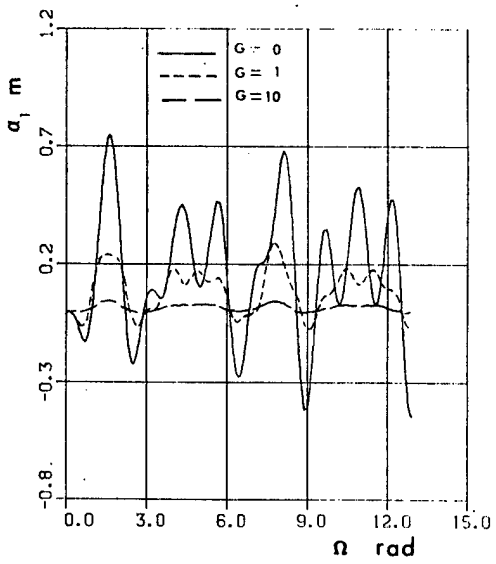

Figure 6. Effect of the Gain on the First Mode of Link BP

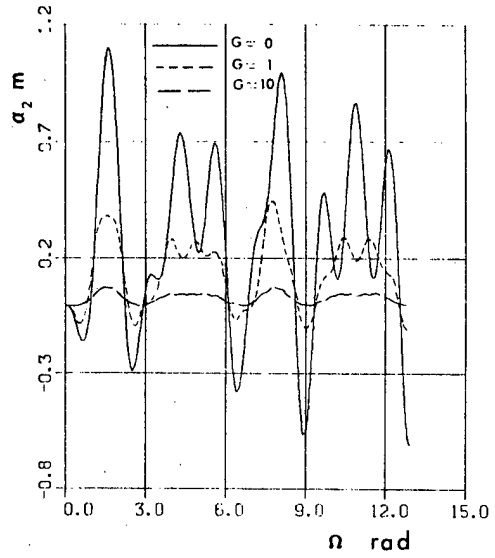

Figure 7. Effect of the Gain on the Second Mode of Link BP

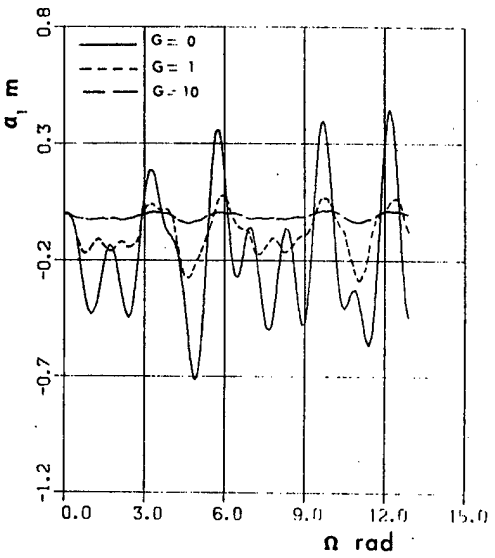

Figure 8. Effect of the Gain on the First Mode of Link EP

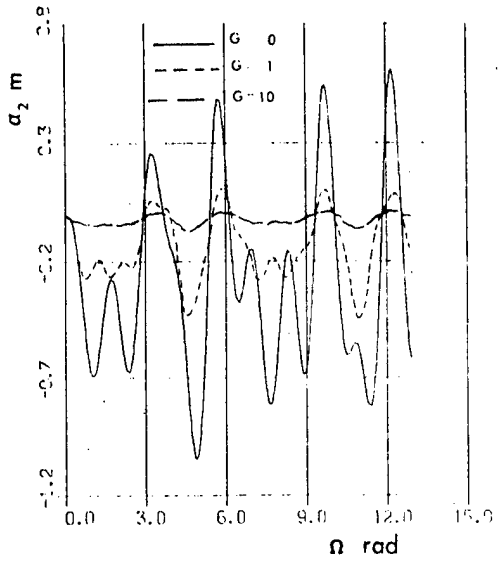

Figure 9. Effect of the Gain on the Second Mode of Link EP

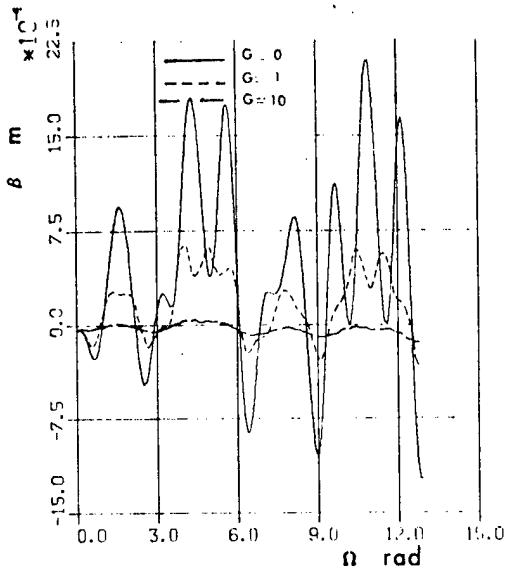

Figure 10. Four-Mode Solution for Different Gain Factors

7. CONCLUSION

A method for the dynamic analysis of large scale inertia-variant mechanical systems with flexible components is presented. The resultant method is capable of analyzing complex mechanical systems and it utilizes coordinate reduction techniques. The final form of the system equations of motion is expressed in terms of the reference and modal coordinates. The applicability of the method to control systems is demonstrated through a simple example. The modal control technique is employed to control the dominant modes of the system components.

8. REFERENCES

1. Winfrey, R.C., "Elastic Link Mechanism Dynamics," Journal of Engineering for Industry, Trans. ASME, February 1971, pp. 268-272.

2. Winfrey, R.C., "Dynamic Analysis of Elastic Link Mechanisms by Reduction of Coordinates," Journal of Engineering for Industry, Trans. ASME, May 1972, pp. 577-582.

3. Imdad, Imam, Sandor, G.N., and Kramer, S.N., "Deflection and Stress Analysis in High Speed Planar Mechanisms with Elastic Links," Journal of Engineering for Industry, Trans. ASME, May 1973, pp. 541-548.

4. Erdman, A.G., Sandor, G.N., and Oakberg, R.G., "A General Method for Kineto-Elastodynamic Analysis and Synthesis," Journal of Engineering for Industry, Trans. ASME, November 1972, pp. 1193-1205.

5. Sadler, J.P., and Sandor, G.N., "A Lumped Parameter Approach to Vibration and Stress Analysis of Elastic Linkages," Journal of Engineering for Industry, Trans. ASME, May 1973, pp. 549-557.

6. Winfrey, R.C., Anderson, R.V., and Gnilka, C.W., "Analysis of Elastic Machinery with Clearance," Journal of Engineering for Industry, Trans. ASME, August 1973, pp. 695-703.

7. Chu, S.C., and Pan, K.C., "Dynamic Response of a High-Speed Slider-Crank Mechanism with an Elastic Connecting Rod," Journal of Engineering for Industry, May 1975, pp. 542-550.

8. Imdad, Imam, and Sandor, G.N., "High-Speed Mechanism Design - A General Analytical Approach," Journal of Engineering for Industry, May 1975, pp. 609-628.

9. Kohli, D., Hunter, D., and Sandor, G.N., "Elastodynamic Analysis of a Completely Elastic System," Journal of Engineering for Industry, Trans. ASME, August, 1977, pp. 604-609.

10. Midha, A., Erdman, A.G., and Frohrib, D.A., "An Approximate Method for the Dynamic Analysis of Elastic Linkage," Journal of Engineering for Industry, Trans. ASME, May 1977, pp. 449-455.

11. Midha, A. Erdman, A.G., and Forhrib, D.A., "Finite Element Approach to Mathematical Modeling of High Speed Elastic Linkage," Mechanism and Machine Theory, 1978, Vol. 13, pp. 603-618.

12. Cavin, R.K., and Dusto, A.R., "Hamilton's Principle: Finite Element Methods and Flexible Body Dynamics," AIAA Journal, Vol. 15, No. 12, December 1977, pp. 1684-1690.

13. Song, J.O., and Haug, E.J., "Dynamic Analysis of Planar Flexible Mechanisms," Computer Methods in Applied Mechanics and Engineering, Vol. 24, 1980, pp. 359-381.

14. Shabana, A.A., and Wehage, R.A., "Variable Degree of Freedom Component Mode Analysis of Inertia Variant Flexible Mechanical System," submitted to ASME Journal of Mechanical Design, Feb. 1982.

15. Shabana, A.A., "Dynamic Analysis of Large Scale Inertia Variant Flexible Systems," Doctoral dissertation, Dept. of Mech. Eng., University of Iowa, Dec. 1982.

16. Wehage, R.A., and Haug, E.J., "Generalized Coordinate Partitioning for Dimension Reduction in Analysis of Constrained Dynamic Systems," Journal of Mechanical Design, Vol. 104, 1982, pp. 247-255.

17. Zienkiewicz, O.C., The Finite Element Method, Third Edition, McGraw-Hill Book Co., 1977.

18. Goldstein, H., Classical Mechanics, Addison Wesley, 1950.

19. Bathe, K.J., and Wilson, E.L., Numerical Methods in Finite Element Analysis, Prentice-Hall, Englewood Cliffs, N.J., 1976.

20. Przemieniecki, J.S., Theory of Matrix Structural Analysis, McGraw-Hill, 1968.

21. Takahashi, Y., Rabin, M.J., and Auslander, D.M., Control and Dynamic Systems, Addison Wesley Publishing, 1970.